

Scanning

In Situ SEM Nanomanipulation and Nanomechanical/Electrical Characterization

Lead Guest Editor: Yang Lu

Guest Editors: Yajing Shen, Xinyu Liu, Mohd R. Bin Ahmad, and Yan Chen



***In Situ* SEM Nanomanipulation and
Nanomechanical/Electrical Characterization**

Scanning

***In Situ* SEM Nanomanipulation and
Nanomechanical/Electrical Characterization**

Lead Guest Editor: Yang Lu

Guest Editors: Yajing Shen, Xinyu Liu, Mohd R. Bin Ahmad,
and Yan Chen



Copyright © 2017 Hindawi. All rights reserved.

This is a special issue published in "Scanning." All articles are open access articles distributed under the Creative Commons Attribution License, which permits unrestricted use, distribution, and reproduction in any medium, provided the original work is properly cited.

Editorial Board

Masayuki Abe, Japan
David Alsteens, Belgium
Igor Altfeder, USA
Jose Alvarez, France
Richard Arinero, France
Renato Buzio, Italy
Brunero Cappella, Germany
Antonio Checco, USA
Ovidiu Cretu, Japan
Nicolas Delorme, France
Hendrix Demers, Canada
Carlo Dri, Italy

John R. Dutcher, Canada
Jonathan R. Felts, USA
Marina I. Giannotti, Spain
Sacha Gómez, Spain
Federico Grillo, UK
Anton V. Ievlev, USA
Berndt Koslowski, Germany
Jörg Kröger, Germany
Jessem Landoulsi, France
Emanuela Margapoti, Brazil
Alessio Morelli, UK
Daniele Passeri, Italy

Andrea Picone, Italy
Jason L. Pitters, Canada
Michela Relucenti, Italy
Damien Riedel, France
Francesco Ruffino, Italy
Steven R. Schofield, UK
Christian Teichert, Austria
Marilena Vivona, UK
Kislon Voitchovsky, UK
Masamichi Yoshimura, Japan

Contents

***In Situ* SEM Nanomanipulation and Nanomechanical/Electrical Characterization**

Yang Lu, Yajing Shen, Xinyu Liu, Mohd R. Bin Ahmad, and Yan Chen

Volume 2017, Article ID 8016571, 2 pages

Recent Advances on In Situ SEM Mechanical and Electrical Characterization of Low-Dimensional Nanomaterials

Chenchen Jiang, Haojian Lu, Hongti Zhang, Yajing Shen, and Yang Lu

Volume 2017, Article ID 1985149, 11 pages

Electron Beam Irradiation Induced Multiwalled Carbon Nanotubes Fusion inside SEM

Daming Shen, Donglei Chen, Zhan Yang, Huicong Liu, Tao Chen,

Lining Sun, and Toshio Fukuda

Volume 2017, Article ID 8563931, 8 pages

In Situ SEM Torsion Test of Metallic Glass Microwires Based on Micro Robotic Manipulation

Chenchen Jiang, Haojian Lu, Ke Cao, Wenfeng Wan, Yajing Shen, and Yang Lu

Volume 2017, Article ID 6215691, 7 pages

Automated Axis Alignment for a Nanomanipulator inside SEM and Its Error Optimization

Chao Zhou, Lu Deng, Long Cheng, Zhiqiang Cao, Shuo Wang, and Min Tan

Volume 2017, Article ID 3982503, 8 pages

Application of Environmental Scanning Electron Microscope-Nanomanipulation System on Spheroplast Yeast Cells Surface Observation

Maryam Alsadat Rad, Mohd Ridzuan Ahmad, Masahiro Nakajima, Seiji Kojima, Michio Homma, and Toshio Fukuda

Volume 2017, Article ID 8393578, 7 pages

Characterization of the Resistance and Force of a Carbon Nanotube/Metal Side Contact by Nanomanipulation

Ning Yu, Masahiro Nakajima, Qing Shi, Zhan Yang, Huaping Wang, Lining Sun, Qiang Huang, and Toshio Fukuda

Volume 2017, Article ID 5910734, 11 pages

Editorial

***In Situ* SEM Nanomanipulation and Nanomechanical/Electrical Characterization**

Yang Lu,¹ Yajing Shen,¹ Xinyu Liu,² Mohd R. Bin Ahmad,³ and Yan Chen⁴

¹*City University of Hong Kong, Kowloon, Hong Kong*

²*University of Toronto, Toronto, ON, Canada*

³*Universiti Teknologi Malaysia, Johor, Malaysia*

⁴*Arizona State University, Mesa, AZ, USA*

Correspondence should be addressed to Yang Lu; yanglu@cityu.edu.hk

Received 23 October 2017; Accepted 23 October 2017; Published 5 November 2017

Copyright © 2017 Yang Lu et al. This is an open access article distributed under the Creative Commons Attribution License, which permits unrestricted use, distribution, and reproduction in any medium, provided the original work is properly cited.

In the past decades, in situ scanning electron microscopy (SEM) has become a powerful technique for the experimental study of nanomaterials, since it can provide unprecedented details for individual nanostructures upon mechanical and electrical stimulus, uncovering the fundamental deformation and failure mechanisms for their device applications, such as nanoelectronics, solar cells, and sensors. This special issue aims at exhibiting the latest research achievements, findings, and ideas in the field of in situ SEM nanomanipulation, nanomechanical/electrical characterization, and nanoassembly. In order to give clear introduction and guideline to researchers new to this field, C. Jiang et al. firstly offered an overview about some recent progresses from the literature. They have classified the recent advances of in situ SEM mechanical characterization techniques into tensile, compression, indentation, and bending tests. The state-of-the-art electromechanical coupling analysis was also discussed. Finally, the history of micro/nanomanipulation techniques was also presented, including the critical challenges for the development and design of robust in situ SEM characterization.

Among the original researches reported in this special issue, N. Yu et al. characterized both the resistance and the force at a CNT/Au side-contact interface inside SEM by nanomanipulation technique before and after electron beam induced deposition (EBID). Their robotic system could be expanded to investigate the contact between CNTs and other metals and to fabricate nanodevices such as CNT-FETs in

combination with EBID. On the other hand, C. Jiang et al. investigated the torsion fracture behavior of $\text{La}_{50}\text{Al}_{30}\text{Ni}_{20}$ MG microwire under in situ SEM and compared the fracture surface with tensile loading test based on a self-developed micro robotic mechanical testing system. The fracture mechanism of the microwire under torsional loading was also proposed. They believed this micro robotic system could also be used in many other applications in the future, for example, microassembly of nanoelectronic devices and nanomanufacturing of hierarchical low-dimensional nanomaterials.

Another important application of in situ manipulation techniques is about nanoassembly with high degree of automation, which could speed up the fabrication of the nanodevices in the future. C. Zhou et al. proposed an automated axis alignment method for a nanomanipulator inside the SEM by recognizing the position of a closed-loop controlled end-effector. Over these years, carbon nanotube (CNT) was proved to have potential applications in the integration of large-scale interconnections, a key component in the manufacturing of nanodevices. A method of multiwalled carbon nanotubes (MWCNTs) fusion by electronic beam irradiation inside SEM was reported and proved reliable by D. Shen and coworkers.

So far there are less reports on the applications of in situ SEM techniques for biomedical research because of the challenges in high vacuum operating environment and complicated bio-sample preparation steps. Here, M. A. Rad et al. performed in situ local direct observation and

manipulation of a biological sample by controlling the environmental conditions, demonstrating the ability to observe spheroplast cells under electron microscope without the need of sample coating for the first time, which could open great opportunities for in situ SEM-aid biomedical research.

Overall, the objectives of the special issue have been reached in terms of advancing the current state of the art of in situ SEM nanomanipulation and nanomechanical/electrical characterization techniques. Several basic problems in these areas were well addressed and most of the proposed contributions exhibited very promising results that outperform existing studies in the community. Some results were even firstly reported in these areas, such as in situ torsion testing of microwires.

Acknowledgments

We would like to express our thanks to all the authors who submitted their original works to this special issue and to all the reviewers who helped us ensure the quality of the papers.

Yang Lu
Yajing Shen
Xinyu Liu
Mohd R. Bin Ahmad
Yan Chen

Review Article

Recent Advances on In Situ SEM Mechanical and Electrical Characterization of Low-Dimensional Nanomaterials

Chenchen Jiang,¹ Haojian Lu,¹ Hongti Zhang,^{1,2} Yajing Shen,^{1,3} and Yang Lu^{1,2}

¹Department of Mechanical and Biomedical Engineering, City University of Hong Kong, Kowloon, Hong Kong

²Centre for Advanced Structural Materials (CASM), Shenzhen Research Institute, City University of Hong Kong, Shenzhen 518057, China

³Centre for Robotics and Automation (CRA), Shenzhen Research Institute, City University of Hong Kong, Shenzhen 518057, China

Correspondence should be addressed to Yajing Shen; yajishen@cityu.edu.hk and Yang Lu; yanglu@cityu.edu.hk

Received 18 May 2017; Revised 29 August 2017; Accepted 1 October 2017; Published 25 October 2017

Academic Editor: Daniele Passeri

Copyright © 2017 Chenchen Jiang et al. This is an open access article distributed under the Creative Commons Attribution License, which permits unrestricted use, distribution, and reproduction in any medium, provided the original work is properly cited.

In the past decades, in situ scanning electron microscopy (SEM) has become a powerful technique for the experimental study of low-dimensional (1D/2D) nanomaterials, since it can provide unprecedented details for individual nanostructures upon mechanical and electrical stimulus and thus uncover the fundamental deformation and failure mechanisms for their device applications. In this overview, we summarized recent developments on in situ SEM-based mechanical and electrical characterization techniques including tensile, compression, bending, and electrical property probing on individual nanostructures, as well as the state-of-the-art electromechanical coupling analysis. In addition, the advantages and disadvantages of in situ SEM tests were also discussed with some possible solutions to address the challenges. Furthermore, critical challenges were also discussed for the development and design of robust in situ SEM characterization platform with higher resolution and wider range of samples. These experimental efforts have offered in-depth understanding on the mechanical and electrical properties of low-dimensional nanomaterial components and given guidelines for their further structural and functional applications.

1. Introduction

Due to their excellent mechanical and electrical properties, low-dimensional (1D/2D) nanomaterials, such as metallic/polymer/semiconductor nanowires, graphene, and MoS₂, have become important building blocks in applications like nanoelectronics, solar cells, and sensors, and so on [1–4]. Therefore, it is necessary to get a thorough understanding of their mechanical behaviors and electrical properties for the purposes of exploring their full potential functions and promoting the development of the advanced micro/nanoelectronics applications and mechatronic systems. However, due to their exceedingly small sample sizes at micro- and nanoscales, people can merely observe their general morphologies under optical microscopes [5] before, while they cannot directly manipulate and characterize them until the recent breakthroughs in scanning electron microscopy (SEM).

With the recent development of scanning electron microscopy and small scale micro/nanomanipulation and

mechanical/electrical testing techniques, interrogating the unique and wide-spectrum properties of individual nanostructures directly inside scanning electron microscopes (SEM) became possible. Various kinds of characterization methods for different types of nanomaterials, such as tensile tests, compression tests, and bending tests, have come forth. Particularly, as to the metallic or semiconductor nanomaterials, investigating their electrical properties is also meaningful. Traditionally, these tests can only be done outside SEM given to the limited chamber size of the testing instruments and controlling mechanisms. Although people can acquire data such as strength and Young's modulus of these nanomaterials and derive their failure mechanism by performing postmortem SEM study, they lose the opportunity to know how the samples behave upon mechanical/electrical stimulus which may contain abundant interesting phenomena. Therefore, people have spent years of efforts on developing small testing platforms which were suitable for in situ SEM mechanical or electrical characterizations. In recent

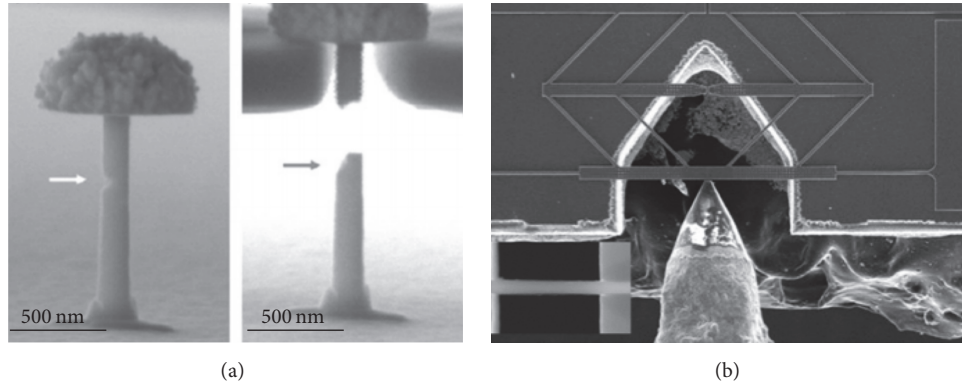


FIGURE 1: Typical tensile testing configurations on nanostructures. (a) shows that the sample can be stretched by a custom-milled diamond tension grip in SEM [17]. (b) Push-to-pull micromechanical device which can convert the compression force of the nanoindenter into tensile force [18].

years, with the help of commercialized nanoindentation system, atomic force microscope (AFM), micro/nanofabrication method, and micromechanical and microelectromechanical system (MEMS) devices, these testing methods can be gradually combined together for the desired “in situ characterization” inside SEM.

On the other hand, in order to give researchers more freedom and higher precision ability to manipulate the nanomaterials inside SEM during in situ experiments, advanced robotic systems have also been developed. Besides the function in nanomaterial sample manipulation and transferring, these systems also can exert force and electricity stimuli on samples directly during tests. Therefore, in this review paper, we mainly focus on the latest development on the in situ SEM techniques for individual nanomaterial testing including the recent micro/nanorobotics advances in this application field, as well as the related nanomaterial manipulation and transferring techniques with the corresponding challenges discussed.

2. In Situ SEM Mechanical Tests of Micro/Nanomaterials

2.1. Tensile Testing of 1D or 2D Nanostructures. Among all the mechanical testing techniques, tensile test is the most straightforward manner which can provide a wide-spectrum of mechanical properties, such as elasticity, plasticity, and fracture strength, in a direct way. Since in situ SEM tensile test has been developed by Dingley [6], large amount of efforts has been devoted to this field [7–9]. The size effects of nanomaterials have been demonstrated by in situ tensile mechanical test for many materials, such as Ag nanowire [10] and ZnO nanowire [11]. In most of the cases, the fracture strength increases as the diameter of the nanowires decreases. Recently, a new concept of “ultra-strength” has been proposed [12, 13] and further demonstrated in many nanomaterials. Tian et al. [14] approached the elastic strain limit of the submicron-sized metallic glass specimens and the corresponding strength of them was about twice as high as the already impressive elastic limit observed in bulk metallic

glass samples. Zhang et al. [15] have found that vapor-liquid-solid-grown single-crystalline Si nanowires with diameters of ~ 100 nm could be repeatedly stretched above 10% elastic strain at room temperature, approaching the theoretical elastic limit of silicon (17 to 20%). However, not every nanomaterial will display such “smaller is stronger” size effect; Zhang et al. [16] conducted in situ uniaxial quasi-static tensile tests on individual nanocrystalline Co nanowires and observed that Young’s modulus is (75.3 ± 14.6) GPa with a tensile strength of (1.6 ± 0.4) GPa, which are significantly lower than their bulk counterparts and the theoretical value of monocrystalline samples, therefore, deviated from the traditional theory.

Understanding the failure mechanism in micro/nanomaterials is demanding for the design of reliable structural materials and micro- and nanoscale devices. Gu et al. [17] investigated the fracture behavior of nanocrystalline Pt nanocylinders with prefabricated surface notches as shown in Figure 1(a) and demonstrated that most of these samples fractured at the notches. Fatigue fracture mechanism of nanomaterials also can be done with in situ tensile loading; Lu et al. [18, 19] have demonstrated the first quantitative low-cycle in situ SEM tensile fatigue testing of Ni nanowires based on the nanoindenter-assisted “push-to-pull MEMS” dynamic tensile straining system, as shown in Figure 1(b). Also based on MEMS device, Jiang et al. [20] developed a high cycle nanowire fatigue tensile and torsion platform which reduced the time to investigate the fatigue behavior of nanostructures.

In situ SEM tensile test can also fulfill the mechanical investigation of 2D nanostructures. Therefore, metal thin films, which are key components in microelectronics devices, have been studied extensively. Haque and Saif [24] presented a novel tensile testing technique utilizing MEMS force sensors for in situ mechanical characterization of submicron scale freestanding thin films in SEM decade ago. Sim and Vlassak [25] studied the mechanical properties of thin Au films at various temperature and strain rates during in situ SEM tensile tests. An inverse size effect where the yield strength at elevated temperature decreases with decreasing temperature was also observed. Zhang et al. [26] reported the first in situ tensile testing of suspended graphene using a

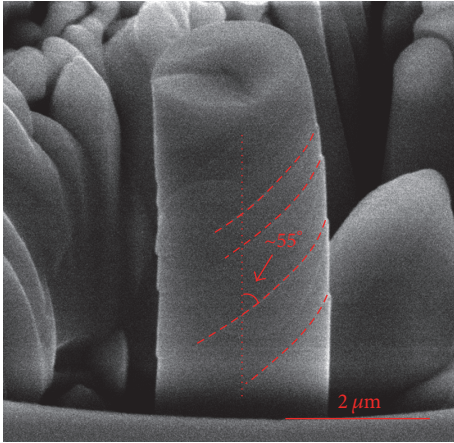


FIGURE 2: The typical postcompression test of niobium nanopillar which fractured with pronounced slip offsets [21].

nanomechanical device in a SEM and found that the cracked graphene samples exhibit a fast brittle fracture behavior with the breaking stress much lower than the intrinsic strength of graphene. Recently, we also investigated the 2D MoS₂ membranes under in situ SEM tensile loading and provided some critical insights into the mechanical properties and fracture behavior of them [27].

2.2. Compression Testing of Micro/Nanopillars. Compression tests on micro/nanomaterials are similar to that applied on the macroscopic samples, but with some modifications facilitating both the fabrication of the diminutive samples and the subsequent manipulation via the testing system. Commercial nanoindentation systems are always regarded as the mechanical test frame of compression experiments, except that the sharp indentation tip is accordingly replaced with a flat-punch tip. The load and displacement resolutions of most nanoindentation systems are well suited for micro/nanocompression testing because they typically produce stress-strain curves with nanoscale resolution for micro/nanoscale samples. Figure 2 shows the typical compression test of a nanopillar which was fabricated by FIB.

As many micro/nanomaterials behave significantly different in compression tests from the way they perform under tension [28], the compression testing of micromachined micro/nanopillars is currently an active research area since Gane and Bowden [29] firstly reported the in situ compression test inside SEM. The failure mechanism of materials under compression may be the most attracting point to the researchers because of the particular stress state in it, which is usually not entirely uniaxial. This approach has sparked a number of studies and the traditional laws of plasticity at small scales were challenged because the overall sample dimensions limited the length scales available for plastic processes [30–33]. Particularly, for amorphous MG (metallic glass) materials, which usually have high strength, low inhomogeneous plasticity of micro/nanopillars have been found under compression tests [34].

Similar to the in situ tensile test of micro/nanomaterials, size effects were also observed in compression tests in both bcc and fcc single-crystalline micro/nanopillars [35]. Kim and Greer [36] even conducted a contrastive in situ tensile and compression tests on fcc (Au) and bcc (Mo) nanopillars and found that the size dependence between the two loading directions in Au nanopillar was identical while there was a pronounced tension-compression asymmetry in Mo nanopillars.

Recently, compression tests at different circumstances or on special materials were also conducted. Wheeler and Michler [37] investigated the transitions in deformation mechanism of silicon nanopillars with increasing temperature under microcompression test. Raghavan et al. [38] studied the failure mechanism of Cu/TiN multilayered thin film micropillars at elevated temperature and found that the yielding of the multilayers was governed by the stress-assisted diffusion of the Cu interlayers, which coalesce into microcrystals and grow into larger faceted crystals at elevated temperatures of 200 and 400°C. Zhang et al. [21] systematically investigated the CoCrCuFeNi high-entropy alloy micro/nanopillars, which has equi- or near equiatomic compositions and found the less sensitive size effect of its yield strength. Traditionally, the semiconductor materials are usually brittle at room temperature; however, Michler et al. [39] found that the GaAs micropillars have very large plastic strain even comparable to that of metal single crystal micropillars.

2.3. Nanoindentation on Thin Films. Nanoindentation system is not only suitable for micro/nanopillars compression test, but also useful in the quantitative characterization of thin films [40] and microbeams with custom made tips. As some ceramic thin films are widely used as a protective coating in tribological applications [41], it became necessary to investigate the microhardness, Young's modulus, and fracture toughness of them. With the decreasing size of the actuators and sensors, the in situ SEM nanoindentation can give more information on the formation and propagation of mechanically induced dislocations and defects during the experiment so as to correlate the load-displacement data with the in situ microstructural changes. For example, the Rabe et al. [42] found that the sudden increases of the displacement at constant load on Si-DLC film were due to the chipping out of materials with the help of the SEM video. Rzepiejewska-Malyska et al. [43] studied the deformation mechanisms of TiN, CrN, and multilayer TiN/CrN thin films on silicon substrate. The TiN thin film showed short radial cracks, whereas CrN deformed through pileup and densification of the material. For TiN/CrN, multilayer pileup and cracks were found. Heiroth et al. [44] compared the deformation mechanism of amorphous yttria-stabilized zirconia films with crystalline Y₂O₃ films under nanoindentation and found that the amorphous films deform plastically by shear bands, while the crystalline films reveal a brittle behavior and accommodate the load by the formation of hoop and surface cracks.

As those thin films were directly deposited or grown on a substrate, the experiments yield mechanical properties of a composite structure not of the thin film itself, especially for

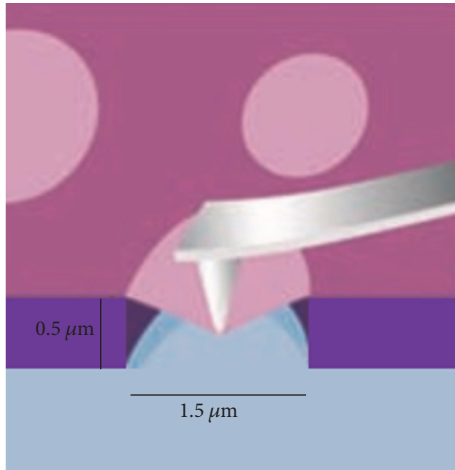


FIGURE 3: Schematic illustration of nanoindentation on freestanding graphene film [22].

increasingly thinner films. In order to get rid of the influence from the substrate, some researchers have conducted tests on freestanding thin films. However, the in situ SEM indentation of freestanding thin films was little reported. Lee et al. [22] measured the elastic properties and intrinsic strength of monolayer graphene with the help of AFM, as shown in Figure 3. Similar to Lee, Frank et al. [45] and Suk et al. [46] also conducted the mechanical testing on free standing thin film of graphene sheets and monolayer graphene oxide, respectively, by AFM. Leseman and Mackin [47] developed a new indentation system to investigate the freestanding Au thin films with a ball-like indentation tip. Although it was not performed inside SEM, it has the ability to record the applied load and membrane displacement simultaneously.

2.4. Micro/Nanoscale Bending Test. Another useful test geometry under the scope of indentation measurement is the micro/nanobending test, which can be categorized into single point bending test, three-point double-clamped bending test, and the four-point double-clamped bending test. Figure 4 shows the typical configurations of bending test. With the help of focused ion beam (FIB) technique it is relatively easy to machine micrometer-sized bending test samples. This attracted many researchers to study the material fracture mechanism under bending test.

In single point bending test, the freestanding beam or wire is always named as cantilever. Allison et al. [48] performed in situ SEM microcantilever beam experiments on bioinspired nanocomposites and the deformation mechanism was similar to nacre. Howard et al. [49] even studied the cyclic deformation of metal microbeam under in situ SEM bending test and found that dislocation pileup within these microbeams occurs exactly as it would in a macroscopic fatigue specimen. The in situ single point bending test can also be used in the bending of nanoscale materials; for example, Vlassov et al. [50] measured Young's modulus and yield point of the Ag nanowires and even observed their plastically deformation before fracture. With the aim of providing the

characterization of cracking process of metallic thin films, Hintsala et al. [51] reported the in situ doubly clamped three-point bending test of microscale and nanoscale specimens. The crack tip behavior was not kept out of view by the indenter as usual, allowing for further EBSD characterization.

What is more, with the help of newly self-developed bending test methods, some interesting phenomenon has been found by researchers. Elhebeary and Saif [52] investigated the cofabricated single crystal silicon (SCS) microbeam by a newly designed system, which eliminated any misalignment error. With the advantage of high temperature testing ability, the study revealed significant reduction in the Brittle to Ductile temperature (BDT) of SCS microbeams compared to their bulk counterparts.

3. In Situ SEM Electrical/Electromechanical Probing

3.1. In Situ Electrical Property Probing of Nanostructure. Electrical property is also an important factor that affects the reliability of metallic and semiconductor nanowires beside their mechanical properties when serving as interconnecting leads and functional building blocks in applications of nanodevices and nanoelectronics [53–56]. Although it is difficult to measure the various electrical properties of nanomaterials, with the newly developed techniques, such as nanomanipulators and nanoindentation system, a lot of interesting results have been obtained, as shown in Figure 5.

Firstly, as to the fundamental *I-V* behaviors of nanowire, Noyong et al. [57] developed a nanomanipulation system with four manipulators and demonstrated the setup by measuring the average resistance of the platinum wire. Similar to Michael Noyong, the Au [58], GaAs [59], and CoPt/Pt [60] multilayer nanowires' resistance also have been accurately measured. Furthermore, the linear relationship between resistance and sample length [58, 60] also have been obtained which indicated that the contact resistance between tips and nanowires was largely reproducible. Another interesting phenomenon related to the current density and Joule heating of nanowires was the electromigration, which was a major reliability issue in the metallic interconnects. Huang et al. [61] studied the in situ SEM electromigration of the Cu nanowires and the relationship between the failure lifetimes and applied current densities was measured.

3.2. Electromechanical Coupling Analysis of Nanostructure. Electromechanical coupling effect is also a topic worth investigating in the nanomaterials. Understanding the electromechanical properties of nanomaterials is essential for further implementation of the fascinating applications in metallic and semiconducting systems. For example, increased attention has been paid to semiconducting nanowires, whose piezoresistivity [62] or piezoelectricity [63] property can be used as sensors, energy harvesting, and transistors. In electromechanical studies of nanowires, the most common approach was deforming the sample and measuring the specimen's electrical response (resistivity, generated charge, etc.) by using two or four electrical contacts same as Figure 5 shows, except that the tips of the manipulators should be

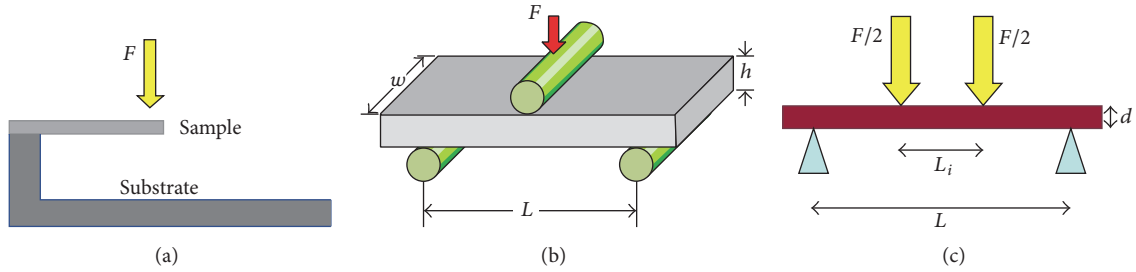


FIGURE 4: The schematic illustration of different bending tests of thin films. (a) Single point bending test. (b) Three-point double-clamped bending test and (c) four-point double-clamped bending test.

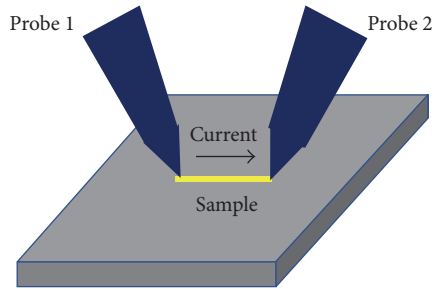


FIGURE 5: Schematic illustration of in situ electrical probing of an individual nanowire inside SEM.

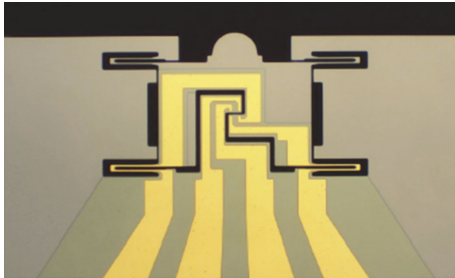


FIGURE 6: Optical image of an electrical push-to-pull micromechanical device for electromechanical coupling analysis of individual nanowires.

bonded with the nanowires and the movement of the tips will exert tensile force and current simultaneously on the nanowire.

However, this kind of method often involves contact resistance and may introduce Schottky barriers. In order to avoid these problems, devices dedicated for electromechanical characterization have been developed. For example, by using a commercially available E-PTP (electrical push-to-pull) device with four electrodes, as Figure 6 shows, Bhowmick et al. [64] studied the ZnO nanowire under tensile stress and found that, at constant applied voltage, the current will increase with the increasing of the load force. Based on the self-designed MEMS device, Bernal et al. [65] investigated the relationship between resistance and strain of Ag and Si nanowires which have shown opposite behaviors which could be very interesting to further investigate such electromechanical coupled effect. Although the commercial

devices were beneficial for speeding up the process of the measurement, self-developed devices could satisfy the different requirements of materials and structures.

4. The Pros and Cons Analysis of In Situ SEM Testing

Based on these above fascinating researches, the advantages of in situ SEM were very obvious. The most important one was that the comparison of the fracture process videos and the real-time data curves, such as stress-strain and $I-V$ curves, could provide much useful information to understand the fracture mechanism of micro/nanoscale materials. It also ensured that no accidents happen, for example, debonding of the sample. Therefore, the precise and convincing results data could be guaranteed. These relatively precise results benefited with not only the advance testing platforms, but also the nanoscale resolution of the SEM images, which can provide precise measurement of the sample dimensions. Some software types, such as DIC (digital image correlation), also have lots of functions for image analysis and processing, deformation, shape, and motion measurement, which could help the researchers obtain more convincing data [66, 67].

However, the in situ SEM technique was not faultless, such as the complexity of the process and the high price of the instruments. According to our own experience, the time consumed for in situ SEM experiments was much longer than that of in situ optical ones, such as the installation of instruments in SEM, the connection between the controller outside SEM and the device through a port, and the vacuum-pumping process. Particularly, as to the sample preparation process, there are two methods to bond the materials. The first one is the FIB (focus ion beam) coating technique, which could ensure a strong and precise bonding of samples inside SEM, for example, the tensile test of Co nanowire [16]. But the manipulation of FIB is difficult to operate and the cost is high. Usually some researchers prefer to bond the materials with glue by a micromanipulator under optical microscope [18]. Although the cost is low, we need much time to practice to achieve the precise and quick bonding.

Nevertheless, for small scale samples, many tests have to be done in order to have a statistically convincing result. Few researchers paid much attention to the high-throughput problems, which were more like technique issues than scientific ones. With this aim, we have tried to speed up the

process of studying the fatigue behavior of nanowires under torsion loading based on a DMD (digital micromirror device) chip, which have millions of movable micromirrors and could test many samples at one experiment [20]. As to the in situ SEM compression tests, lots of micropillars could be made on single chip at the same time, which could speed up the systematic study of the materials; for example, Moser et al. made an array of microsilicon pillars with different size [68].

5. Robotic In Situ SEM Micro/Nanomanipulation

As we have reviewed various in situ SEM mechanical/electrical testing progress of micro/nanomaterials above, it is worth reviewing this field from another aspect, which is about the technological manipulation components or the robotic-aid manipulation/testing instrument used in these experiments. Without the help of advanced micro/nanomanipulation instrument, it is hard to accomplish the in situ SEM characterization of nanomaterials. Owing to the precise techniques for positioning, sensing, and nanometer resolution manipulation, more and more nanorobotic manipulation systems have been installed in SEM to explore material characteristics with small scale [8, 10, 13, 18, 25, 32]. Meanwhile, a large number of researchers have engaged in developing in situ SEM nanorobotic manipulation systems for material field for several decades [45, 47, 50], since the manipulators are useful for picking, placing, bonding nanosized components, and even exerting tensile, bending, and kinking force on them. These systems can be categorized into two different types, traditional robotic manipulation systems and advanced in situ nanorobotic manipulation systems.

5.1. Traditional Robotic Manipulation Systems. Traditionally, the manipulation systems within in situ SEM characterization are mainly about nanoindentation system. Gane et al. have been engaged in in situ SEM material test since 1966; they developed a nanorobotic indentation system to realize in situ indentation test. In this system, the stylus is installed on a nanorobotic manipulator, which can be moved through a moving-coil device with a permanent magnet [15]. Bangert and Wagendristel have developed another kind of ultralow-load hardness tester, which is composed of elastic cantilever, electromagnet, indenter, and a double leaf spring [69]. Hedenqvist and Hogmark developed a kind of 2DOF nanorobotic manipulation system with a friction force detector and realized in situ SEM indentation test in 1997 [70]. In situ SEM tensile test helped by manipulation system first accomplished in 1999; Yu et al. developed a nanorobotic manipulation system with four degrees of freedom (DOF), which has the ability to manipulate small scale objects with one rotational DOF and three linear DOF [71]. Rzepiejewska-Malyska et al. developed a kind of nanorobotic manipulation system with three slip-stick actuators installed perpendicular to each other, which can realize in situ SEM mechanical observations during nanoindentation with high magnification [72]. Romeis et al. developed a novel nanorobotic manipulation system with two main assembly groups: an upper part which was utilized for moving the employed

probe and a lower part which was composed of a force sensor and a sample support [73]. These pioneers have paved the way for fundamental material research and practical characterization.

With the popularity of the position techniques, a number of commercial in situ SEM material characteristic test systems have been developed by companies, such as Hysitron, Alemnis, Nanomechanics, ASMEC, Kammrath & Weiss, Deben, and MTI Instruments as Figure 7 shows. With the help of these mentioned commercial in situ SEM material characteristic test systems, scientists have made a great process in material research field [15, 18, 73–75].

5.2. Advanced In Situ Nanorobotic Manipulation System. Compared with traditional material test nanorobotic manipulation system, scholars have developed nanorobotic manipulation platforms with multiple DOF and piezoelectric actuators to realize manipulating micro/nanoscale objects, not only for material test [76–79] but also for nanoelectromechanical systems assembly [80–82], biological cell characterization, and manipulation [83–86].

Among all kinds of advanced nanorobotic manipulation systems, actuation is one of the main challenges for scholars to control the nanorobotic manipulator precisely due to high vacuum environment inside SEM. Compared with thermal actuators, electric motors, and voice coil actuators, piezoelectric actuators are widely utilized in recent advanced nanorobotic manipulation systems because this kind of actuator does not need dissipate heat effectively and will not interfere with electron optics [87, 88]. Meanwhile, the piezoelectric actuators can generate large forces with a high bandwidth [89]. Normally, the advanced nanorobotic manipulation systems are composed of several piezoelectric actuators to realize multiple direction manipulation, as shown in Figure 8, which have both coarse positioning function and fine positioning function for working effectively [23].

Thanks to the increasingly larger chamber of model SEMs, scientists now can even combine scanning electron microscopy and atomic force microscopy (AFM) facility or nanomanipulation instruments into a single system, among which AFM/SEM hybrid systems are widely used [90]. When an AFM is integrated inside an SEM, it can realize topography analysis with high resolution and force feedback due to the real-time manipulation and imaging [91, 92]. With the help of this kind of hybrid system, manipulation and characterization of nanomaterials can be realized [10, 93–95], as well as assembly of nanodevices [96, 97] and cell characterization and manipulation [98, 99]. Owing to the advanced nanorobotic manipulation systems' development towards the direction of programmability, automation, and specificity, they will continue paving the way for micro/nanomaterial characterizations.

6. Summary and Outlook

This paper mainly reviewed the recent experimental efforts on in situ SEM mechanical and electrical characterization of the nanomaterials as well as the technical advances of

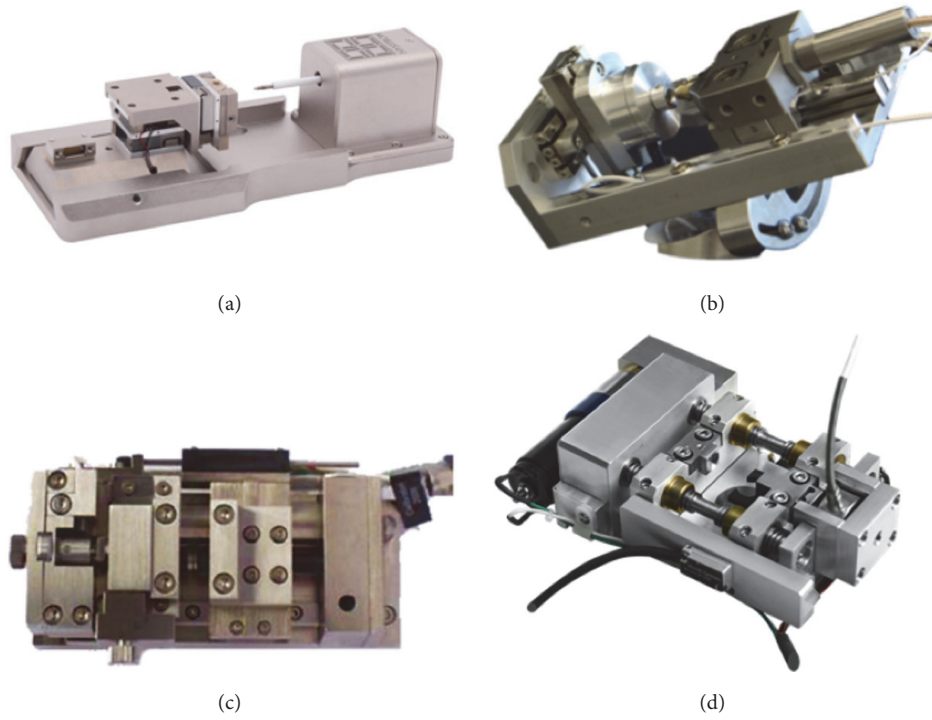


FIGURE 7: Some commercialized in situ testing systems: (a) Hysitron PI95, (b) Alemnis nanoindenter, (c) Deben Microtest, and (d) MTI Instruments tensile stage.

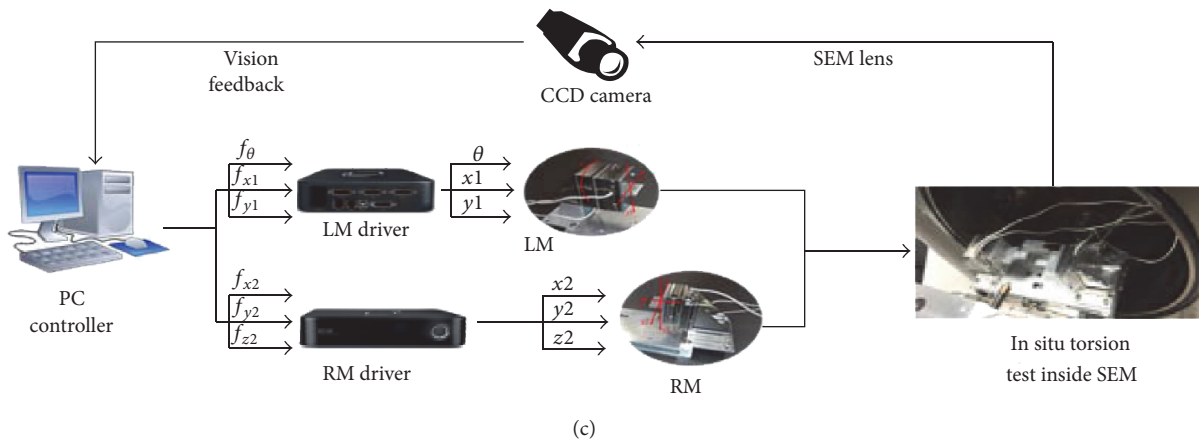
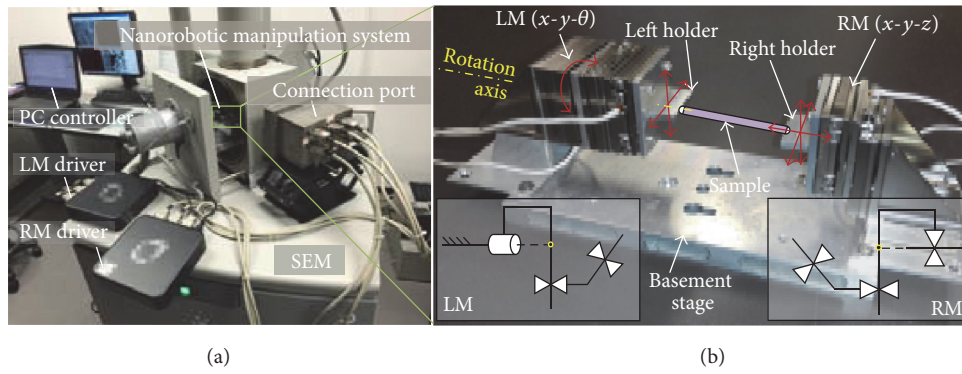


FIGURE 8: Advanced in situ SEM nanorobotics testing system developed by Shen et al. [23].

different testing and manipulation platforms. These experiments not only manifested the unique properties of the nanomaterials but also supplied useful images or videos to help researchers in analyzing the mechanism involved, which may give beneficial guidance on their applications. Despite the significant progress, challenges still remained in the in situ SEM characterization field, such as reducing the time consumed and complexity of the experiments to produce more convincing statistical data, transferring the 2D thin films onto the testing platform effectively even with high automation, developing platforms suitable for high cycle fatigue testing, and integrating different external factors like force, electricity, and even heating into the testing platforms to study the sample's responses simultaneously. We believe further advances in both hardware and software developments will produce even smaller, delicate, more precise, and versatile testing techniques for in situ SEM characterization and make well preparation for the device applications of low-dimensional micro/nanomaterials in our daily life.

Conflicts of Interest

The authors declare that they have no conflicts of interest.

Authors' Contributions

Chenchen Jiang and Haojian Lu contributed equally to this work.

Acknowledgments

The authors gratefully acknowledge the funding support by Research Grants Council of the Hong Kong Special Administrative Region (CityU 138813, 11216515, and 11278716), the National Natural Science Foundation of China (51301147, 61403323), and Shenzhen Basic Research Project (JCYJ20160329150236426).

References

- [1] G. Chai, E. Rusu, and L. Chow, "Microsensor on single ZnO microwire," in *Proceedings of the 2009 International Semiconductor Conference, CAS 2009*, pp. 275–278, October 2009.
- [2] J. Lee and J. Kim, "Fabrication of strongly anchored, high aspect ratio elastomeric microwires for mechanical and optical applications," *Journal of Micromechanics and Microengineering*, vol. 21, no. 8, Article ID 085016, 2011.
- [3] M. C. Putnam, S. W. Boettcher, M. D. Kelzenberg et al., "Si microwire-array solar cells," *Energy & Environmental Science*, vol. 3, no. 8, pp. 1037–1041, 2010.
- [4] Q. Yang, W. Wang, S. Xu, and Z. L. Wang, "Enhancing light emission of ZnO microwire-based diodes by piezo-phototronic effect," *Nano Letters*, vol. 11, no. 9, pp. 4012–4017, 2011.
- [5] M. K. Habibi and Y. Lu, "Crack propagation in bamboo's hierarchical cellular structure," *Scientific Reports*, vol. 4, article no. 5598, 2014.
- [6] D. J. Dingley, "A simple straining stage for the scanning electron microscope," *Micron* (1969), vol. 1, no. 2, pp. 206–210, 1969.
- [7] Y. Lu and J. Lou, "Quantitative in-situ nanomechanical characterization of metallic nanowires," *JOM: The Journal of The Minerals, Metals & Materials Society (TMS)*, vol. 63, no. 9, pp. 35–42, 2011.
- [8] X. Liu, Y. Liu, B. Jin, Y. Lu, and J. Lu, "Microstructure evolution and mechanical properties of a smated mg alloy under in situ sem tensile testing," *Journal of Materials Science and Technology*, vol. 33, no. 3, pp. 224–230, 2017.
- [9] D. S. Gianola, A. Sedlmayr, R. Mnig et al., "In situ nanomechanical testing in focused ion beam and scanning electron microscopes," *Review of Scientific Instruments*, vol. 82, no. 6, Article ID 063901, 2011.
- [10] Y. Zhu, Q. Qin, F. Xu et al., "Size effects on elasticity, yielding, and fracture of silver nanowires: In situ experiments," *Physical Review B: Condensed Matter and Materials Physics*, vol. 85, no. 4, Article ID 045443, 2012.
- [11] F. Xu, Q. Qin, A. Mishra, Y. Gu, and Y. Zhu, "Mechanical properties of ZnO nanowires under different loading modes," *Nano Research*, pp. 1–10, 2010.
- [12] T. Zhu, J. Li, S. Ogata, and S. Yip, "Mechanics of ultra-strength materials," *MRS Bulletin*, vol. 34, no. 3, pp. 167–172, 2009.
- [13] T. Zhu and J. Li, "Ultra-strength materials," *Progress in Materials Science*, vol. 55, no. 7, pp. 710–757, 2010.
- [14] L. Tian, Y.-Q. Cheng, Z.-W. Shan et al., "Approaching the ideal elastic limit of metallic glasses," *Nature Communications*, vol. 3, article no. 609, 2012.
- [15] H. T. Zhang, J. Tersoff, S. Xu et al., "Approaching the ideal elastic strain limit in silicon nanowires," *Science Advances*, vol. 2, no. 8, Article ID e1501382, 2016.
- [16] D. Zhang, J.-M. Breguet, R. Clavel, L. Phillippe, I. Utke, and J. Michler, "In situ tensile testing of individual Co nanowires inside a scanning electron microscope," *Nanotechnology*, vol. 20, no. 36, Article ID 365706, 2009.
- [17] X. W. Gu, Z. Wu, Y.-W. Zhang, D. J. Srolovitz, and J. R. Greer, "Microstructure versus flaw: mechanisms of failure and strength in nanostructures," *Nano Letters*, vol. 13, no. 11, pp. 5703–5709, 2013.
- [18] H. Zhang, C. Jiang, and Y. Lu, "Low-cycle fatigue testing of Ni nanowires based on a micro-mechanical device," *Experimental Mechanics*, vol. 57, no. 3, pp. 495–500, 2017.
- [19] Y. Lu, Y. Ganesan, and J. Lou, "A Multi-step method for In situ mechanical characterization of 1-D nanostructures using a novel micromechanical device," *Experimental Mechanics*, vol. 50, no. 1, pp. 47–54, 2010.
- [20] C. Jiang, D. Hu, and Y. Lu, "Digital micromirror device (DMD)-based high-cycle torsional fatigue testing micromachine for 1D nanomaterials," *Micromachines*, vol. 7, no. 3, article 49, 2016.
- [21] H. Zhang, K. W. Siu, W. Liao, Q. Wang, Y. Yang, and Y. Lu, "In situ mechanical characterization of CoCrCuFeNi high-entropy alloy micro/nano-pillars for their size-dependent mechanical behavior," *Materials Research Express*, vol. 3, no. 9, Article ID 094002, 2016.
- [22] C. Lee, X. Wei, J. W. Kysar, and J. Hone, "Measurement of the elastic properties and intrinsic strength of monolayer graphene," *Science*, vol. 321, no. 5887, pp. 385–388, 2008.
- [23] Y. Shen, W. Wan, L. Zhang, L. Yong, H. Lu, and W. Ding, "Multidirectional image sensing for microscopy based on a rotatable robot," *Sensors*, vol. 15, no. 12, pp. 31566–31580, 2015.
- [24] M. A. Haque and M. T. A. Saif, "Application of MEMS force sensors for in situ mechanical characterization of nano-scale thin films in SEM and TEM," *Sensors and Actuators A: Physical*, vol. 97–98, pp. 239–245, 2002.

- [25] G.-D. Sim and J. J. Vlassak, "High-temperature tensile behavior of freestanding Au thin films," *Scripta Materialia*, vol. 75, pp. 34–37, 2014.
- [26] P. Zhang, L. Ma, F. Fan et al., "Fracture toughness of graphene," *Nature Communications*, vol. 5, p. 5, 2014.
- [27] P. Li, C. Jiang, S. Xu et al., "In situ nanomechanical characterization of multi-layer MoS₂," *Nanoscale*, vol. 9, no. 26, pp. 9119–9128, 2017.
- [28] N. E. Dowling, *Mechanical Behavior of Materials*, Pearson, 2012.
- [29] N. Gane and F. P. Bowden, "Microdeformation of solids," *Journal of Applied Physics*, vol. 39, no. 3, pp. 1432–1435, 1968.
- [30] M. D. Uchic, D. M. Dimiduk, J. N. Florando, and W. D. Nix, "Sample dimensions influence strength and crystal plasticity," *Science*, vol. 305, no. 5686, pp. 986–989, 2004.
- [31] J. R. Greer, C. R. Weinberger, and W. Cai, "Comparing the strength of f.c.c. and b.c.c. sub-micrometer pillars: Compression experiments and dislocation dynamics simulations," *Materials Science and Engineering: A Structural Materials: Properties, Microstructure and Processing*, vol. 493, no. 1-2, pp. 21–25, 2008.
- [32] Z. W. Shan, R. K. Mishra, S. A. S. Asif, O. L. Warren, and A. M. Minor, "Mechanical annealing and source-limited deformation in submicrometre-diameter Nanocrystals," *Nature Materials*, vol. 7, no. 2, pp. 115–119, 2008.
- [33] J. R. Greer, J.-Y. Kim, and M. J. Burek, "The in-situ mechanical testing of nanoscale single-crystalline nanopillars," *JOM: The Journal of The Minerals, Metals & Materials Society (TMS)*, vol. 61, no. 12, pp. 19–25, 2009.
- [34] A. Dubach, R. Raghavan, J. F. Löffler, J. Michler, and U. Ramamurty, "Micropillar compression studies on a bulk metallic glass in different structural states," *Scripta Materialia*, vol. 60, no. 7, pp. 567–570, 2009.
- [35] M. D. Uchic, P. A. Shade, and D. M. Dimiduk, "Micro-compression testing of fcc metals: a selected overview of experiments and simulations," *JOM: The Journal of The Minerals, Metals & Materials Society (TMS)*, vol. 61, no. 3, pp. 36–41, 2009.
- [36] J.-Y. Kim and J. R. Greer, "Tensile and compressive behavior of gold and molybdenum single crystals at the nano-scale," *Acta Materialia*, vol. 57, no. 17, pp. 5245–5253, 2009.
- [37] J. M. Wheeler and J. Michler, "Elevated temperature, nanomechanical testing in situ in the scanning electron microscope," *Review of Scientific Instruments*, vol. 84, no. 4, Article ID 045103, 2013.
- [38] R. Raghavan, J. M. Wheeler, D. Esqué-de los Ojos et al., "Mechanical behavior of Cu/TiN multilayers at ambient and elevated temperatures: Stress-assisted diffusion of Cu," *Materials Science and Engineering: A Structural Materials: Properties, Microstructure and Processing*, vol. 620, pp. 375–382, 2014.
- [39] J. Michler, K. Wasmer, S. Meier, F. Östlund, and K. Leifer, "Plastic deformation of gallium arsenide micropillars under uniaxial compression at room temperature," *Applied Physics Letters*, vol. 90, no. 4, Article ID 043123, 2007.
- [40] W. C. Oliver and G. M. Pharr, "Nanoindentation in materials research: past, present, and future," *MRS Bulletin*, vol. 35, no. 11, pp. 897–907, 2010.
- [41] L. D. Marks, O. L. Warren, A. M. Minor, and A. R. Merkle, "Tribology in full view," *MRS Bulletin*, vol. 33, no. 12, pp. 1168–1173, 2008.
- [42] R. Rabe, J. M. Breguet, P. Schwaller et al., "Observation of fracture and plastic deformation during indentation and scratching inside the scanning electron microscope," *Thin Solid Films*, vol. 469–470, pp. 206–213, 2004.
- [43] K. Rzepiejewska-Malyska, M. Parlinska-Wojtan, K. Wasmer, K. Hejduk, and J. Michler, "In-situ SEM indentation studies of the deformation mechanisms in TiN, CrN and TiN/CrN," *Micron*, vol. 40, no. 1, pp. 22–27, 2009.
- [44] S. Heiroth, R. Ghisleni, T. Lippert, J. Michler, and A. Wokaun, "Optical and mechanical properties of amorphous and crystalline yttria-stabilized zirconia thin films prepared by pulsed laser deposition," *Acta Materialia*, vol. 59, no. 6, pp. 2330–2340, 2011.
- [45] I. Frank et al., "Mechanical properties of suspended graphene sheets," *Journal of Vacuum Science & Technology B: Microelectronics and Nanometer Structures Processing, Measurement, and Phenomena*, vol. 25, no. 6, pp. 2558–2561, 2007.
- [46] J. W. Suk, R. D. Piner, J. An, and R. S. Ruoff, "Mechanical properties of monolayer graphene oxide," *ACS Nano*, vol. 4, no. 11, pp. 6557–6564, 2010.
- [47] Z. C. Leseman and T. J. Mackin, "Indentation testing of axisymmetric freestanding nanofilms using a MEMS load cell," *Sensors and Actuators A: Physical*, vol. 134, no. 1, pp. 264–270, 2007.
- [48] P. Allison, R. Moser, J. Schirer, R. Martens, J. Jordon, and M. Chandler, "In-situ nanomechanical studies of deformation and damage mechanisms in nanocomposites monitored using scanning electron microscopy," *Materials Letters*, vol. 131, pp. 313–316, 2014.
- [49] C. Howard, R. Fritz, M. Alfreider, D. Kiener, and P. Hosemann, "The influence of microstructure on the cyclic deformation and damage of copper and an oxide dispersion strengthened steel studied via in-situ micro-beam bending," *Materials Science and Engineering: A Structural Materials: Properties, Microstructure and Processing*, vol. 687, pp. 313–322, 2017.
- [50] S. Vlassov, B. Polyakov, L. M. Dorogin et al., "Elasticity and yield strength of pentagonal silver nanowires: In situ bending tests," *Materials Chemistry and Physics*, vol. 143, no. 3, pp. 1026–1031, 2014.
- [51] E. Hintsala, D. Kiener, J. Jackson, and W. W. Gerberich, "In-Situ Measurements of Free-Standing, Ultra-Thin Film Cracking in Bending," *Experimental Mechanics*, vol. 55, no. 9, pp. 1681–1690, 2015.
- [52] M. Elhebeary and M. T. A. Saif, "Thermo-mechanical characterization of materials at micro/nanoscale under bending," in *Proceedings of the 30th IEEE International Conference on Micro Electro Mechanical Systems, MEMS 2017*, pp. 736–739, January 2017.
- [53] Y. Wu, J. Xiang, C. Yang, W. Lu, and C. M. Lieber, "Single-crystal metallic nanowires and metal/semiconductor nanowire heterostructures," *Nature*, vol. 430, no. 6995, pp. 61–65, 2004.
- [54] J. Zhou, Y. Gu, P. Fei et al., "Flexible piezotronic strain sensor," *Nano Letters*, vol. 8, no. 9, pp. 3035–3040, 2008.
- [55] J.-P. Raskin, J.-P. Colinge, I. Ferain et al., "Mobility improvement in nanowire junctionless transistors by uniaxial strain," *Applied Physics Letters*, vol. 97, no. 4, Article ID 042114, 2010.
- [56] H. Yan, H. S. Choe, S. Nam et al., "Programmable nanowire circuits for nanoprocessors," *Nature*, vol. 470, no. 7333, pp. 240–244, 2011.
- [57] M. Noyong, K. Blech, A. Rosenberger, V. Klocke, and U. Simon, "In situ nanomanipulation system for electrical measurements in SEM," *Measurement Science and Technology*, vol. 18, no. 12, pp. N84–N89, 2007.
- [58] Y. Peng, T. Cullis, and B. Inkson, "Accurate electrical testing of individual gold nanowires by in situ scanning electron microscope nanomanipulators," *Applied Physics Letters*, vol. 93, no. 18, Article ID 183112, 2008.

- [59] V. T. Fauske, D. C. Kim, A. M. Munshi et al., "In-situ electrical and structural characterization of individual GaAs nanowires," *Journal of Physics: Conference Series*, vol. 522, no. 1, Article ID 012080, 2014.
- [60] Y. Peng, T. Cullis, I. Luxmoore, and B. Inkson, "Electrical properties of individual CoPt/Pt multilayer nanowires characterized by in situ SEM nanomanipulators," *Nanotechnology*, vol. 22, no. 24, Article ID 245709, 2011.
- [61] Q. Huang, C. M. Lilley, and R. Divan, "An in situ investigation of electromigration in Cu nanowires," *Nanotechnology*, vol. 20, no. 7, Article ID 075706, 2009.
- [62] R. He and P. Yang, "Giant piezoresistance effect in silicon nanowires," *Nature Nanotechnology*, vol. 1, no. 1, pp. 42–46, 2006.
- [63] Z. L. Wang and J. Song, "Piezoelectric nanogenerators based on zinc oxide nanowire arrays," *Science*, vol. 312, no. 5771, pp. 243–246, 2006.
- [64] S. Bhowmick, D. Stauffer, H. Guo et al., "In situ electromechanical study of ZnO nanowires," *Microscopy and Microanalysis*, vol. 19, no. S2, pp. 434–435, 2013.
- [65] R. A. Bernal, T. Filleter, J. G. Connell et al., "In situ electron microscopy four-point electromechanical characterization of freestanding metallic and semiconducting nanowires," *Small*, vol. 10, no. 4, pp. 725–733, 2014.
- [66] S.-H. Joo, H. Kato, M. J. Jang et al., "Tensile deformation behavior and deformation twinning of an equimolar CoCrFeMnNi high-entropy alloy," *Materials Science and Engineering: A Structural Materials: Properties, Microstructure and Processing*, vol. 689, pp. 122–133, 2017.
- [67] N. Kang, Y. Kim, H. Jeon et al., "Wall-thickness-dependent strength of nanotubular ZnO," *Scientific Reports*, vol. 7, no. 1, 2017.
- [68] B. Moser, K. Wasmer, L. Barbieri, and J. Michler, "Strength and fracture of Si micropillars: A new scanning electron microscopy-based micro-compression test," *Journal of Materials Research*, vol. 22, no. 4, pp. 1004–1011, 2007.
- [69] H. Bangert and A. Wagendristel, "Ultralow-load hardness tester for use in a scanning electron microscope," *Review of Scientific Instruments*, vol. 56, no. 8, pp. 1568–1572, 1985.
- [70] P. Hedenqvist and S. Hogmark, "Experiences from scratch testing of tribological PVD coatings," *Tribology International*, vol. 30, no. 7, pp. 507–516, 1997.
- [71] M. Yu, M. J. Dyer, G. D. Skidmore et al., "Three-dimensional manipulation of carbon nanotubes under a scanning electron microscope," *Nanotechnology*, vol. 10, no. 3, pp. 244–252, 1999.
- [72] K. A. Rzepiejewska-Malyska, G. Buerki, J. Michler et al., "In situ mechanical observations during nanoindentation inside a high-resolution scanning electron microscope," *Journal of Materials Research*, vol. 23, no. 7, pp. 1973–1979, 2008.
- [73] S. Romeis, J. Paul, M. Ziener, and W. Peukert, "A novel apparatus for in situ compression of submicron structures and particles in a high resolution SEM," *Review of Scientific Instruments*, vol. 83, no. 9, Article ID 095105, 2012.
- [74] D. Kiener, W. Grosinger, G. Dehm, and R. Pippan, "A further step towards an understanding of size-dependent crystal plasticity: in situ tension experiments of miniaturized single-crystal copper samples," *Acta Materialia*, vol. 56, no. 3, pp. 580–592, 2008.
- [75] W. Zhang and Y. Liu, "Investigation of incremental fatigue crack growth mechanisms using in situ SEM testing," *International Journal of Fatigue*, vol. 42, pp. 14–23, 2012.
- [76] Z. Gong, B. K. Chen, J. Liu, and Y. Sun, "Robotic probing of nanostructures inside scanning electron microscopy," *IEEE Transactions on Robotics*, vol. 30, no. 3, pp. 758–765, 2014.
- [77] S. L. Toh, P. K. Tan, Y. W. Goh et al., "In-depth electrical analysis to reveal the failure mechanisms with nanoprobng," *IEEE Transactions on Device and Materials Reliability*, vol. 8, no. 2, pp. 387–393, 2008.
- [78] S. Zimmermann, S. A. Garnica Barragan, and S. Fatikow, "Nanorobotic processing of graphene: A platform tailored for rapid prototyping of graphene-based devices," *IEEE Nanotechnology Magazine*, vol. 8, no. 3, pp. 14–19, 2014.
- [79] C. Ru, Y. Zhang, Y. Sun et al., "Automated four-point probe measurement of nanowires inside a scanning electron microscope," *IEEE Transactions on Nanotechnology*, vol. 10, no. 4, pp. 674–681, 2011.
- [80] L. Dong, B. J. Nelson, T. Fukuda, and F. Arai, "Towards nanotube linear servomotors," *IEEE Transactions on Automation Science and Engineering*, vol. 3, no. 3, pp. 228–235, 2006.
- [81] Y. L. Zhang, J. Li, S. To et al., "Automated nanomanipulation for nanodevice construction," *Nanotechnology*, vol. 23, no. 6, Article ID 065304, 2012.
- [82] D. Xu, A. Subramanian, L. Dong, and B. J. Nelson, "Shaping nanoelectrodes for high-precision dielectrophoretic assembly of carbon nanotubes," *IEEE Transactions on Nanotechnology*, vol. 8, no. 4, pp. 449–456, 2009.
- [83] Y. Shen and T. Fukuda, "State of the art: micro-nanorobotic manipulation in single cell analysis," *Rendiconti Lincei*, vol. 1, no. 1, 2014.
- [84] W. Shang, D. Li, H. Lu, T. Fukuda, and Y. Shen, "Less-invasive non-embedded cell cutting by nanomanipulation and vibrating nanoknife," *Applied Physics Letters*, vol. 110, no. 4, Article ID 043701, 2017.
- [85] W. Shang, H. Lu, W. Wan, T. Fukuda, and Y. Shen, "Vision-based nano robotic system for high-throughput non-embedded cell cutting," *Scientific Reports*, vol. 6, Article ID 22534, 2016.
- [86] M. R. Ahmad, M. Nakajima, M. Kojima, S. Kojima, M. Homma, and T. Fukuda, "Instantaneous and quantitative single cells viability determination using dual nanoprobe inside ESEM," *IEEE Transactions on Nanotechnology*, vol. 11, no. 2, pp. 298–306, 2012.
- [87] Y. K. Yong, S. O. R. Moheimani, B. J. Kenton, and K. K. Leang, "Invited review article: high-speed flexure-guided nanopositioning: mechanical design and control issues," *Review of Scientific Instruments*, vol. 83, no. 12, Article ID 121101, 2012.
- [88] A. I. Denisyuk, A. V. Krasavin, F. E. Komissarenko, and I. S. Mukhin, "Mechanical, electrostatic, and electromagnetic manipulation of microobjects and nanoobjects in electron microscopes," *Advances in Imaging and Electron Physics*, vol. 186, pp. 101–140, 2014.
- [89] D. Jasper et al., "Robot-based automation on the nanoscale," in *Encyclopedia of Nanotechnology*, pp. 2246–2264, Springer, 2012.
- [90] C. Shi, "Recent advances in nanorobotic manipulation inside scanning electron microscopes," *Microsystems Nanoengineering*, p. 2, 2016.
- [91] P. Russell, D. Batchelor, and J. Thornton, "SEM and AFM: complementary techniques for high resolution surface investigations," in *Veeco Metrology Group*, 2001, http://www.veeco.com/pdfs/appnotes/an46_semandafm_20.pdf.
- [92] W. Häßler-Grohne, D. Hüser, K.-P. Johnsen, C. G. Frase, and H. Bosse, "Current limitations of SEM and AFM metrology for the characterization of 3D nanostructures," *Measurement Science and Technology*, vol. 22, no. 9, Article ID 094003, 2011.

- [93] T. Fukuda, F. Arai, and L. Dong, "Assembly of nanodevices with carbon nanotubes through nanorobotic manipulations," *Proceedings of the IEEE*, vol. 91, no. 11, pp. 1803–1818, 2003.
- [94] M. R. Mikczinski, G. Josefsson, G. Chinga-Carrasco, E. K. Gamstedt, and S. Fatikow, "Nanorobotic testing to assess the stiffness properties of nanopaper," *IEEE Transactions on Robotics*, vol. 30, no. 1, pp. 115–119, 2014.
- [95] S. Zimmermann, V. Eichhorn, and S. Fatikow, "Nanorobotic transfer and characterization of graphene flakes," in *Proceedings of the 25th IEEE/RSJ International Conference on Robotics and Intelligent Systems, IROS 2012*, pp. 640–645, October 2012.
- [96] Z. Yang, P. Wang, Y. Shen et al., "Dual-MWCNT probe thermal sensor assembly and evaluation based on nanorobotic manipulation inside a field-emission-scanning electron microscope," *International Journal of Advanced Robotic Systems*, vol. 12, 2015.
- [97] P. Liu, K. Kantola, T. Fukuda, and F. Arai, "Nanoassembly of nanostructures by cutting, bending and soldering of carbon nanotubes with electron beam," *Journal of Nanoscience and Nanotechnology*, vol. 9, no. 5, pp. 3040–3045, 2009.
- [98] M. R. Ahmad, M. Nakajima, S. Kojima, M. Homma, and T. Fukuda, "The effects of cell sizes, environmental conditions, and growth phases on the strength of individual W303 yeast cells inside ESEM," *IEEE Transactions on NanoBioscience*, vol. 7, no. 3, pp. 185–193, 2008.
- [99] M. R. Ahmad, M. Nakajima, S. Kojima, M. Homma, and T. Fukuda, "Buckling nanoneedle for characterizing single cells mechanics inside environmental SEM," *IEEE Transactions on Nanotechnology*, vol. 10, no. 2, pp. 226–236, 2011.

Research Article

Electron Beam Irradiation Induced Multiwalled Carbon Nanotubes Fusion inside SEM

Daming Shen,^{1,2} Donglei Chen,¹ Zhan Yang,¹ Huicong Liu,¹ Tao Chen,¹ Lining Sun,¹ and Toshio Fukuda³

¹Robotics and Microsystem Center, Soochow University, Suzhou 215006, China

²School of Mechatronics Engineering, Harbin University of Science and Technology, Harbin 150080, China

³Department of Micro-Nano Systems Engineering, Nagoya University, Nagoya 464-0814, Japan

Correspondence should be addressed to Zhan Yang; yangzhan@suda.edu.cn and Huicong Liu; hcliu078@suda.edu.cn

Received 12 May 2017; Revised 9 August 2017; Accepted 30 August 2017; Published 23 October 2017

Academic Editor: Xinyu Liu

Copyright © 2017 Daming Shen et al. This is an open access article distributed under the Creative Commons Attribution License, which permits unrestricted use, distribution, and reproduction in any medium, provided the original work is properly cited.

This paper reported a method of multiwalled carbon nanotubes (MWCNTs) fusion inside a scanning electron microscope (SEM). A CNT was picked up by nanorobotics manipulator system which was constructed in SEM with 21 DOFs and 1 nm resolution. The CNT was picked up and placed on two manipulators. The tensile force was 140 nN when the CNT was pulled into two parts. Then, two parts of the CNT were connected to each other by two manipulators. The adhered force between two parts was measured to be about 20 nN. When the two parts of CNT were connected again, the contact area was fused by focused electron beam irradiation for 3 minutes. The tensile force of the junction was measured to be about 100 nN. However, after fusion, the tensile force was five times larger than the tensile force connected only by van der Waals force. This force was 70 percent of the tensile force before pulling out of CNTs. The results revealed that the electron beam irradiation was a promising method for CNT fusion. We hope this technology will be applied to nanoelectronics in the near future.

1. Introduction

The gate scale of the transistor of integrated circuit (IC) chip is down to 10 nm. With the introduction of sub-10 nm transistor, the scaling trend of transistor with silicon eventually reaches its physical limitation [1]. The quantum chipping effects become more prominent as the length of channel between source and drain was reduced to several nanometers. With photolithography and advanced ultraviolet etching processing technology, central processing unit (CPU) and graphic processing unit (GPU) were integrated within hundreds of billions of transistors. They reduced the processor's thermal power consumption and enhanced the processor frequency significantly [2]. In recent years, carbon nanotube, which was discovered by Raghavan in 1991 [3], attracted great interest of not only researcher but also manufacturing engineer on a conductive channel for the transistor less than 10 nm. The multiwalled carbon nanotube consisted of rotation of individual graphene sheets with

respect to the needle axes [4]. Carbon nanotubes were noticed greatly because of their exceptional electrical, mechanical properties and unique electronic transport characteristics [5, 6]. It is expected that these properties will be used by employing carbon nanotubes as structural or electrical components. Some major companies in the world such as IBM Corporation [7] and Intel Corporation [8] proposed a new process of carbon nanotube. CNT had a similar molecular structure to the graphene, which consisted of a hexagonal lattice of carbon atoms [9]. The carriers in the CNT can move freely in each graphene sheet because of ballistic transport [10]. It is on the order of 10^9 A/cm², which is three orders of magnitude larger than Cu [11]. The current density of CNT field-effect transistor (FET) was four times more than that of the best silicon devices. In addition, it was performed at a low operating voltage. With the scale of transistors becoming smaller, the switching speed will be improved significantly [12]. Copper as the traditional conducting material was more vulnerable to electromigration

damage [13]. Copper resistivity increases due to electron scattering at the surface. By this transport form of electrons, the current density of carbon nanotube was two or three orders of magnitude higher than that of Cu [14], making CNT an ideal material for nanodevice and electronic circuits.

The carbon nanotube interconnection technology is a crucial part for structure manufacture and functional device preparation and assembly. The quality of the connection directly determines the reliability of the functional device. The existing interconnection methods include chemical vapor deposition (CVD), high energy beam irradiation technology, arc discharge, and ultrasonic vibration interconnecting technology [15]. During the conventional processing, it was not possible to realize valid pick-up and alignment of carbon nanotube in three-dimensional space. Besides, carbon nanotubes were not interconnected by appropriate methods. To solve these problems, some scholars have designed and developed the nano operating system. Fukuda et al. constructed a nanorobotic manipulation system consisting of 4 operation units with 16 DOFs [16]. This system can be used for nanomanipulation and nanoassembly. Ru et al. demonstrated a 4-probe automated nanomanipulation system inside an SEM for a nanomanipulation task [17]. In IC manufacturing, CNT can be placed through boom-up technology [18]. It can effectively solve the problem which the top-down fabrication processing is faced with.

Over these years, CNT was proven to have potential application in large-scale integration interconnection. Nanometer-scale electronic device has been realized and widely applied in computer chips, tiny wires, and so on by many interconnection methods of carbon nanotubes [19]. Over the decades, the nanodevices [20–22] have made great breakthrough due to interconnection technology. The interconnecting technology has become the key component in nanodevices manufacture. Wu's Group successfully welded double-walled CNTs inside the vacuum tube by vacuum brazing of CNTs with a eutectic alloy (AgxCu_y) doped with Ti. The interconnection process needed low cost and the contact resistance was low [23]. Krashennnikov et al. performed MD simulations of ion irradiation induced CNT welding [24] and showed how this approach could be used to solder CNTs. However, the energy was consumed with time going on. Chen and Zhang showed that the focused electron beam in a scanning electron microscope (SEM) can be used to deposit a small amount of hydrocarbon contamination so as to attach the tubes on an AFM tip [25]. The adhesion was large enough that the CNT was attached on the AFM tip firmly. However, the experimental devices were contaminated during the interconnection process. Peng et al. synthesized branching structures of H-junctions and multiple Y-junctions CNT using a thermal chemical vapor deposition method [26]. The spatial resolution, flexibility, and controllability of welds between individual nanowires and nanoobjects were improved radically by this method.

Fedorov et al. applied focused-electron-beam-induced capabilities to fuse CNT with electrode [27]. It would have a direct positive impact on enhancing functionality, improving quality, and reducing fabrication costs for electronic devices. These methods destructed the properties of CNTs to some

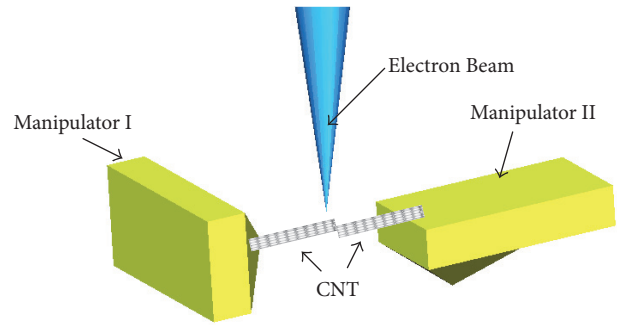


FIGURE 1: The schematic diagram of fusion method by electron beam irradiation.

degree. It is introduced that the nanotubes are connected by the fusion C-C bonds and the interconnection was stronger than the previous CNTs connected without fusion. What is more, this method has some advantages over any other methods [28]. The carbon nanotube interconnecting technology has no contamination. Nanodevices can be in mass production with interconnecting carbon nanotubes [29]. There is no need of other materials during the process of fusing the C-C bond with electron beam [30]. Study has shown that the carbon nanotubes can be connected at any angle and integrated into complex constructions by nanomanipulation [31]. This carbon nanotube interconnection technology can advance the development of small-scale device. However, the carbon nanotubes were not interconnected precisely. These methods changed the surface resistance of interconnected carbon nanotubes. These involved issues were not solved effectively by the above-mentioned interconnection methods.

This paper presented a method to interconnect carbon nanotube with electron beam to fuse the C-C bond. The carbon nanotubes were picked up and aligned effectively by nanomanipulators. With the development of semiconductor technology, the size of nanodevices is getting smaller and smaller. Effective interconnection of semiconductors has become a major challenge. In future industrial application, large quantities of carbon nanotubes can be fused by electron beam irradiation. The mass production will be achieved by this method. The whole operations were finished in the scanning electron microscope (SEM). We designed three experimental categories to compare fusion effect. In order to study the influences of the irradiation time and the magnification of observation on fusion, the deflection of the AFM should be observed and recorded seriously during the experiment. The effects of these factors were figured out, respectively, through the curves obtained in the experiment. Figure 1 shows a schematic diagram of fusion method by electron beam irradiation of the MWCNTs.

2. Experimental Set-Up

The experimental system was designed to study these issues in the SEM. Figure 2 shows the configuration of the system set-up for nanorobotics manipulation with 21 DOFs. The SEM (Zeiss, MERLIN Compact, resolution: 1.5 nm) was

TABLE 1: Parameters of each nanorobotics manipulator.

Parameters	Unit 1	Unit 2	Unit 3	Unit 4
Model	SLC-1720-s/8301-UHV	SLC-1720-s/8301-UHV	TSDS-255C/8301-UHV	TSDS-255C/8301-UHV
Dimensions (mm)	33 * 33 * 30.5/63.5 * 32.2 * 56.5	33 * 33 * 30.5/63.5 * 32.2 * 56.5	66 * 66 * 45/63.5 * 32.2 * 56.5	66 * 66 * 45/63.5 * 32.2 * 56.5
Travel (mm)	X ± 6, Y ± 6, Z ± 6	X ± 6, Y ± 6, Z ± 6	XY ± 3, Z ± 3	XY ± 3, Z ± 3
Rotate	-360°~+360°	-360°~+360°	-360°~+360°	-360°~+360°
Linear resolution	1 nm	1 nm	30 nm	30 nm
Rotate resolution	<1 microrad	<1 microrad	<1 microrad	<1 microrad

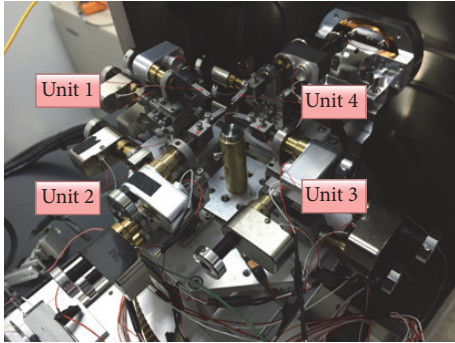


FIGURE 2: An image of the nanorobotics manipulation system.

introduced to observe the whole nanomanipulation process that was conducted in the vacuum chamber of the SEM (Table 1). In this system, Unit 1, Unit 2, and Unit 3 were used to operate the nanomanipulation. Unit 1 and Unit 2 (SmarAct, SLC-1720-s) with a resolution of 1 nm shown in Figure 2 were four-axe micromanipulators. Unit 3 consisted of the Picomotor (New Focus, 8301-UHV) and a three-dimensional micromotion stage (Sigma, TSDS-255C) with a resolution of 30 nm to move the CNT bulk. The grippers were designed to fix the AFM cantilever (Olympus, OMCL-TR400PB-1). The AFM was applied to pick up carbon nanotubes from CNT bulk. The carbon nanotubes that were fixed on the AFM cantilever tip were driven by a manipulator. And the moving step of the AFM was set at 5 nm step.

The procedure of the experiment was shown as follows.

The first step was to pick up a MWCNT. The picked up carbon nanotube was fixed on cantilever 2 as shown in Figure 3(a) and the distance between the two ends of the carbon nanotube was measured.

The second step was to connect the MWCNTs. Cantilever 2 was driven rightwards. The MWCNT was pulled into two parts. The two ends of the distance were recorded when the MWCNT was broken into two parts as shown in Figure 3(b). During the pulling process, the MWCNT was separated into two parts. After the pulling, the total length of the two parts was beyond the previous MWCNT.

The third step was to fuse the MWCNTs. Cantilever 2 was moved with 10 nm step to connect two parts of the CNT. The manipulators stopped moving when the two breaking points of the CNT touched each other. The joint was fused by electron beam irradiation as shown in Figure 3(c). The

accelerating voltage was applied to 5 kV and the beam current was 30 pA. The C-C bond of the two MWCNTs where they were in contact together was fused by the electron beam. Two MWCNTs were irradiated for 3 minutes and the magnification was kept at 5000. Before breaking, we recorded the distance of the two joints on the AFMs.

The fourth step was to pull the MWCNTs again. The deflection of cantilever 1 was recorded when the fused MWCNTs broke up as shown in Figure 3(d).

The fifth step was to connect again. The connection force was van der Waals force as shown in Figure 3(e). As soon as they connected, the extra high tension (EHT) was set off for 3 minutes for comparison with the CNT which was fused by electron beam irradiation.

In the following procedure, the connected MWCNTs were pulled again and the deflection of cantilever 1 was recorded when the MWCNTs separated apart.

3. Experimental Result

As shown in Figure 4(a), the MWCNT picked up from the bulk was set on the two manipulators (cantilever 1 and cantilever 2). In the SEM, the length of the MWCNT in the beginning of the experiment was measured at 11.81 μm and the diameter was 39.46 nm. The original distance of the two joints was 11.24 μm . In Figure 4(b), the MWCNT was dragged into two parts and the lengths of the parts were 3 μm and 13.7 μm , respectively. The distance between the two joints was 18.16 μm . The tensile force was calculated to be 140 nN. As Figures 4(c) and 4(d) show, the MWCNT was fused by electron beam irradiation. After that, the fused MWCNT was pulled off again and van der Waals force was calculated to be 12.6 nN. In Figures 4(e) and 4(f), the dragged MWCNT was interconnected and dragged again. When the CNT was interconnected and dragged, the distances of the two ends were 14.22 μm and 18.29 μm , respectively. It was found that the tensile force after fusion was 81.4 nN, which was clearly larger than van der Waals force.

4. Discussion

The electron beam was emitted by the electron gun in the SEM irradiated at the joint of MWCNTs. This synthesis was controlled by the systems operating with atomic-scale precision which enabled positional selection at the desired place precisely. The dragged C-C bonds were at the end of

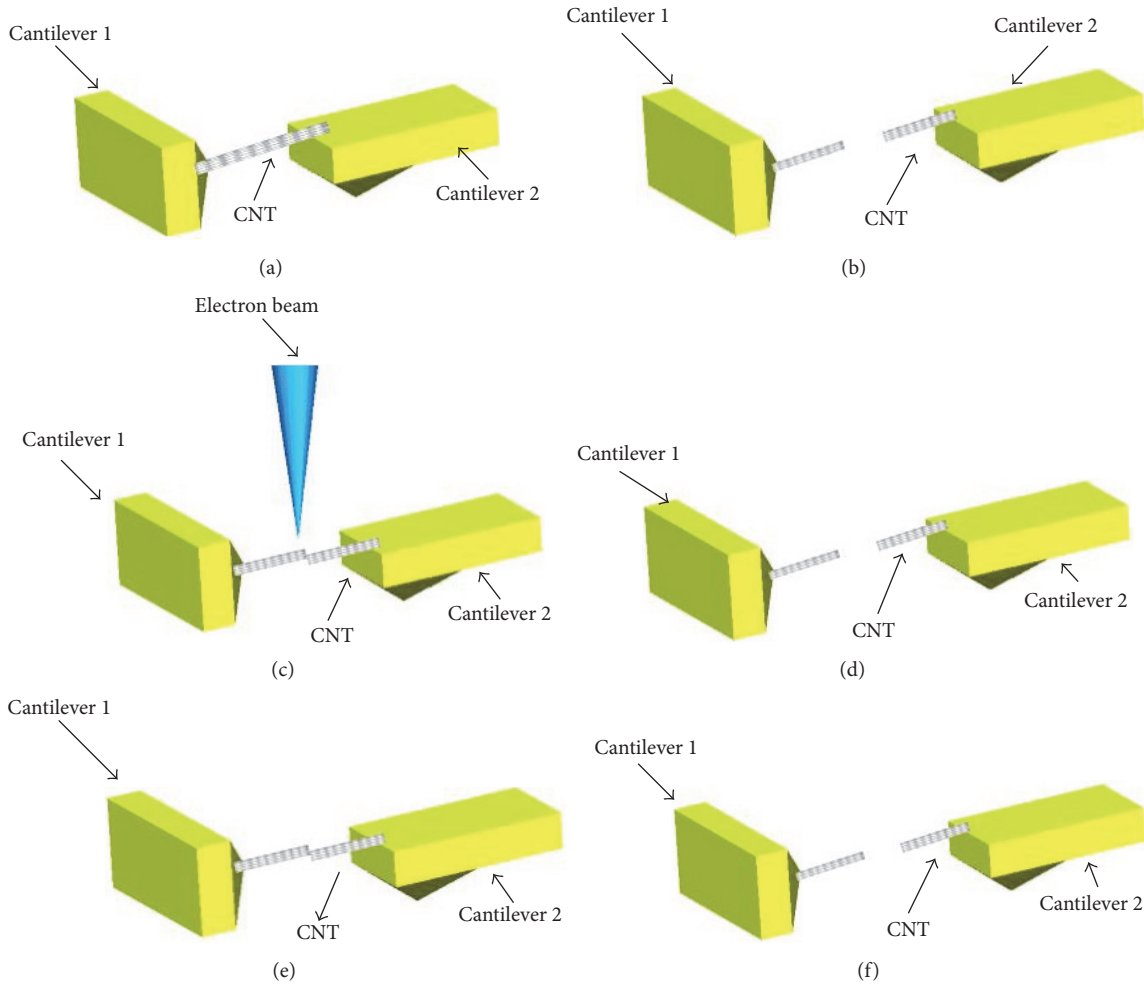


FIGURE 3: (a) The original position of the CNT. (b) Pulling the CNT until the nanotube breaks. (c) Fusing the CNT. (d) Pulling the CNT into two parts. (e) Connecting CNTs again without fusion. (f) Pulling the CNTs separated apart.

the MWCNTs. Because of the existence of the interatomic repulsive force, the fractured C-C bonds could not recover, when the dragged MWCNTs were interconnected. However, the electronic beam transferred to the orbital electrons of the carbon atoms. When the emitted electrons strike the joint, quantum photons generated from the electrons transferred energy to the low-energy orbit electrons. The low-energy orbit electrons would transit to the high-energy orbit; then their vibration frequency and range of the motion were increased. Under this circumstance, the possibility of C-C bonds formation was increasing which promoted lattice reconstruction of carbon atoms, so the properties would be the same as initial CNTs. Before this experiment, van der Waals force was calculated theoretically according to the following formula [28]:

$$W = \frac{A_s \pi C \rho_1 \rho_2}{12D^2}, \quad (1)$$

where C is the coefficient in the atom-atom pair potential; ρ_1 and ρ_2 are the numbers of atoms per unit volume in the interaction material. D is 0.34 nm, which is the vertical

distance of the attractive van der Waals force. A is the Hamaker constant between nanotubes [28]:

$$A = \pi^2 C p^2 = 2.842 \times 10^{-20} \text{ J}. \quad (2)$$

According to the tensile force formula, the force was calculated by Hooke's law [32]:

$$F = kd. \quad (3)$$

By comparing tensile force and van der Waals force, the tensile force was evidently larger. This result showed clearly that the fusion of carbon nanotubes could increase the tensile force significantly.

Assuming that the carbon nanotube was a multilayered cylinder, there were two interconnection ways. One was head to head configuration and the other was side to side configuration, as shown in Figures 5(a) and 5(b).

Figure 5(a) shows the head to head configuration. In this case, the centres of the two carbon nanotubes were connected and van der Waals force was the largest. The layers of the

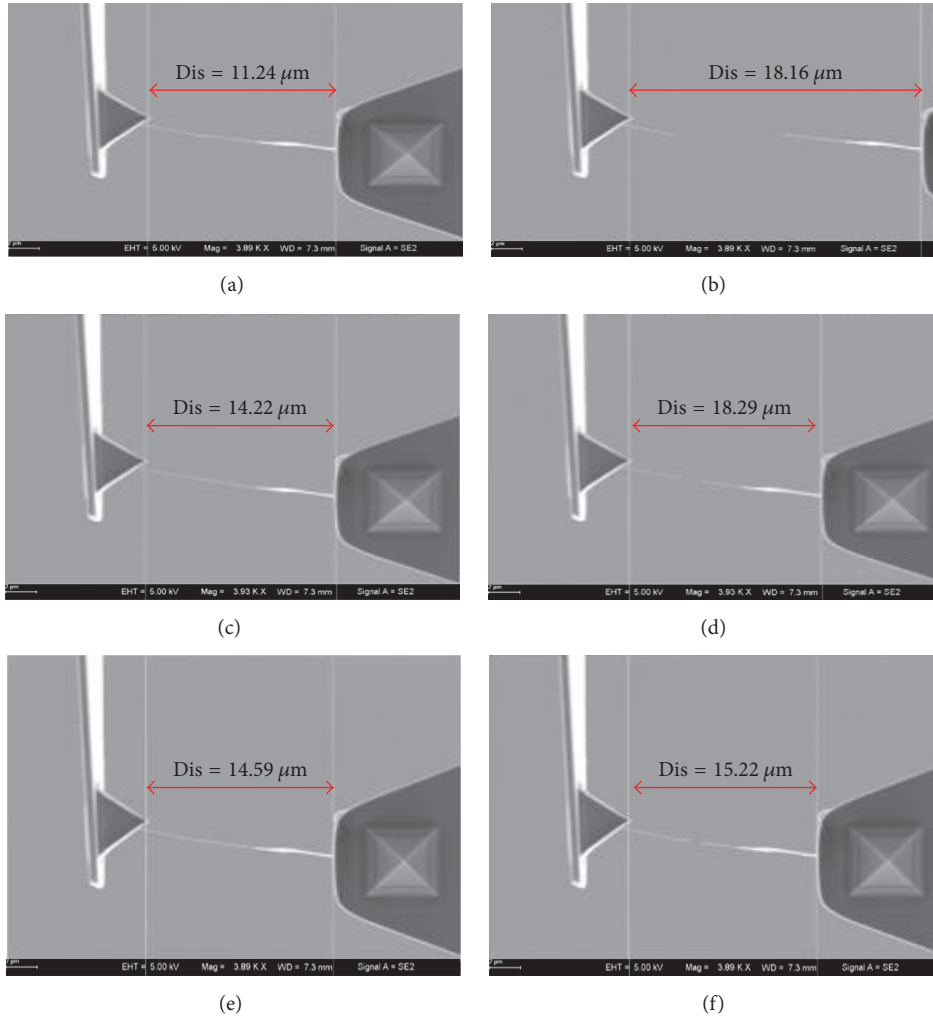


FIGURE 4: (a) The original distance of two ends of the CNT. (b) The distance when the CNT was dragged. (c) The distance of two ends of the fused CNT. (d) The distance when the fused CNT was dragged. (e) The distance of interconnecting the dragged CNT. (f) The distance of dragging the interconnected CNT.

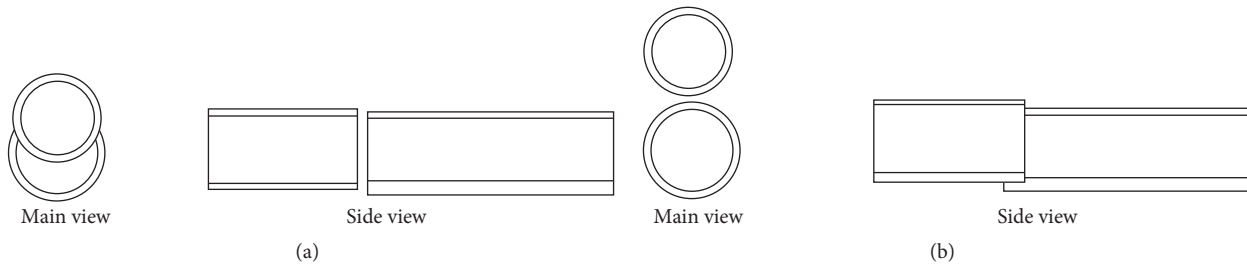


FIGURE 5: (a) Cross-sectional view and overhead view of head to head configuration of two carbon nanotubes. (b) Cross-sectional view and overhead view of side to side configuration of two carbon nanotubes.

carbon nanotubes were 58. The cross-sectional area can be calculated by the following relation equations [33]:

$$A_S = \sum_{n=1}^{n=58} \left[\pi (0.34 + 0.035 + 0.34n)^2 - \pi (0.34 - 0.035 + 0.34n)^2 \right] = 138 \text{ nm}^2. \quad (4)$$

According to the calculation, the area is 138 nm^2 . The value of the force was calculated to be 5.3 nN .

The other way of carbon nanotubes interconnection was side to side configuration. The strongest connection force was contained by the following equation [34]. The distance between two outer walls was 0.34 nm , s was the interfacial shear stress of nanotubes, which was 2 MPa ,

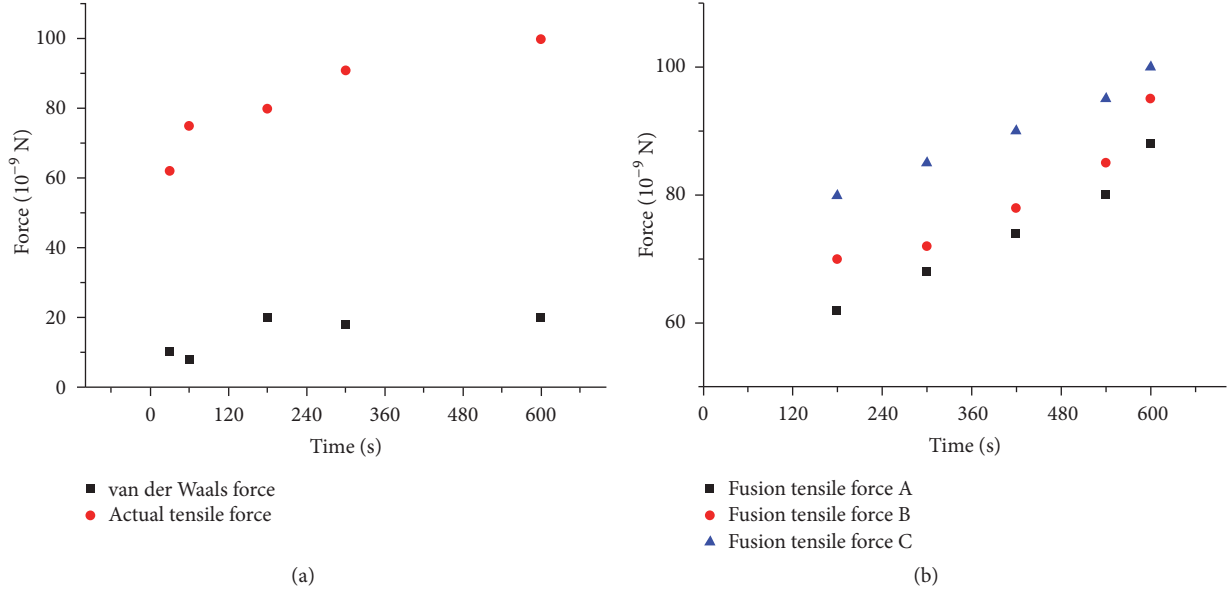


FIGURE 6: (a) F - T scatter diagram of actual tensile force and van der Waals force. (b) F - T curve of actual tensile force of different diameters of CNTs.

and w was the contact width of the MWCNTs, which was 100 nm.

$$F_v = swe_x = 6.8 \text{ nN}. \quad (5)$$

First, the two ends of MWCNTs were irradiated for some time. The deflection of the cantilever was tested after dragging the connected nanotube until the new joint broke. After connection, the extra high tension was shut down. When dragging the connected MWCNT, the extra high tension was turned on. The relationship between the forces and time was presented by the F - T scatter diagram in Figure 6(a). As irradiating time passed by, van der Waals force changed a little, demonstrating that the actual van der Waals force had nothing to do with the irradiating time.

After fusion, the actual tensile force was recorded. It obviously reflected the fusion effect by the F - T scatter diagram that was shown in Figure 6(a). The tensile force was significantly larger than van der Waals force. What is more, the longer the irradiation time was, the larger the actual tensile force was.

In order to rule out the fortuity, the experiment was divided into several groups by manipulating different diameters of CNTs to repeat the fusion and measure the fusion effect by deflection of AFM. The F - T scatter diagram of fusion tensile force was shown in Figure 6(b). The fusion effects were almost similar in three different MWCNTs. The electronic beam irradiation methods possessed universality in fusing graphene structure.

Another experiment was designed to verify the effects of different magnification on fusion. The irradiation time was set to 2 minutes under different magnification. The F - M curve was obtained by experiment. From Figure 7, the force became larger with the increase of magnification. When the magnification increased, the region of observation became

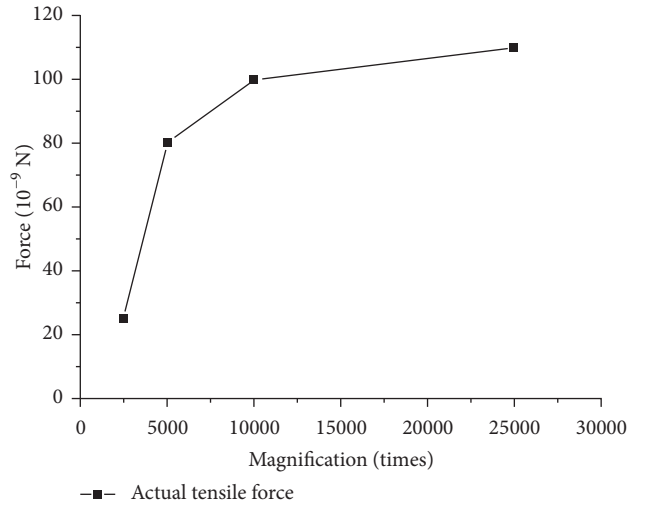


FIGURE 7: Force and magnification relationship curve of actual tensile force at different magnification times.

small with more electrons gathering. In this condition, more electrons emitted by electronic gun hit extranuclear electrons of carbon atom. The experiment demonstrated that a larger magnification had a better effect on fusion of carbon nanotubes.

It was observed that the force becomes larger with the magnification increasing. This phenomenon may be caused by the electric field imaging force. Thus, we calculated the force according to the formula and made the following chart [35]:

$$\lg(F_{ei}) = \lg\left(\frac{\pi}{4\epsilon_0} \frac{\epsilon - \epsilon_0}{\epsilon + \epsilon_0} d^2 \sigma^2\right), \quad (6)$$

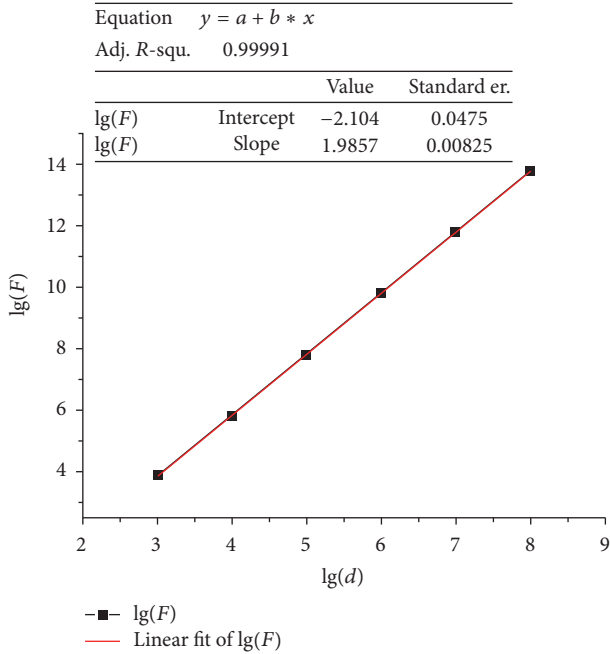


FIGURE 8: $\lg(F)$ and $\lg(d)$ relationship curve of electric field imaging force of CNTs with different diameters.

where d is the diameter of the sphere, ϵ_0 is dielectric coefficient of circumference, F_{ei} is the electrostatic force by electric imaging, and ϵ is the dielectric coefficient of the nanotube. $\epsilon_0 = 8.85 \times 10^{-12}$ [F/m]; $\epsilon = 5\epsilon_0$, $\sigma = 26.5$ [$\mu\text{C}/\text{m}^2$]. Figure 8 indicates the relationship between the electrostatic force and the diameter of carbon nanotube. The logarithm was adopted here so that linear calculations of the force were convenient. The electrostatic force of carbon nanotube with dozens of nanometers could be calculated by this graph of a function " $\lg(F) = 1.98\lg(d) - 2.10$." After calculation, we found that the diameter of the CNT was dozens of nanometers and the force was about 11 nN, while the fusion force was about 100 nN. The scale of the force was not an order of magnitude with the fusion force. Therefore, the force could be ignored. When the magnification time increased, the observation region became small with more electrons gathering. In summary, the force was the fusion force.

The fusion method of electronic beam irradiation was reliable. The fusion effect achieved 70 percent which was stronger than other methods and did not damage the original structure. The electron beam will indeed induce hydrocarbon. However, our experimental vacuum order was 10^{-4} Pa. At that point, the free path of hydrocarbon molecules was very large. The distance was calculated at several hundred meters theoretically. But the diameter of carbon nanotube was tens of nanometers. The amount of hydrocarbon accumulation absorbed on the surface of carbon nanotube was very small [36]. Therefore, we think that the hydrocarbon absorbed on the surface of carbon nanotubes can be neglected. The fusion point and location would be controlled.

5. Conclusion

This paper proposed a new method of the interconnection of carbon nanotubes. The tensile force of the fused carbon nanotubes was larger than van der Waals force. A C-C bond was newly generated because of the fusion by electron beam irradiation. This interconnection method can connect different-scale carbon nanotubes. Some small-scale electronic devices can be built by nanomanipulation with the development of technology. This method used to interconnect MWCNTs is sturdy because the actual tensile force increased only from 20 nN to 100 nN. In the future work, more efforts will be devoted to interconnect the MWCNTs by arbitrary angles to fabricate nanotransistor.

Conflicts of Interest

The authors declare that they have no conflicts of interest.

Acknowledgments

This work is supported by the National Natural Science Funds of China (Grant no. 61433010) and the National High Technology Research and Development Program ("863" Program) of China (Grant no. 2015AA042601).

References

- [1] Z. Yang, T. Chen, Y. Wang, L. Sun, and T. Fukuda, "Carbon nanotubes pickup by van der Waals force based on nanorobotics manipulation inside SEM," *Micro and Nano Letters*, vol. 11, no. 10, pp. 645–649, 2016.
- [2] B. T. Lewis, R. Barik, and T. Shpeisman, "Function callback mechanism between a central processing unit (CPU) and an auxiliary processor," 2016.
- [3] D. Raghavan, "Synthesis of Multi-walled Carbon Nanotubes by Plasma Enhanced Microwave Cvd Using Colloidal Form of Iron Oxide as a Catalyst," 1991.
- [4] S. Iijima, "Helical microtubules of graphitic carbon," *Nature*, vol. 354, no. 6348, pp. 56–58, 1991.
- [5] C. Lee, X. Wei, J. W. Kysar, and J. Hone, "Measurement of the elastic properties and intrinsic strength of monolayer graphene," *Science*, vol. 321, no. 5887, pp. 385–388, 2008.
- [6] B. Hoefflinger, "ITRS: The International Technology Roadmap for Semiconductors," in *Chips 2020*, pp. 161–174, Springer Berlin Heidelberg, Heidelberg, Germany, 2011.
- [7] A. D. Franklin, M. Luisier, S. J. Han et al., "Sub-10 nm carbon nanotube transistor," in *IEEE Proceedings of the Electron Devices Meeting*, pp. 23.7.1–23.7.3, 2012.
- [8] B. Liu, Z. Cao, J. Tao, X. Zeng, P. Tang, and P. H.-S. Wong, "Intel LVS logic as a combinational logic paradigm in CNT technology," in *Proceedings of the 2010 IEEE/ACM International Symposium on Nanoscale Architectures, NANOARCH 2010*, pp. 77–81, Anaheim, CA, USA, June 2010.
- [9] M. I. Katsnelson, "Graphene: carbon in two dimensions," *Materials Today*, vol. 10, no. 1-2, pp. 20–27, 2007.
- [10] H. J. Li, W. G. Lu, X. D. Bai et al., "Multi-channel ballistic transport in multi-wall carbon nanotubes," *Physical Review Letters*, vol. 95, no. 8, Article ID 086601, 2005.

- [11] H. Li, N. Srivastava, J.-F. Mao, W.-Y. Yin, and K. Banerjee, "Carbon nanotube vias: Does ballistic electron-phonon transport imply improved performance and reliability?" *IEEE Transactions on Electron Devices*, vol. 58, no. 8, pp. 2689–2701, 2011.
- [12] L. C. T. Shoute, Y. Wu, and R. L. McCreery, "Direct spectroscopic monitoring of conductance switching in polythiophene memory devices," *Electrochimica Acta*, vol. 110, pp. 437–445, 2013.
- [13] A. Naeemi, R. Sarvari, and J. D. Meindl, "Performance comparison between carbon nanotube and copper interconnects for gigascale integration (GSI)," *IEEE Electron Device Letters*, vol. 26, no. 2, pp. 84–86, 2005.
- [14] A. Kawabata, S. Sato, T. Nozue et al., "Robustness of CNT Via Interconnect Fabricated by Low Temperature Process over a High-Density Current," in *Proceedings of the 2008 International Interconnect Technology Conference - IITC*, pp. 237–239, Burlingame, CA, USA, June 2008.
- [15] L. J. Yang, J. L. Cui, W. Yang et al., "Research progress on the interconnection of carbon nanotubes," *Xinxing Tan Cailiao/New Carbon Materials*, vol. 100, no. 1, p. 710, 2016.
- [16] T. Fukuda, F. Arai, and L. Dong, "Micro and Nano Robotic Manipulation Systems," 2009.
- [17] C. Ru, Y. Zhang, Y. Sun et al., "Automated four-point probe measurement of nanowires inside a scanning electron microscope," *IEEE Transactions on Nanotechnology*, vol. 10, no. 4, pp. 674–681, 2011.
- [18] E. Oyarzua, J. H. Walther, A. Mejía et al., "Early regimes of water capillary flow in slit silica nanochannels," *Physical Chemistry Chemical Physics Pccp*, vol. 17, no. 22, p. 14731, 2015.
- [19] C. L. Kane and E. J. Mele, "Size, shape, and low energy electronic structure of carbon nanotubes," *Physical Review Letters*, vol. 78, no. 10, pp. 1932–1935, 1997.
- [20] R. H. Baughman, A. A. Zakhidov, and W. A. De Heer, "Carbon nanotubes—the route toward applications," *Science*, vol. 297, no. 5582, pp. 787–792, 2002.
- [21] D. Galpaya et al., "Carbon nanotubes : synthesis, structure, properties, and applications," *Journal of Applied Physics*, vol. 116, no. 5, Article ID 05351810, 2001.
- [22] Y.-P. Sun, K. Fu, Y. Lin, and W. Huang, "Functionalized carbon nanotubes: properties and applications," *Accounts of Chemical Research*, vol. 35, no. 12, pp. 1096–1104, 2002.
- [23] W. Wu, A. Hu, X. Li et al., "Vacuum brazing of carbon nanotube bundles," *Materials Letters*, vol. 62, no. 30, pp. 4486–4488, 2008.
- [24] A. V. Krasheninnikov, K. Nordlund, J. Keinonen et al., "Ion-irradiation induced welding of carbon nanotubes," *Physical Review B Condensed Matter*, vol. 66, no. 24, Article ID 245503, 2002.
- [25] C. Chen and Y. Zhang, "Ultrasonic nanowelding technology between carbon nanotubes and metal electrodes," in *Nanowelded Carbon Nanotubes*, pp. 47–62, Springer, Berlin, Germany, 2009.
- [26] Y. Peng, T. Cullis, and B. Lnkson, "Bottom-up nanoconstruction by the welding of individual metallic nanoobjects using nanoscale solder," *Nano Letters*, vol. 9, no. 1, pp. 91–96, 2009.
- [27] A. G. Fedorov, S. Kim, M. Henry, D. Kulkarni, and V. V. Tsukruk, "Focused-electron-beam-induced processing (FEBIP) for emerging applications in carbon nanoelectronics," *Applied Physics A: Materials Science and Processing*, vol. 117, no. 4, pp. 1659–1674, 2014.
- [28] T. Fukuda, F. Arai, and L. Dong, "Assembly of nanodevices with carbon nanotubes through nanorobotic manipulations," *Proceedings of the IEEE*, vol. 91, no. 11, pp. 1803–1818, 2003.
- [29] J. Jiao and D. McClain, "Overcoming obstacles for developing carbon nanotube-based devices," in *proceedings of the Vacuum Electron Sources Conference and Nanocarbon*, p. 14, IEEE, Nanjing, China, 2010.
- [30] I. Jang, S. B. Sinnott, D. Danailov, and P. Keblinski, "Molecular Dynamics Simulation Study of Carbon Nanotube Welding under Electron Beam Irradiation," *Nano Letters*, vol. 4, no. 1, pp. 109–114, 2004.
- [31] Y. Zhu, S. Murali, W. Cai et al., "Graphene and graphene oxide: synthesis, properties, and applications," *Advanced Materials*, vol. 22, no. 35, pp. 3906–3924, 2010.
- [32] R. S. Rivlin, "Large Elastic Deformations of Isotropic Materials. I. Fundamental Concepts," *Philosophical Transactions of the Royal Society A Mathematical Physical & Engineering Sciences*, vol. 240, no. 822, pp. 459–490, 1997.
- [33] Z. Yang, *Fabrication, Assembly and Application for Functional Nanodevices based on Nanorobotic Manipulation*, Nagoya University, 2013.
- [34] M. R. Falvo, R. M. Taylor II, A. Helsen et al., "Nanometre-scale rolling and sliding of carbon nanotubes," *Nature*, vol. 397, no. 6716, pp. 236–238, 1999.
- [35] D. Lixin, *Nanorobotic Manipulations of Carbon Nanotubes*, Nagoya University, 2002.
- [36] R. W. Walters and R. G. Luthy, "Rebuttal to: "Equilibrium adsorption of polycyclic aromatic hydrocarbons from water onto activated carbon," *Environmental Science & Technology*, vol. 19, no. 9, pp. 870–871, 1985.

Research Article

In Situ SEM Torsion Test of Metallic Glass Microwires Based on Micro Robotic Manipulation

Chenchen Jiang,^{1,2} Haojian Lu,¹ Ke Cao,¹ Wenfeng Wan,¹ Yajing Shen,^{1,3} and Yang Lu^{1,2}

¹Department of Mechanical and Biomedical Engineering, City University of Hong Kong, Kowloon, Hong Kong

²Center for Advanced Structural Materials (CASM), Shenzhen Research Institute, City University of Hong Kong, Shenzhen 518057, China

³Centre for Robotics and Automation, Shenzhen Research Institute, City University of Hong Kong, Shenzhen 518057, China

Correspondence should be addressed to Yajing Shen; yajishen@cityu.edu.hk and Yang Lu; yanglu@cityu.edu.hk

Received 24 March 2017; Accepted 25 July 2017; Published 23 August 2017

Academic Editor: Nicolas Delorme

Copyright © 2017 Chenchen Jiang et al. This is an open access article distributed under the Creative Commons Attribution License, which permits unrestricted use, distribution, and reproduction in any medium, provided the original work is properly cited.

Microwires, such as metallic, semiconductor, and polymer microwires and carbon fibers, have stimulated great interest due to their importance in various structural and functional applications. Particularly, metallic glass (MG) microwires, because of their amorphous atoms arrangement, have some unique mechanical properties compared with traditional metals. Despite the fact that substantial research efforts have been made on the mechanical characterizations of metallic glass microwires under tension or flexural bending, the mechanical properties of microwires under torsional loading have not been well studied, mainly due to the experimental difficulties, such as the detection of torsion angle, quantitative measurement of the torsional load, and the alignment between the specimen and torque meter. In this work, we implemented the in situ SEM torsion tests of individual $\text{La}_{50}\text{Al}_{30}\text{Ni}_{20}$ metallic glass (MG) microwires successfully based on a self-developed micro robotic mechanical testing system. Unprecedented details, such as the revolving vein-pattern along the torsion direction on MG microwires fracture surface, were revealed. Our platform could provide critical insights into understanding the deformation mechanisms of other microwires under torsional loading and can even be further used for robotic micromanufacturing.

1. Introduction

Microwires, such as metallic [1, 2], semiconducting [3, 4], and composite microwire [5, 6], biomaterial fiber [7], and carbon fiber [8, 9], have unusual mechanical and physical properties, making them promising for various mechatronic applications in micro electronics devices [10] or solar cells [11]. For example, polymer microwires with high elasticity even can function as a spring element to produce jumping or flapping motions in microrobots [12]. ZnO microwires, on the other hand, which have unique piezoelectric property, have been demonstrated to act as microsensor or field effect transistor [13]. Among those crystalline and non-crystalline microstructured materials, BMG (bulk metallic glass) has received tremendous research attention because of its unique physical and mechanical properties such as ultrahigh strength, high hardness, and large elastic strain [14, 15] due to the amorphous state of the atoms. Compared

with the normal metals having crystalline lattice structures, which can facilitate dislocation movement under stress, making them soft and ductile, MGs, on the other hand, are normally hard and brittle at bulk scales [16]. Recently, MG microwires have received increased interests due to their different properties compared to their bulk counterparts; for instance, magnetic metallic glass microwires exhibit extremely soft magnetic behavior because of the absence of magnetocrystalline anisotropy, grain boundaries, and crystalline structure defects [17–20]. However, in-depth understanding of the mechanical properties of these novel MG micromaterials is still necessary for developing new applications, such as micro/nanoelectromechanical system (MEMS/NEMS) devices [21], heterogeneous catalysts [22], and magnetic sensors [23]. What is more, as the various microwires' applications circumstances have become complicated, the mechanical property of these materials has become a bottleneck constraint for long service time.

Although there have been extensive studies on the mechanical behavior of microwire materials in the past two decades, such as static tensile test [24–27], micro/nanoindentation measurement [28–30], bending measurement [31–33], and dynamic resonance frequency fatigue test [34, 35], little was reported on the behavior of microwire under the torsional loading [36–38]. Torsion of thin wires is a fundamental and excellent approach to explore the mechanical behavior, from elastic deformation, through yielding, to the strain-hardening regime. The reason for the rareness of torsion test of microwire was the great challenge involved in the experiment, such as the alignment between the specimen and the rotation axis, the detection of torsion angle, and the sensibility and calibration of torque meter. In this paper, we investigated the torsion fracture behavior of the $\text{La}_{50}\text{Al}_{30}\text{Ni}_{20}$ MG microwire under in situ SEM and compared the fracture surface with tensile loading test [24–26] based on a self-developed micro robotic mechanical testing system. After analyzing the pattern on the fracture surface, the fracture mechanism of the microwire under torsion loading was proposed. The fracture resulted from the fact that the local temperature became very high to the melting point of the MG material and a fluid layer was generated; then the nucleated nano/microvoid caused the failure. The interesting revolved vein-pattern microstructures were firstly observed by the robot system we developed which we believe can be used in many other applications in the future, for example, micro assembly of nanoelectronic devices.

2. Sample and Experimental Procedures

2.1. MG Microwire Preparation. The metallic glass (MG) microwire samples (dia. $70\ \mu\text{m}$) used in this work are fabricated by rapid quenching of alloy proportions from their liquid mixture. As the mechanical or magnetic property of the microwire is highly related to the microstructure of the materials [39, 40], the structure and composition should be confirmed before experiment. The chemical composition of the metallic glass is evaluated through the energy dispersive X-ray spectroscopy (EDS) studies carried out on the MG microwires, which reaffirmed the composition to be approximately $\text{La}_{50}\text{Al}_{30}\text{Ni}_{20}$ (in atomic%). X-ray diffraction (XRD) studies on the MG microwires were carried out to confirm the amorphous nature of the material.

2.2. Micro Robotic Mechanical Testing System. The self-developed micro robotic mechanical testing system is illustrated in Figure 1(a). The robot mainly comprised two parts [41–43]. The left motion part includes a rotary positioner and two linear positioners. If we set the world coordinate as Figure 1(a) shows, the rotation axis is along the Z direction. Upon the rotary positioner (RP), the linear positioner (LP_1) which moves in Y direction is joined. Then another linear positioner (LP_2) that moves in X direction is connected to the first one. LP_1 and LP_2's movement directions are mutually perpendicular. Each nanopositioner of the robot is responsible for one independent movement; thereby the left part of the robot has three degrees of freedom (DOFs) in total: two mutually perpendicular translational movements

(along X and Y directions, resp.) and one rotation (the rotation axis is along z -axis). The right part includes three linear positioners, which can move independently in X , Y , Z directions, as Figure 1(a) shows. A metal basement is used to fix the two parts. Additionally, two T-shape stages were fabricated to clamp the sample at each side as the inset image shows. With the small footprint of the robot setup, it is suitable for SEM chamber for in situ experiment, as shown by Figure 1(b).

As to the parameters of the positioners, the travel range, resolution, and repeatability for the rotary positioner RP are 360° endless, $(1 \times 10^{-6})^\circ$ and 5% over the full range, respectively. The travel range, resolution, and repeatability of the linear positioners are 20 mm, 1 nm, and 50 nm, respectively. Due to their high accuracy, the compact drive units can achieve the challenging positioning task of precise alignment in torsion test.

2.3. Experimental Setup. At first, the MG microwire sample was fixed between the T-shape stage on the left part and the metal plate by screwing. Then the robot was put in the SEM chamber and connected with the control box through the port. Because the SEM imaging system can only provide the 2D image information, it is very difficult to obtain the position of the sample directly based on the SEM images. An automatic forward-backward alignment strategy was proposed to address this challenge.

As shown in Figure 2(a), first microscope image is captured. Then rotate rotary positioner by α degrees so that the second microscope image can be captured. After that, rotate rotary positioner by 2α degrees so that the third microscope image can be captured. After these procedures, all the information for the sample alignment strategy has been obtained. Simplified coordinate diagram shows the calculation process of the proposed alignment principle. The detailed alignment strategy is illustrated in our previous work [44, 45]. After calculation, the movement of LP_1 and LP_2 is given as follows:

$$\begin{aligned} x_o &= \frac{\Delta x_p + \Delta x_n}{2(\cos \alpha - 1)} \\ y_o &= \frac{\Delta x_p - \Delta x_n}{2 \sin \alpha}. \end{aligned} \quad (1)$$

Before the sample alignment, when the micro robotic mechanical testing system rotates with angles -15° , 0° , and $+15^\circ$, as shown in Figure 2(b), the maximum position difference between the three images is $1009.089\ \mu\text{m}$. After the sample alignment, when the micro robotic mechanical testing system rotates with angles -90° , 0° , and $+90^\circ$, as depicted in Figure 2(c), the sample almost remains at the same position.

After aligning the sample along the axis of the rotation positioner, we control the T-shape stage on the right part of the robot to approach the freestanding side of the sample slowly. We can set the gap between the two stages as needed by using linear positioner at Z direction. Then we open the SEM chamber and fix the sample on the right T-shape stage also by screwing a metal plate for subsequent in situ SEM testing.

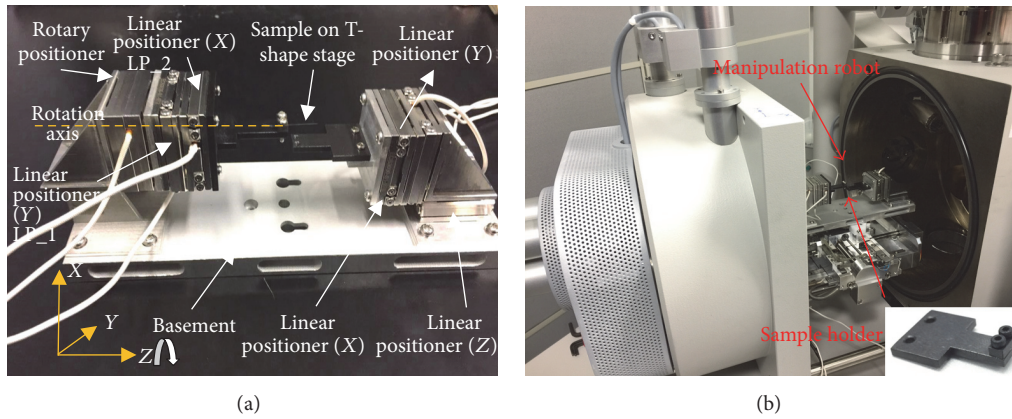


FIGURE 1: (a) is the photograph of the robot and the illustration of the different key parts. The rotation axis is along the Z direction of the world coordinate. (b) shows that the small footprint of the robot is suitable for the in situ SEM experiment. The inset image is magnification of the T-shape stage with screws used to clamp the sample.

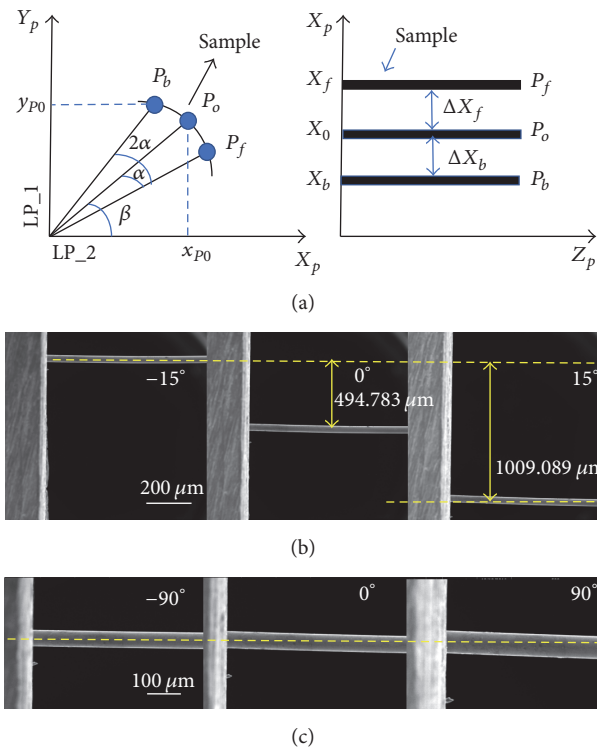


FIGURE 2: (a) Illustration of the alignment process. (b) The images captured from SEM at different angles can be used to calculate how much LP.1 and LP.2 have to move. (c) The alignment result shows that no matter how many rotations there are, the sample remains almost at the same position.

2.4. *Torsion Process inside SEM.* After the alignment and fixation process, we closed the SEM chamber and the robot pose in SEM was horizontal at the beginning as Figure 3(a) shows. The original whole sample configuration is shown in Figure 3(b). There was no preload to the sample. The gauge length was about $190 \mu\text{m}$. In order to judge whether the sample was being twisted, we selected two obvious markers (red rectangles A and B) on its surface. Then we twisted the sample through rotary positioner with rotation speed kept

unchanged at 5 deg/s and the twisting direction was anti-clockwise from the left side of view as shown in Figure 3(b). Figure 3(c) shows the robot setup during the torsion loading with torsion angle about 45° . From Figure 3(d), captured from the supplementary video (see Supplementary Material available online at <https://doi.org/10.1155/2017/6215691>), it is easy to find that part of the marker (A) rotated outside of the view and marker (B) almost stayed at the same place. The movement of the markers on the sample can indicate that

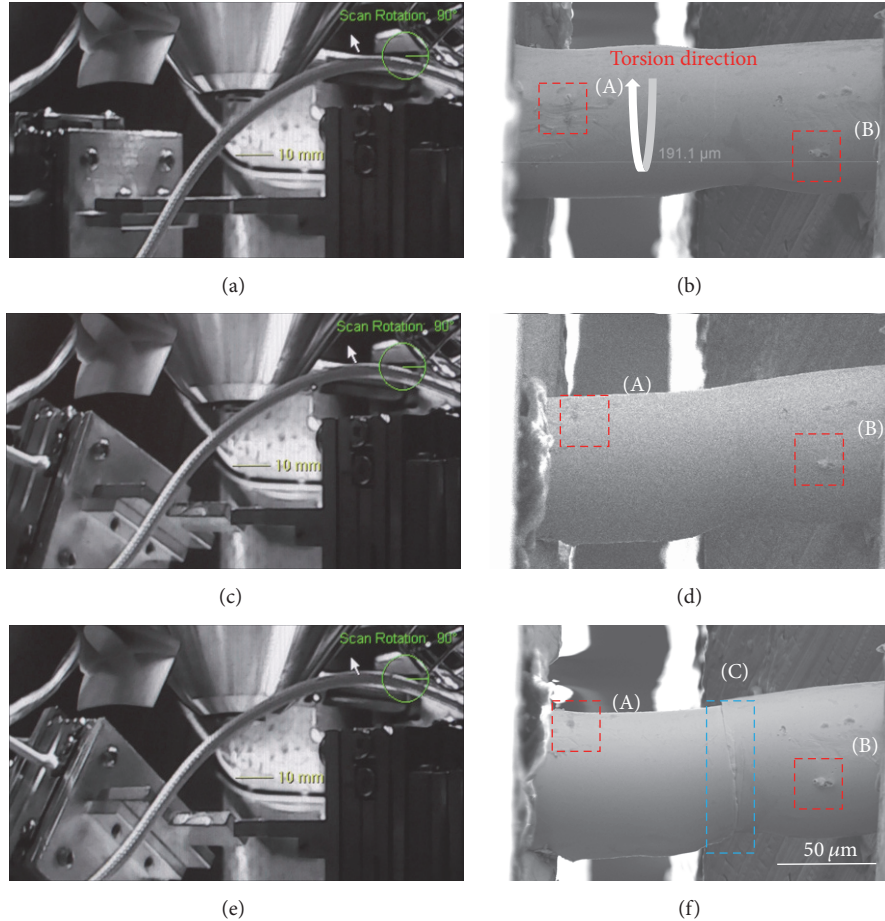


FIGURE 3: Images selected during the experiment. (a) is the robot pose at the beginning of the experiment. (b) is the sample configuration at the time of (a). The effective length of the sample was about $190 \mu\text{m}$. Two markers were selected on the surface to judge whether the rotation happened. The rotation direction was anticlockwise from the left side of view. (c) shows the robot pose during the torsion loading and the displacement of marker (A) was much more obvious than marker (B) as (d) shows. The sample fractured at about 55 degrees of rotation as shown in (e). (f) is the final morphology of the sample, which shows that the marker (A) moved a lot and the fracture happened at the middle part of the sample, partly because of the nonuniformity of the sample diameter or internal defects inside the microwire. The scale bar for the (b), (c), and (d) was $50 \mu\text{m}$.

the clamping was firm enough. Figures 3(e) and 3(f) were images to show the robot pose and sample morphology when fracture happened at 55° .

3. Results and Discussions

The shear strain can be calculated by $\gamma = \varphi * R/L$, in which φ indicates the rotation angle; R and L are the diameter and effective length of the microwire. According to the images captured during the experiment, the MG microwire (dia. $70 \mu\text{m}$) with length about $190 \mu\text{m}$ fractured at about 55 degrees of distortion, which means the maximum shear strain of the sample was about 17.6%. According to the rotation theory, the maximum shear strain located at the rightmost side of the sample between the clamp. However, the fracture that happened at the middle part of the sample may be because of the nonuniformity of the diameter or internal defects inside the microwire.

The overall fracture surfaces of the two sides of MG microwires are shown in Figures 4(a) and 4(c), from which we can easily identify that the vein-pattern microstructures, a typical fracture surface feature of glassy materials, revolved along with the twisting direction. They were different from the microstructure of the fracture surface after tensile loading (as shown in [24]), which means that the fracture was indeed caused by torsion loading. These vein-patterns bear the signature of liquid-like flow occurring inside MG materials. Upon magnification (Figures 4(b) and 4(d)), we also found that there were almost no localized shear bands on the sample fracture surfaces.

At the start period of torque exertion, the plastic deformation was prevented because of lacking structural dislocation, and the stress was usually confined to elastic regime. With the increase of stress, the plastic deformation was usually confined to extremely localized areas (plastic zones) in the material, which caused a rapid temperature rise while the

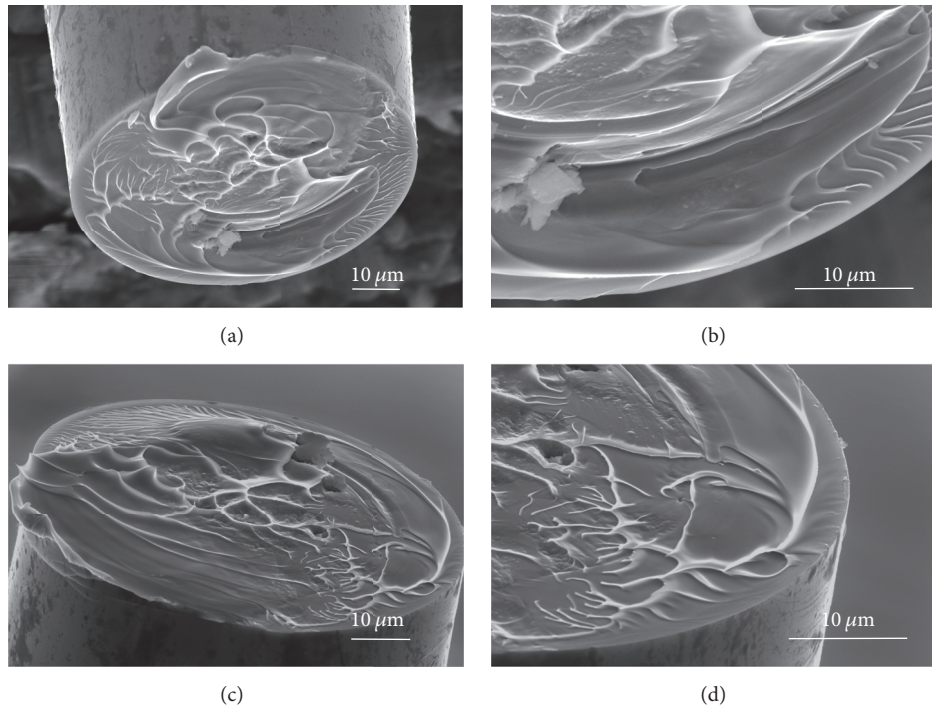


FIGURE 4: Microstructure of the fracture surface. (a) and (c) are the two corresponding sides at the fracture point. There are revolving vein-patterns on both of them. The magnification images of (b) and (d) show that the area between the corrugations is very flat and clean, which may be because the plastic deformation was confined to extremely small space inside metallic glass.

adiabatic heating leads to extremely fast events within a few hundred nanoseconds. The absence of necking in or around the fracture location as Figure 3(f) proved that the plastic deformation was localized at the fracture point. During this time, the material melted and a fluid layer was produced. The local density (as well as the viscosity) of the fluid layer was also changed, and intermixing of two liquids with different densities was responsible for producing such fractal-like patterns, possibly due to Rayleigh-Taylor instability [46].

With the increase of the torsion angle, the nano/microvoid nucleated, and the catastrophic failure happened at the final stage. The rapid cooling of viscous fluid layers leads to the formation of the revolving vein-patterns because of the torsion stress. Obviously, the revolving vein-pattern usually occurred near the edge of the microwire cross-section, as shown in Figure 4, which corresponded to the largest stress at that area. Because the torsion stress decreased towards the center of the microwire, the vein-pattern near it was similar to that of tensile loading.

Compared with the previous mechanical testing of the MG microwires, the presented micro robotic system can speed up the in situ sample alignment process and exert a controllable twist angle on the microwire. The small footprint of the setup is very suitable for in situ SEM mechanical testing, which can give more microstructural information about the fracture mechanism at real time than traditional tests. The robot system utilized the image processing algorithm to ensure the microwire can rotate along the rotary axis and the precise movement of the robot makes it possible to control the effective length of the microwire.

4. Conclusion

In this work, in situ SEM torsional tests on the $\text{La}_{50}\text{Al}_{30}\text{Ni}_{20}$ MG microwires were implemented by self-developed micro robotic mechanical testing system. Firstly, this platform not only reduced the time of alignment involved in microwire torsion test but also increased the precision of it. Secondly, the SEM imaging provided unprecedented details on their fracture state during loading and there was no obvious brittle torsion failure at the cross-section area during the experiment. The vein-pattern microstructure on the fracture cross-section area was very different from that of tensile loading. What is more, the fracture mechanism where the occurrence of the fluid area resulting from adiabatic heating leads to the fracture was revealed. Finally, because of the 6DOFs and precise movement of our platform, it may also be used for micro assembly and micromanufacturing of composite materials at microscale, such as carbon fiber yarns, or mixed protein microfibers [47].

Conflicts of Interest

The authors declare that they have no conflicts of interest.

Authors' Contributions

Chenchen Jiang and Haojian Lu contributed equally to this work.

Acknowledgments

The authors gratefully acknowledge the samples from Professor Yong Yang at the Department of Mechanical and Biomedical Engineering, City University of Hong Kong. The authors acknowledge the funding supports by Research Grants Council of the Hong Kong Special Administrative Region (CityU 11209914, CityU 11278716), the National Natural Science Foundation of China (51301147, 61403323), and Shenzhen (China) Basic Research Project (JCYJ20160329150236426).

References

- [1] N. Ranjan, M. Mertig, G. Cuniberti, and W. Pompe, "Dielectrophoretic growth of metallic nanowires and microwires: Theory and experiments," *Langmuir*, vol. 26, no. 1, pp. 552–559, 2010.
- [2] A. Zhukov, C. García, J. J. Del Val et al., "Studies of Fe-Cu microwires with nanogranular structure," *Journal of Physics Condensed Matter*, vol. 21, no. 3, Article ID 035301, 2009.
- [3] J. Hu, Y. Bando, J. Zhan, X. Yuan, T. Sekiguchi, and D. Golberg, "Self-assembly of SiO₂ nanowires and Si microwires into hierarchical heterostructures on a large scale," *Advanced Materials*, vol. 17, no. 8, pp. 971–975, 2005.
- [4] L. Jiang, Y. Fu, H. Li, and W. Hu, "Single-crystalline, size, and orientation controllable nanowires and ultralong microwires of organic semiconductor with strong photoswitching property," *Journal of the American Chemical Society*, vol. 130, no. 12, pp. 3937–3941, 2008.
- [5] R. Varga, T. Ryba, Z. Vargova, K. Saksl, V. Zhukova, and A. Zhukov, "Magnetic and structural properties of Ni-Mn-Ga Heusler-type microwires," *Scripta Materialia*, vol. 65, no. 8, pp. 703–706, 2011.
- [6] X. Lu, Y. Yu, L. Chen et al., "Poly(acrylic acid)-guided synthesis of helical polyaniline microwires," *Polymer*, vol. 46, no. 14, pp. 5329–5333, 2005.
- [7] S.-P. Tsai, D. W. Howell, Z. Huang et al., "The effect of protein fusions on the production and mechanical properties of protein-based materials," *Advanced Functional Materials*, vol. 25, no. 9, pp. 1442–1450, 2015.
- [8] E. T. Thostenson, W. Z. Li, D. Z. Wang, Z. F. Ren, and T. W. Chou, "Carbon nanotube/carbon fiber hybrid multiscale composites," *Journal of Applied Physics*, vol. 91, no. 9, pp. 6034–6037, 2002.
- [9] G. Guitchounts, J. E. Markowitz, W. A. Liberti, and T. J. Gardner, "A carbon-fiber electrode array for long-term neural recording," *Journal of Neural Engineering*, vol. 10, no. 4, Article ID 046016, 2013.
- [10] Q. Yang, W. Wang, S. Xu, and Z. L. Wang, "Enhancing light emission of ZnO microwire-based diodes by piezo-phototronic effect," *Nano Letters*, vol. 11, no. 9, pp. 4012–4017, 2011.
- [11] M. C. Putnam, S. W. Boettcher, M. D. Kelzenberg et al., "Si microwire-array solar cells," *Energy and Environmental Science*, vol. 3, no. 8, pp. 1037–1041, 2010.
- [12] J. Lee and J. Kim, "Fabrication of strongly anchored, high aspect ratio elastomeric microwires for mechanical and optical applications," *Journal of Micromechanics and Microengineering*, vol. 21, no. 8, Article ID 085016, 2011.
- [13] G. Chai, E. Rusu, L. Chow et al., "Microsensor on single ZnO microwire," in *Proceedings of the 2009 International Semiconductor Conference, CAS 2009*, pp. 275–278, October 2009.
- [14] K. S. Nakayama, Y. Yokoyama, G. Xie et al., "Metallic glass nanowire," *Nano Letters*, vol. 8, no. 2, pp. 516–519, 2008.
- [15] L. Tian, Y.-Q. Cheng, Z.-W. Shan et al., "Approaching the ideal elastic limit of metallic glasses," *Nature Communications*, vol. 3, article no. 609, 2012.
- [16] X. K. Xi, D. Q. Zhao, M. X. Pan, W. H. Wang, Y. Wu, and J. J. Lewandowski, "Fracture of brittle metallic glasses: Brittleness or plasticity," *Physical Review Letters*, vol. 94, no. 12, Article ID 125510, 2005.
- [17] A. Zhukov, M. Vázquez, J. Velázquez, A. Hernando, and V. Larin, "Magnetic properties of Fe-based glass-coated microwires," *Journal of Magnetism and Magnetic Materials*, vol. 170, no. 3, pp. 323–330, 1997.
- [18] A. Zhukov, K. Chichay, A. Talaat et al., "Manipulation of magnetic properties of glass-coated microwires by annealing," *Journal of Magnetism and Magnetic Materials*, vol. 383, pp. 232–236, 2015.
- [19] A. Zhukov, M. Ipatov, and V. Zhukova, "Advances in giant magnetoimpedance of materials," *Handbook of Magnetic Materials*, vol. 24, pp. 139–236, 2015.
- [20] V. Zhukova, M. Ipatov, and A. Zhukov, "Thin magnetically soft wires for magnetic microsensors," *Sensors*, vol. 9, no. 11, pp. 9216–9240, 2009.
- [21] P. Sharma, N. Kaushik, H. Kimura, Y. Saotome, and A. Inoue, "Nano-fabrication with metallic glass - an exotic material for nano-electromechanical systems," *Nanotechnology*, vol. 18, no. 3, Article ID 035302, 2007.
- [22] M. Zhao, K. Abe, S.-I. Yamaura, Y. Yamamoto, and N. Asao, "Fabrication of Pd-Ni-P metallic glass nanoparticles and their application as highly durable catalysts in methanol electro-oxidation," *Chemistry of Materials*, vol. 26, no. 2, pp. 1056–1061, 2014.
- [23] T. A. Phan, M. Hara, H. Oguchi, and H. Kuwano, "Current sensors using Fe-B-Nd-Nb magnetic metallic glass micro-cantilevers," *Microelectronic Engineering*, vol. 135, pp. 28–31, 2015.
- [24] A. Banerjee, C. Jiang, L. Lohiya, Y. Yang, and Y. Lu, "Fracture emission in lanthanum-based metallic glass microwires under quasi-static tensile loading," *Journal of Applied Physics*, vol. 119, no. 15, Article ID 155102, 2016.
- [25] H. Sun, Z. Ning, G. Wang et al., "Tensile strength reliability analysis of Cu₄₈Zr₄₈Al₄ amorphous microwires," *Metals*, vol. 6, no. 12, article no. 296, 2016.
- [26] H. Shen, D. Xing, H. Wang et al., "Tensile properties and fracture reliability of melt-extracted Gd-rich amorphous wires," *Materials Research*, vol. 18, pp. 66–71, 2015.
- [27] Y. Lu and J. Lou, "Quantitative in-situ nanomechanical characterization of metallic nanowires," *JOM*, vol. 63, no. 9, pp. 35–42, 2011.
- [28] P. Kumar and M. S. R. N. Kiran, "Nanomechanical characterization of indium nano/microwires," *Nanoscale Research Letters*, vol. 5, no. 7, pp. 1085–1092, 2010.
- [29] Z. Liu, X. Yan, Z. Lin, Y. Huang, H. Liu, and Y. Zhang, "Mechanical properties and indentation-induced damage of high-quality ZnO microwires," *Materials Research Bulletin*, vol. 47, no. 3, pp. 750–754, 2012.
- [30] H. Zhang, K. W. Siu, W. Liao, Q. Wang, Y. Yang, and Y. Lu, "In situ mechanical characterization of CoCrCuFeNi high-entropy alloy micro/nano-pillars for their size-dependent mechanical behavior," *Materials Research Express*, vol. 3, no. 9, Article ID 094002, 2016.

- [31] S. Maekawa, K. Takashima, M. Shimojo et al., "Fatigue tests of Ni-P amorphous alloy microcantilever beams," *Japanese Journal of Applied Physics, Part 1: Regular Papers and Short Notes and Review Papers*, vol. 38, no. 12 B, pp. 7194–7198, 1999.
- [32] M. M. McClarty, J. P. Bruce, M. S. Freund, and D. R. Oliver, "Piezoresistive characterization of bottom-up, n-type silicon microwires undergoing bend deformation," *Applied Physics Letters*, vol. 106, no. 2, Article ID 022107, 2015.
- [33] S. K. Deb Nath, H. Tohmyoh, and M. A. Salam Akanda, "Evaluation of elastic, elastic-plastic properties of thin Pt wire by mechanical bending test," *Applied Physics A: Materials Science and Processing*, vol. 103, no. 2, pp. 493–496, 2011.
- [34] G. Khatibi, A. Betzwar-Kotas, V. Gröger, and B. Weiss, "A study of the mechanical and fatigue properties of metallic microwires," *Fatigue and Fracture of Engineering Materials and Structures*, vol. 28, no. 8, pp. 723–733, 2005.
- [35] P. Li, Q. Liao, S. Yang et al., "In situ transmission electron microscopy investigation on fatigue behavior of single ZnO wires under high-cycle strain," *Nano Letters*, vol. 14, no. 2, pp. 480–485, 2014.
- [36] Y. J. Dai, Y. Huan, M. Gao et al., "Development of a high-resolution micro-torsion tester for measuring the shear modulus of metallic glass fibers," *Measurement Science and Technology*, vol. 26, no. 2, Article ID 025902, 2015.
- [37] D. Liu, Y. He, X. Tang, H. Ding, P. Hu, and P. Cao, "Size effects in the torsion of microscale copper wires: experiment and analysis," *Scripta Materialia*, vol. 66, no. 6, pp. 406–409, 2012.
- [38] C. Jiang, D. Hu, and Y. Lu, "Digital micromirror device (DMD)-based high-cycle torsional fatigue testing micromachine for 1D nanomaterials," *Micromachines*, vol. 7, no. 3, article 49, 2016.
- [39] V. Zhukova, A. F. Cobeo, A. Zhukov et al., "Correlation between magnetic and mechanical properties of devitrified glass-coated Fe_{71.8}Cu₁Nb_{3.1}Si₁₅B_{9.1} microwires," *Journal of Magnetism and Magnetic Materials*, vol. 249, no. 1-2, pp. 79–84, 2002.
- [40] A. Zhukov, M. Ipatov, A. Talaat et al., "Correlation of crystalline structure with magnetic and transport properties of glass-coated microwires," *Crystals*, vol. 7, no. 2, p. 41, 2017.
- [41] Y. Shen, Z. Zhang, and T. Fukuda, "Bending spring rate investigation of nanopipette for cell injection," *Nanotechnology*, vol. 26, no. 15, Article ID 155702, 2015.
- [42] W. Shang, H. Lu, W. Wan, T. Fukuda, and Y. Shen, "Vision-based nano robotic system for high-throughput non-embedded cell cutting," *Scientific Reports*, vol. 6, Article ID 22534, 2016.
- [43] W. Wan, H. Lu, V. Zhukova, M. Ipatov, A. Zhukov, and Y. Shen, "Surface defect detection of magnetic microwires by miniature rotatable robot inside SEM," *AIP Advances*, vol. 6, no. 9, Article ID 095309, 2016.
- [44] Y. Shen, W. Wan, H. Lu, T. Fukuda, and W. Shang, "Automatic sample alignment under microscopy for 360° imaging based on the nanorobotic manipulation system," *IEEE Transactions on Robotics*, vol. 33, no. 1, pp. 220–226, 2017.
- [45] Y. Shen, W. Wan, L. Zhang, L. Yong, H. Lu, and W. Ding, "Multidirectional image sensing for microscopy based on a rotatable robot," *Sensors (Switzerland)*, vol. 15, no. 12, pp. 31566–31580, 2015.
- [46] D. H. Sharp, "An overview of rayleigh-taylor instability," *Physica D: Nonlinear Phenomena*, vol. 12, no. 1-3, pp. 3–IN10, 1984.
- [47] Z. Huang, Y. Lu, R. Majithia et al., "Size dictates mechanical properties for protein fibers self-assembled by the drosophila hox transcription factor ultrabithorax," *Biomacromolecules*, vol. 11, no. 12, pp. 3644–3651, 2010.

Research Article

Automated Axis Alignment for a Nanomanipulator inside SEM and Its Error Optimization

Chao Zhou,¹ Lu Deng,² Long Cheng,¹ Zhiqiang Cao,¹ Shuo Wang,¹ and Min Tan¹

¹State Key Laboratory of Management and Control for Complex Systems, Institute of Automation, Chinese Academy of Sciences, Beijing, China

²School of Statistics and Mathematics, Central University of Finance and Economics, Beijing, China

Correspondence should be addressed to Lu Deng; denglu521@sina.com

Received 15 March 2017; Accepted 8 May 2017; Published 19 June 2017

Academic Editor: Yajing Shen

Copyright © 2017 Chao Zhou et al. This is an open access article distributed under the Creative Commons Attribution License, which permits unrestricted use, distribution, and reproduction in any medium, provided the original work is properly cited.

In the motion of probing nanostructures, repeating position and movement is frequently happening and tolerance for position error is stringent. The consistency between the axis of manipulators and image is very significant since the visual servo is the most important tool in the automated manipulation. This paper proposed an automated axis alignment method for a nanomanipulator inside the SEM by recognizing the position of a closed-loop controlling the end-effector, which can characterize the relationship of these two axes, and then the rotation matrix can be calculated accordingly. The error of this method and its transfer function are also calculated to compare the iteration method and average method. The method in this paper can accelerate the process of axis alignment to avoid the electron beam induced deposition effect on the end tips. Experiment demonstration shows that it can achieve a 0.1-degree precision in 90 seconds.

1. Introduction

Nanoscale manipulations inside scanning electron microscope (SEM) have found many uses in various fields [1]. Examples include nanomaterial characterizations [2–9], nanoelectronic probing [10–12], nanodevices prototyping [13], photonics [14, 15], and biological researches [16–18]. The most common setup involves installing piezo-based manipulator into an SEM. A joystick is used to control the motion of the manipulator, and the SEM provides the real-time image feedback. This combination provides an intuitive hand-eye coordinated method to interact with objectives and in micrometer and nanometer scale.

Several SEM based nanomanipulation systems have been reported in the literature [19–23]. There are also commercially available systems from Kleindiek, DCG Systems (Previously Zyvex), SmarAct, Klocke, and Attocube. The majority of these systems do not have position sensor integrated, thus repeatable motions cannot be made, and the manipulation efficiency relies heavily on the skill of the human operator. Other systems contain optical encoders for position feedback, but the heat generated by the laser diode is difficult to

dissipate inside vacuum, leading to high position drift rate. The use of mechanical sliding rails for guiding the piezo stick-slip motion is not repeatable due to frictions in the interfaces and the deformation in the mechanical rails. The stick-slip motion also creates mechanical vibration while in motion, which can cause end-effector (the device at the end of a robotic arm, such as claws and needles) or sample damage.

We have previously reported a new load-lock compatible nanomanipulation system that tackles limitations with existing nanomanipulation systems. The system utilizes unique in-vacuum, low-power electronics for sensing strain gauge deformation, and flexure based positioner design. The system is capable of producing nanometer resolution closed-loop positioning, subnanometer per minute drift, and friction free, vibration free motion inside SEM. The compact system can be mounted onto most SEM using the standard SEM sample holder, thus allowing the system to be added or removed from an SEM within seconds.

In the applications, the manipulations can be guided by SEM's real-time vision and handled by operators, or computer generating the motion targets according to the presupposed tasks. Since all the position information is

calculated based on the images, this requires the consistency between the image's and manipulator's axis. However, there are always install errors, and the two set axes cannot be aligned perfectly. The end-effectors will not match the expected position on images with these errors, and subtle differences will cause large deviation in the nanoscale motion.

There are three key sources of error that demand a full system recalibration prior to use every time. (1) While handling the system, the force exerted by the human hand causes tiny changes to the mechanical assembly of the system. These changes lead to performance variation of the system in the micronanometer scale. (2) When the system is installed onto the SEM, there exists small misalignment between the SEM and nanomanipulation system. Even when the installation is carefully conducted, it is impossible to align the system onto SEM stage with nanometer precision. (3) The internal temperature of the SEM can vary by a few degrees after each setup, which affects the positioner sensor accuracy. All of these factors contribute to inaccuracy in position sensor, which demands recalibration prior to operation each time.

Manually performing the calibrations is time consuming and poor in repeatability. The extended electron beam exposure to the end-effector and sample also leads to significant amount of electron beam induced deposition (EBID) [24]. The rotation of SEM's image can only align one of the image's and manipulator's axes, X or Y . This rotation cannot deal with the situation that the manipulator's axes are not vertical. So an automated calibration process is necessary for quickly measuring the angle and calculating the rotation matrix to align the axes of nanomanipulation robot inside SEM.

This paper developed an automated approach for calibration. The performance of the calibration method is evaluated in terms of speed, calibration repeatability, and positioning accuracy. Compared with our conference paper [25], this paper provides additional details on the error optimization and Z -axis misalignment compensation; furthermore, more experimental data are presented. The nanomanipulation system is briefly introduced in Section 2. Section 3 presents the automated alignment method based on the SEM image processing. Section 4 analyzed the system's error transfer and optimization. Finally, Section 5 concludes the paper.

2. System Overview

The nanomanipulation system used for this study consists of four manipulators mounted on a vacuum load-lock compatible carrier [26]. Each manipulator consists of three long range coarse positioners with three high precision fine positioners stacked on top. Coarse positioners are composed of three stick-slip based piezo positioners for XYZ positioning. No sensory feedback is implemented in the coarse positioners to minimize heat generation sources. The fine positioners are three flexure guided, preloaded piezo positioners with one strain gauge mounted on each piezo stack. The position sensing principle involves the use of strain gauges mounted on piezo and utilizes time-to-digital convertor (TDC) for strain sensing.

On-board electronics are placed within the aluminum housing of the nanomanipulation system carrier inside the

SEM. The external electronics consist of an MCU and arrays of operational amplifiers for driving the piezo stack. After receiving sensor readout from the on-board electronics, the MCU computes the required piezo stack driving voltages based on the PID control law and sends driving voltages to the on-board electronics.

The nanomanipulation system is mounted on a standard SEM sample holder, allowing the system to be added or removed from the SEM stage within seconds.

When manipulating sample inside SEM, the nanomanipulation system is transferred inside SEM through the vacuum load-lock. Then, the sample is transferred inside, too. The axis needs to be aligned to insure the position accuracy. The region of interest can be located manually, and a series of preset operation will be carried out.

Manual calibrations of each fine positioner were conducted under SEM imaging. It involves moving each of the fine positioners back and forth to determine its motion path, followed by raster rotating the SEM image to adjust positioner-image misalignment. The process is completed through manual trial and error. It takes approximately 2 minutes to determine the misalignment angle for one single fine positioner axis. For a 4-manipulator system with 12 axes, the total calibration takes ~ 24 minutes. After collecting all the misalignment angles between the fine positioners and SEM images, a rotation matrix is used. This calibration process needs to be repeated if the system is removed/added back into the SEM or made physical contact with a human hand. Since the operations are manually performed, the repeatability and accuracy are not stable.

3. Methods

An automated alignment method is proposed in this paper to calculate the rotation matrix. The system moved the end-effector automated and recognized the end-effector's position based on template matching method. The basic idea is the rotation matrix T to transform the expected motion in image coordinate to the motion of every axis:

$$\begin{bmatrix} x \\ y \\ z \end{bmatrix}_{\text{axis}} = T \begin{bmatrix} x \\ y \\ z \end{bmatrix}_{\text{img}}, \quad (1)$$

where $[x \ y \ z]_{\text{axis}}'$ are the axes' extension of the manipulator and $[x \ y \ z]_{\text{img}}'$ is the end-effector's expected motion on the image. Since the Z -axis' motion cannot be observed because the SEM's feedback is 2D image, only X - and Y -axes can be calibrated.

3.1. The Filter and Recognition of Image. High SEM image frame rate is desirable for real-time nanomanipulation, but it leads to degraded image quality. A low accelerating voltage is used to minimize electron induced damage on the sample, but the image signal-to-noise ratio is poor. A filter method is necessary to reduce the image noise real-time.

GPU accelerated nonlocal means (NL-means) method [10, 27] was shown to be effective in reducing SEM image

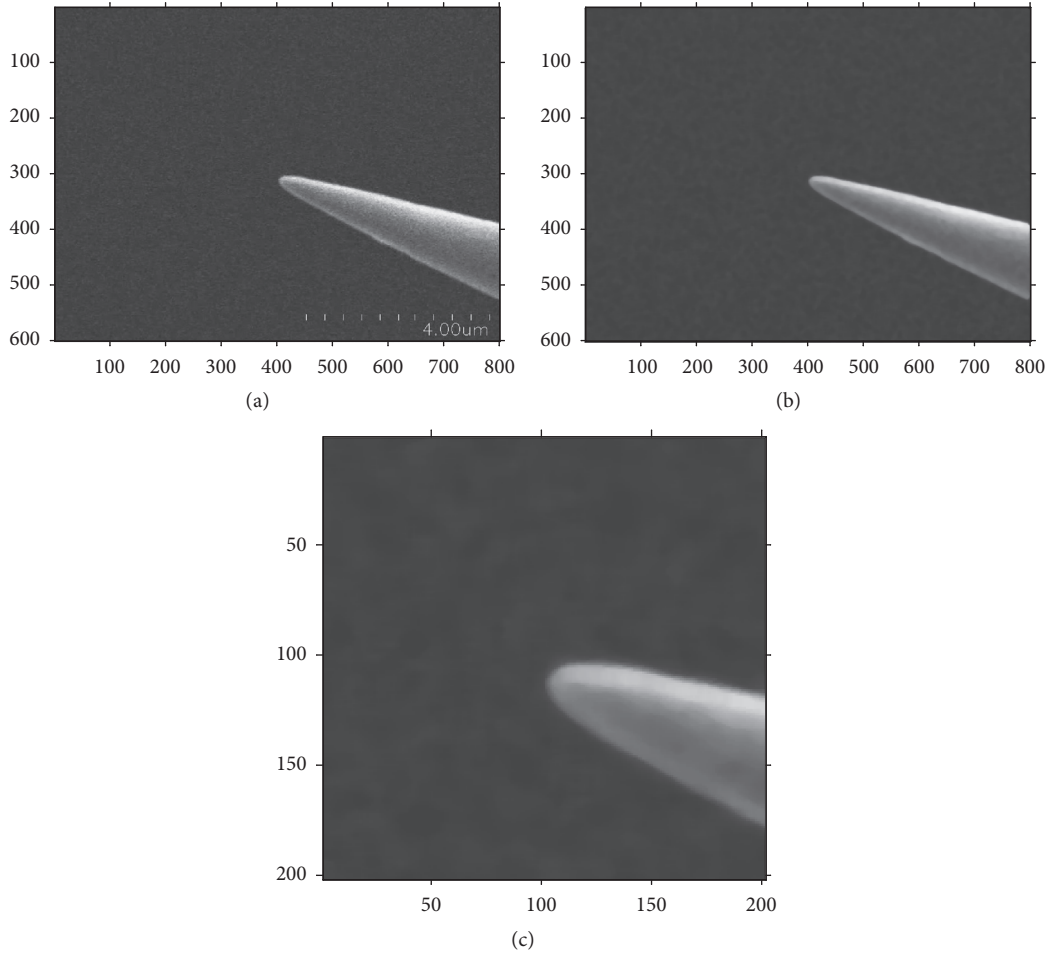


FIGURE 1: The SEM image of (a) end-effector (tungsten probes), (b) its denoising result, and (c) manually selected template.

noise in real-time. It is based on globally averaging all the pixels in an image and produces images with lower noise and with more details retained. The algorithm when implemented on graphics processing unit (GPUs) can satisfy the real-time SEM image denoising/processing. Figure 1 is one of the image frames, its denoising result and manually selected template.

After denoising the image, the position of the end-effector can be accurately recognized. In the calibration stage, the background of SEM's image can be adjusted to almost black, so its difference to the foreground is apparent. Template matching method is adopted to recognize the position of the end-effector [28]. Considering the noise level of the SEM image, the template matching based on FFT is adopted, which have good performance in rapidity and robustness. As to template $T = T(M_T, N_T)$, the matching function in image $I = I(M_I, N_I)$ is

$$\text{cov} = \text{FFT}^{-1} \left(\text{FFT}(\bar{T}) \cdot \text{FFT}(I') \right), \quad (2)$$

where $\bar{T} = \text{rot}(T)$ is the rotation and expansion of T . I' is the transposition of I . The point with maxim cov is the registration point. Figure 2 is the recognition results of stable target (Figure 2(a)) and moving target (Figure 2(b)).

3.2. The Rotation Matrix. The key to calculate the rotation matrix is to obtain the angles between the manipulator's motion axes and image's axes. The end-effector was controlled to move a series of positions, followed by image registration and record the position. These serial position coordinates can be fitted and the angles then were obtained. Firstly, define the coordinate system as Figure 3.

As shown in Figure 3, X_{Img} , Y_{Img} , and Z_{Img} are the axes of image. X_{axis} , Y_{axis} , Z_{axis} , and O are the terminate frame of manipulator. X'_{axis} , Y'_{axis} , and Z'_{axis} are the terminate frame's projection on $X_{\text{Img}}-Y_{\text{Img}}$ plane. α , β , θ , and ψ are the angle between X'_{axis} and X_{Img} , Y'_{axis} and Y_{Img} , Z'_{axis} and Z_{Img} , respectively.

Specific algorithm is as follows:

- (1) Adjust magnification of SEM to 13,000x. Adjust the SEM imaging parameters to maximize the focus and contrast of the SEM image. Manually select template.
- (2) Control the end-effect to certain position and wait until the error is less than 5 nm.
- (3) Filter the image and reorganize the end-effector's position (x_i^X, y_i^X) .
- (4) Repeat steps (2) and (3), with a serial equidistant position, and record the positions as $X_A = [x_i^X]', Y_A^X = [y_i^X]', i = 1, 2, \dots, n$.

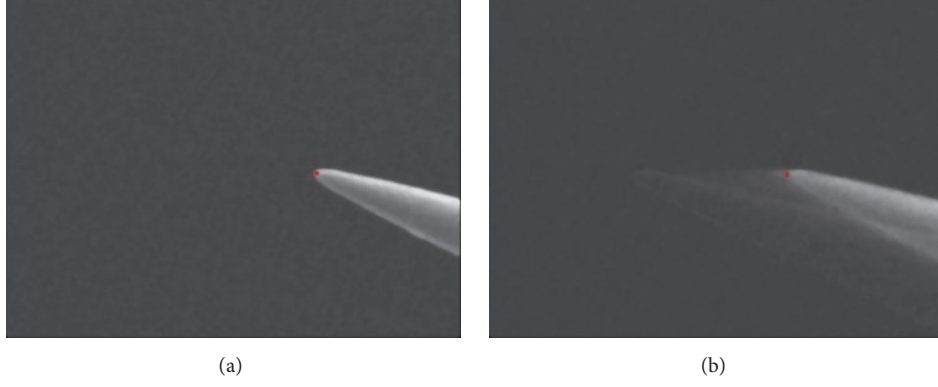


FIGURE 2: The recognition results. (a) Stable target and (b) moving target.

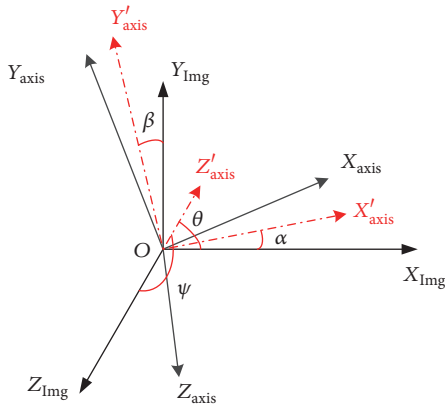


FIGURE 3: The coordinate system and the angle definition.

(5) Consider (x_i^X, y_i^X) is in a straight line to two-dimensional data where both variables are measured with error. Fit the line by Deming Regression and line is $l_x : y^Y = a_x x^X + b_x$, where

$$a_x = \frac{s_{yy} - \delta s_{xx} + \sqrt{(s_{yy} - \delta s_{xx})^2 + 4\delta s_{xy}^2}}{2s_{xy}}$$

$$b_x = \bar{y} - a_x \bar{x},$$

$$\bar{x} = \sum x_i^X,$$

$$\bar{y} = \sum y_i^X.$$

$$s_{xx} = \frac{1}{n-1} \sum (x_i^X - \bar{x})^2$$

$$s_{xy} = \frac{1}{n-1} \sum (x_i^X - \bar{x})(y_i^X - \bar{y})$$

$$s_{yy} = \frac{1}{n-1} \sum (y_i^X - \bar{y})^2$$

(6) Move it along y -axis, and recognize the position (x_j^Y, y_j^Y) automatically, $j = 1, 2, \dots, m$. Fit them and get the line l_y with slope a_y .

(7) Then $tg\alpha = a_x, tg\beta = a_y$, and according to the rotation matrix (1), T can be calculated as

$$T = A^{-1} = \begin{bmatrix} \cos \alpha & -\sin \beta & 0 \\ \sin \alpha & \cos \beta & 0 \\ 0 & 0 & 1 \end{bmatrix}^{-1}. \quad (4)$$

So we have

$$T = A^{-1} = \begin{bmatrix} \frac{\pm 1}{\sqrt{a_x^2 + 1}} & -\frac{\pm 1}{\sqrt{a_y^2 + 1}} & 0 \\ \frac{\pm 1}{\sqrt{a_x^2 + 1}} & \frac{\pm 1}{\sqrt{a_y^2 + 1}} & 0 \\ 0 & 0 & 1 \end{bmatrix}^{-1}. \quad (5)$$

In the visual servo, if the position expected on image is $P_{img} = [x \ y \ z]_{img}'$, the target of the manipulator's axis motion is $P_{axis} = [x \ y \ z]_{axis}' = T [x \ y \ z]_{img}'$.

3.3. Z-Axis Misalignment Compensation. As to the manipulator's Z-axis, the target image is 2D image according to the SEM's image-forming principle and cannot reflect the depth information. Many depth predicting methods are developed [12, 29] to gather useful information on Z-direction. In the application, the movement on Z-axis often causes the extra movement on the X- and Y-axes due to the install error, which is harmful in operation because it may cause the sample damage while Z is moved to sample surface. So it needs to be compensated. The new rotation matrix is

$$T_1 = A_1^{-1} = \begin{bmatrix} \cos \alpha & -\sin \beta & \cos \theta * \cos \psi \\ \sin \alpha & \cos \beta & \sin \theta \cos \psi \\ 0 & 0 & 1 \end{bmatrix}^{-1}, \quad (6)$$

where $tg\alpha = a_x$ and $tg\beta = a_y$.

However, θ and ψ are both immeasurable, so we firstly moved Z-axis with a large distance D_z and record the movement on image as D_x and D_y ; then we have $\cos \theta *$

$\cos \psi = D_x/D_z$, $\sin \theta \cos \psi = D_y/D_z$, so the rotation matrix T_1 is

$$T_1 = A_1^{-1} = \begin{bmatrix} \frac{\pm 1}{\sqrt{a_x^2 + 1}} & -\frac{\pm 1}{\sqrt{a_y^2 + 1}} & \frac{D_x}{D_z} \\ \pm 1 & \pm 1 & \frac{D_y}{D_z} \\ \frac{\pm 1}{\sqrt{a_x^2 + 1}} & \frac{\pm 1}{\sqrt{a_y^2 + 1}} & \frac{D_z}{D_z} \\ 0 & 0 & 1 \end{bmatrix}^{-1}. \quad (7)$$

In some other occasions, such that the end-effector is far from the sample, the motion of Z-axis can be embodied in some way to help indicating its motion. When Z is moving, we can move X and Y a little, so the end-effector seems like moving forward. This mode covers the shortage that Z cannot be observed directly in SEM's image. To realize this, we can change the position after alignment:

$$\begin{aligned} P_{\text{axis}} &= \begin{bmatrix} x \\ y \\ z \end{bmatrix}_{\text{axis}} = T_1 \begin{bmatrix} x + \Delta z \\ y + \Delta z \\ z \end{bmatrix}_{\text{img}} \\ &= T_1 \begin{bmatrix} 1 & 0 & k \\ & 1 & k \\ & & 1 \end{bmatrix} \begin{bmatrix} x \\ y \\ z \end{bmatrix}_{\text{img}} \triangleq T_k \begin{bmatrix} x \\ y \\ z \end{bmatrix}_{\text{img}}, \end{aligned} \quad (8)$$

where $k = \Delta z/z$ and T_k is the new rotation matrix.

k is very small normally, and the small displacement in X- and Y-direction can indicate the movement of Z-axis, which allow the operator to clearly sense it and improve the control accuracy. Switching T_k and T_1 in different occasion can make the operation conveniently.

4. Error Analysis

For nanoscale motion, small error on positioner axis may cause large difference in the end. Since tolerance for position error is stringent during the data collection process, the method for reducing the error in axis alignment needs to be researched. The alignment method in this paper is to utilize the target registration and slope calculation. The random error mainly comes from the anamorphose, image noise, recognition error, fitting error, and shape variation of end-effector (due to EBID). For the purpose of reducing positioning error, several means can be adopted, such as unbiased filter and recognition algorithm, the independent variable choice in fitting to improve the precision of the slope.

Besides, multiple alignments can also reduce the error. The SEM's image is different to the physical object and the resulting error can be reduced by iterative method. Realign the axes after the rotation matrix is used in the manipulator system, and multiply the two rotation matrixes; we can get a new matrix. Repeat this process until the error is lower than a certain threshold. On the other hand, the image noise, the error on recognition, and fitting can be reduced by making this same measurement multiple times and taking the average. These two methods both can improve the precision.

However, the process of alignment has to be as quick as it can to reduce the EBID's effects on end-effector. If one time alignment cannot satisfy the required precision, the alignment method needs to be further optimized. So the error's propagation in this algorithm is researched to compare iteration method and average method under the condition of limited times. The confidence interval of position is adopted to indicate the error.

4.1. The Confidence Interval of Position. Denote the error of the end-effector P_{axis} as $\varepsilon_{P_{\text{axis}}}$, where $P_{\text{axis}} = [x \ y \ z]_{\text{axis}}' = T [x \ y \ z]_{\text{img}}'$. The error comes from the rotation matrix T , which is obtained by a series of transformation. Without loss of generality, we can analyze the error's propagation of the unit displacement of all axes ($P_{\text{img}} = [1 \ 1 \ 1]'$). The main error sources of T are the two parameters a_x and a_y . D_x and D_y 's contribution on final result are too small. Denote the error of a_x and a_y as ε_{ax} and ε_{ay} ; then we have

$$\varepsilon_{P_{\text{axis}}} = \frac{\partial P_{\text{axis}}}{\partial a_x} \varepsilon_{ax} + \frac{\partial P_{\text{axis}}}{\partial a_y} \varepsilon_{ay} \quad (9)$$

Considering the experiments of X- and Y-axes are independent, their errors are independent, too. So the variance $V_{P_{\text{axis}}}$ is

$$\begin{aligned} V_{P_{\text{axis}}} &= \left(\frac{\partial P_{\text{axis}}}{\partial a_x} \right)^T \left(\frac{\partial P_{\text{axis}}}{\partial a_x} \right) V_{ax} \\ &+ \left(\frac{\partial P_{\text{axis}}}{\partial a_y} \right)^T \left(\frac{\partial P_{\text{axis}}}{\partial a_y} \right) V_{ay}, \end{aligned} \quad (10)$$

where V_{ax} and V_{ay} are the variance of a_x and a_y , and they can be calculated by jackknife estimate, which is a resampling technique especially useful for variance and bias estimation. The basic idea is to estimate the parameter for each subsample omitting the i th observation to estimate the previously unknown value of \bar{a}_x^i by average. The variance of a_x is

$$V_{ax} = \frac{\sum_{i=1}^N (\bar{a}_x^i - \bar{a}_x)^2}{(N-1)}, \quad (11)$$

where $\bar{a}_x = (1/N) \sum_{j=1}^N \bar{a}_x^j$ and N is sample size.

Since X and Y are symmetric, we calculate X-axis firstly. According to the Deming Regression, the parameter a_x 's confidence interval is $a_x \pm t_{1-v/2, N-1} \text{SE}_{ax}$, where v is confidence level, and SE_{ax} is standard error of a_x . The variance of a_y can be got in the same way. So, the confidence interval of P_{axis} is

$$\begin{aligned} \hat{P}_{\text{axis}} &= P_{\text{axis}} \pm \frac{t_{1-v/2, N-1}}{\sqrt{N}} \left(\left(\frac{\partial P_{\text{axis}}}{\partial a_x} \right)^T \left(\frac{\partial P_{\text{axis}}}{\partial a_x} \right) V_{ax} \right. \\ &\left. + \left(\frac{\partial P_{\text{axis}}}{\partial a_y} \right)^T \left(\frac{\partial P_{\text{axis}}}{\partial a_y} \right) V_{ay} \right)^{1/2}. \end{aligned} \quad (12)$$

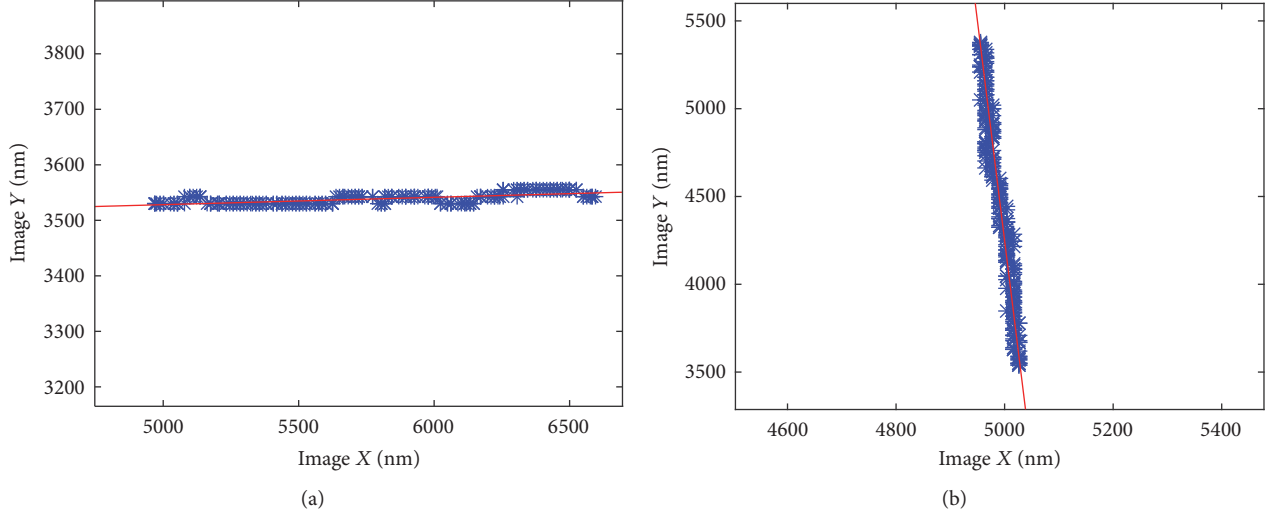


FIGURE 4: The results of recognition and fitting of X- and Y-axis, where blue dots are the data extracted from SEM images, and red line is the linearly fitted line.

4.2. The Error Optimizing. Equation (12) is too complicated for analysis, so it should be simplified. In the application, the angle between axes of image and manipulator is very small, that is, $\alpha, \beta \rightarrow 0$, and using second-order Taylor expansion, we can get $\cos \alpha \rightarrow 1 - \alpha^2/2$ and $\sin \alpha \rightarrow \alpha$. After dropping higher-order infinitesimal, we have

$$\begin{aligned} \hat{P}_{\text{axis}} &\approx P_{\text{axis}} \\ &\pm \frac{t_{1-\nu/2, N-1}}{\sqrt{N}} \left(\frac{1 + 2a_y + a_y^2 + 2a_x^2 - 2a_x a_y}{1 - 2a_x^2 - 2a_y^2 + 4a_x a_y} V_{ax} \right. \\ &\quad \left. + \frac{1 - 2a_x + 2a_y^2 + a_x^2 - 2a_x a_y}{1 - 2a_x^2 - 2a_y^2 + 4a_x a_y} V_{ay} \right)^{1/2}. \end{aligned} \quad (13)$$

It can be summarized that the confidence interval of end-effector's position P_{axis} is determined by V_{ax} and V_{ay} . When a_x and a_y are small enough, $\hat{P}_{\text{axis}} \approx P_{\text{axis}} \pm t_{1-\nu/2, N-1} (V_{ax} + V_{ay})^{1/2} / \sqrt{N}$. So obviously, decreasing V_{ax} and V_{ay} improves the precision of P_{axis} . As to the method in this paper, multiple times alignment and taking the average of a_x and a_y is the optimized choice. When a_x and a_y are not small enough, such that the manipulator was installed incorrectly or it needs to be rotated, the coefficients of V_{ax} and V_{ay} in propagation are greater than 1 significantly, and the system needs to be iterated for a few times until a_x and a_y are small enough and then optimize it with average method.

5. The Experiments

To minimize the thermally induced drift of our system within the vacuum environment, the nanomanipulation system was installed into the SEM for 3 hours prior to the experiment to ensure that the system had reached thermal equilibrium within the SEM. A magnification of 13,000x is selected, which has a field of view (FOV) of $9.7 \mu\text{m} \times 7.3 \mu\text{m}$, and

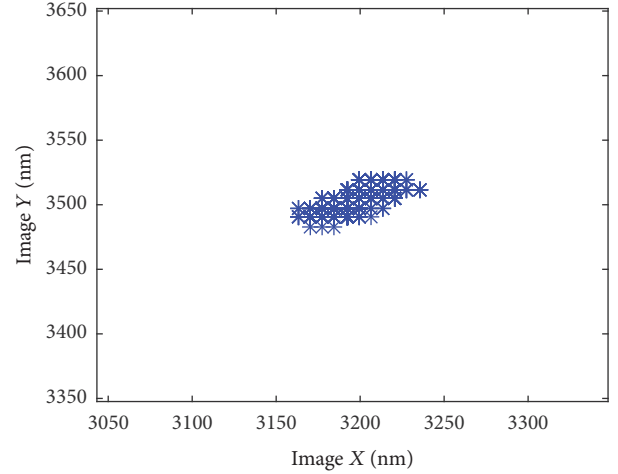


FIGURE 5: The movement on X- and Y-direction when Z is moved on range of 3 um.

each pixel is 12.2 nm in size. Selecting a high image magnification can improve image resolution, but only a smaller nanopositioner motion can be observed within the FOV. The method described in Section 3 is implemented to align the XYZ-axis, and the result of X- and Y-axis is shown in Figure 4.

In this experiment, the X-axis of manipulator has relatively large difference to the image, and the Y-axis is smaller. The slopes of these two lines are $a_x = -0.0400$ and $a_y = -0.0132$, which mean $\alpha = -4.58^\circ$ and $\beta = -1.51^\circ$.

As to Z-axis, only its effect on X- and Y-axis can be observed, and we adjust the X- and Y-axis's motion according to (7). Z-axis is moved in larger range, and the displacement on X- and Y-direction is recoded to calculate T_1 to compensate X- and Y-axis's motion. The result is shown in Figure 5. The Z-axis's motion range is 3 um, and the effect on X- and Y-axis is -42.51 nm and -21.25 nm .

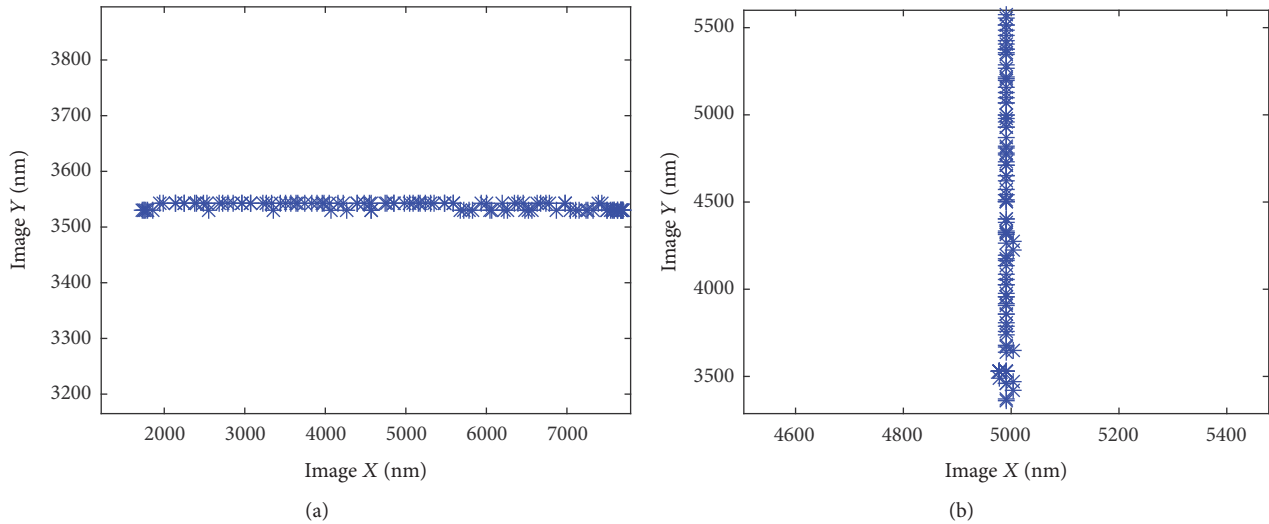


FIGURE 6: The motion trail of X- and Y-axis when it is controlled alone.

And the rotation matrix is

$$T_1 = \begin{bmatrix} 1.0006 & 0.0401 & 0.0145 \\ 0.0133 & 1.0013 & 0.0073 \\ 0 & 0 & 1 \end{bmatrix}. \quad (14)$$

After this alignment, the movement of X- and Y-axis is shown in Figure 6.

Please refer to the Supplementary Video for the details (see Supplementary Material available online at <https://doi.org/10.1155/2017/3982503>). The motion of manipulator fits the image's axis very well after the automated alignment. The whole process takes 90 seconds, and the slope was $a_x = -0.0012$ and $a_y = -0.0013$, meaning that the error of angle is less than 0.1° .

6. Conclusion

This paper discussed the automated axis alignment method for a manipulator system inside SEM. An end-effector recognition and Deming Regression were adopted to calculate the angle deviation and multiple rotation matrixes are proposed to correct the motion in different condition. The error propagation of this method is analyzed. The average method and iteration method are compared to find out a faster method when more than one time alignment is necessary. The method can speed up the process of alignment and avoid the damage on end-effect due to EBID.

Conflicts of Interest

The authors declare that they have no conflicts of interest.

Acknowledgments

This work was supported in part by the National Natural Science Foundation of China (61528304, 71401189, and 61473295) and by Beijing Natural Science Foundation (4152054).

References

- [1] C. Shi, K. D. Luu, Q. Yang et al., "Recent advances in nanorobotic manipulation inside scanning electron microscopes," *Microsystems & Nanoengineering*, vol. 2, 16024, 2016.
- [2] L. Dong, K. Shou, D. R. Frutiger et al., "Engineering multiwalled carbon nanotubes inside a transmission electron microscope using nanorobotic manipulation," *IEEE Transactions on Nanotechnology*, vol. 7, no. 4, pp. 508–517, 2008.
- [3] T. Fukuda, F. Arai, and L. Dong, "Assembly of nanodevices with carbon nanotubes through nanorobotic manipulations," *Proceedings of the IEEE*, vol. 91, no. 11, pp. 1803–1818, 2003.
- [4] D. J. Bell, L. Dong, B. J. Nelson, M. Golling, L. Zhang, and D. Grützmacher, "Fabrication and characterization of three-dimensional InGaAs/GaAs nanosprings," *Nano Letters*, vol. 6, no. 4, pp. 725–729, 2006.
- [5] Y. Zhu, F. Xu, G. Qin, W. Y. Fung, and W. Lu, "Mechanical properties of vapor-Liquid-Solid synthesized silicon nanowires," *Nano Letters*, vol. 9, no. 11, pp. 3934–3939, 2009.
- [6] H. D. Espinosa, Y. Zhu, and N. Moldovan, "Design and operation of a MEMS-based material testing system for nanomechanical characterization," *Journal of Microelectromechanical Systems*, vol. 16, no. 5, pp. 1219–1231, 2007.
- [7] G. Hwang, H. Hashimoto, D. J. Bell, L. Dong, B. J. Nelson, and S. Schön, "Piezoresistive InGaAs/GaAs nanosprings with metal connectors," *Nano Letters*, vol. 9, no. 2, pp. 554–561, 2009.
- [8] A. Lugstein, M. Steinmair, A. Steiger, H. Kosina, and E. Bertagnolli, "Anomalous piezoresistance effect in ultrastrained silicon nanowires," *Nano Letters*, vol. 10, no. 8, pp. 3204–3208, 2010.
- [9] Y. Shen, M. Nakajima, Z. Zhang, and T. Fukuda, "Dynamic force characterization microscopy based on integrated nanorobotic AFM and SEM system for detachment process study," *IEEE/ASME Transactions on Mechatronics*, vol. 20, no. 6, pp. 3009–3017, 2015.
- [10] Z. Gong, B. K. Chen, J. Liu, and Y. Sun, "Robotic probing of nanostructures inside scanning electron microscopy," *IEEE Transactions on Robotics*, vol. 30, no. 3, pp. 758–765, 2014.

- [11] C. Ru, Y. Zhang, Y. Sun et al., "Automated four-point probe measurement of individual nanowires inside a scanning electron microscope," in *Proceedings of the 2010 IEEE International Conference on Automation Science and Engineering (CASE '10)*, vol. 10, pp. 674–681, IEEE, Toronto, Canada, August 2010.
- [12] J. Li, Y. Zhang, S. To, L. You, and Y. Sun, "Effect of nanowire number, diameter, and doping density on nano-FET biosensor sensitivity," *ACS Nano*, vol. 5, no. 8, pp. 6661–6668, 2011.
- [13] K. Aoki, H. T. Miyazaki, H. Hirayama et al., "Microassembly of semiconductor three-dimensional photonic crystals," *Nature Materials*, vol. 2, no. 2, pp. 117–121, 2003.
- [14] H.-Y. Chen, C.-L. He, C.-Y. Wang et al., "Far-field optical imaging of a linear array of coupled gold nanocubes: direct visualization of dark plasmon propagating modes," *ACS Nano*, vol. 5, no. 10, pp. 8223–8229, 2011.
- [15] M. R. Ahmad, M. Nakajima, M. Kojima, S. Kojima, M. Homma, and T. Fukuda, "Nanofork for single cells adhesion measurement via ESEM-nanomanipulator system," *IEEE Transactions on Nanobioscience*, vol. 11, no. 1, pp. 70–78, 2012.
- [16] Z. Gong, B. K. Chen, J. Liu et al., "Fluorescence and SEM correlative microscopy for nanomanipulation of sub-cellular structures," *Light: Science & Applications*, vol. 3, no. e224, 2014.
- [17] B. K. Chen, D. Anchel, Z. Gong et al., "Nano-dissection and sequencing of DNA at single sub-nuclear structures," *Small*, vol. 10, no. 16, pp. 3267–3274, 2014.
- [18] Y. Shen, M. Nakajima, Z. Yang et al., "Single cell stiffness measurement at various humidity conditions by nanomanipulation of a nano-needle," *Nanotechnology*, vol. 24, no. 14, 145703, 2013.
- [19] M.-F. Yu, O. Lourie, M. J. Dyer, K. Moloni, T. F. Kelly, and R. S. Ruoff, "Strength and breaking mechanism of multiwalled carbon nanotubes under tensile load," *Science*, vol. 287, no. 5453, pp. 637–640, 2000.
- [20] L. Dong, F. Arai, and T. Fukuda, "Destructive constructions of nanostructures with carbon nanotubes through nanorobotic manipulation," *IEEE/ASME Transactions on Mechatronics*, vol. 9, no. 2, pp. 350–357, 2004.
- [21] E. C. Heeres, A. J. Katan, M. H. Van Es et al., "A compact multipurpose nanomanipulator for use inside a scanning electron microscope," *Review of Scientific Instruments*, vol. 81, no. 2, 023704, 2010.
- [22] S. Fatikow, T. Wich, H. Hülsen, T. Sievers, and M. Jähnisch, "Microrobot system for automatic nanohandling inside a scanning electron microscope," *IEEE/ASME Transactions on Mechatronics*, vol. 12, no. 3, pp. 244–252, 2007.
- [23] D. Zhang, J.-M. Breguet, R. Clavel, V. Sivakov, S. Christiansen, and J. Michler, "In situ electron microscopy mechanical testing of silicon nanowires using electrostatically actuated tensile stages," *Journal of Microelectromechanical Systems*, vol. 19, no. 3, pp. 663–674, 2010.
- [24] L. Ven Kouwen, A. Botman, and C. W. Hagen, "Focused electron-beam-induced deposition of 3 nm dots in a scanning electron microscope," *Nano Letters*, vol. 9, no. 5, pp. 2149–2152, 2009.
- [25] C. Zhou, Z. Wu, L. Deng, Y. Wang, Z. Cao, and M. Tan, "Automated axis alignment for a nano manipulator inside SEM," in *Proceedings of the 2016 IEEE International Conference on Robotics and Biomimetics (ROBIO '16)*, pp. 1293–1297, IEEE, Qingdao, China, December 2016.
- [26] C. Zhou, Z. Gong, B. K. Chen et al., "A closed-loop controlled nanomanipulation system for probing nanostructures inside scanning electron microscopes," *IEEE/ASME Transactions on Mechatronics*, vol. 21, no. 3, pp. 1233–1241, 2016.
- [27] A. Buades, B. Coll, and J.-M. Morel, "A non-local algorithm for image denoising," in *Proceedings of the 2005 IEEE Computer Society Conference on Computer Vision and Pattern Recognition, CVPR 2005*, pp. 60–65, USA, June 2005.
- [28] V. Eichhorn, S. Fatikow, T. Wortmann et al., "NanoLab: a nanorobotic system for automated pick-and-place handling and characterization of CNTs," in *Proceedings of the 2009 IEEE International Conference on Robotics and Automation, ICRA '09*, pp. 1826–1831, JPN, May 2009.
- [29] V. Eichhorn, S. Fatikow, T. Wich et al., "Depth-detection methods for microgripper based CNT manipulation in a scanning electron microscope," *Journal of Micro-Nano Mechatronics*, vol. 4, no. 1-2, pp. 27–36, 2008.

Research Article

Application of Environmental Scanning Electron Microscope-Nanomanipulation System on Spheroplast Yeast Cells Surface Observation

Maryam Alsadat Rad,¹ Mohd Ridzuan Ahmad,¹ Masahiro Nakajima,² Seiji Kojima,³ Michio Homma,³ and Toshio Fukuda²

¹Department of Control and Mechatronic Engineering, Faculty of Electrical Engineering, Universiti Teknologi Malaysia, 81310 Skudai, Johor, Malaysia

²Department of Micro-Nano Systems Engineering, Nagoya University, Nagoya, Japan

³Division of Biological Science, Graduate School of Science, Nagoya University, Nagoya, Japan

Correspondence should be addressed to Mohd Ridzuan Ahmad; ridzuan@fke.utm.my

Received 17 February 2017; Accepted 29 March 2017; Published 27 April 2017

Academic Editor: Renato Buzio

Copyright © 2017 Maryam Alsadat Rad et al. This is an open access article distributed under the Creative Commons Attribution License, which permits unrestricted use, distribution, and reproduction in any medium, provided the original work is properly cited.

The preparation and observations of spheroplast W303 cells are described with Environmental Scanning Electron Microscope (ESEM). The spheroplasting conversion was successfully confirmed qualitatively, by the evaluation of the morphological change between the normal W303 cells and the spheroplast W303 cells, and quantitatively, by determining the spheroplast conversion percentage based on the OD₈₀₀ absorbance data. From the optical microscope observations as expected, the normal cells had an oval shape whereas spheroplast cells resemble a spherical shape. This was also confirmed under four different mediums, that is, yeast peptone-dextrose (YPD), sterile water, sorbitol-EDTA-sodium citrate buffer (SCE), and sorbitol-Tris-HCl-CaCl₂ (CaS). It was also observed that the SCE and CaS mediums had a higher number of spheroplast cells as compared to the YPD and sterile water mediums. The OD₈₀₀ absorbance data also showed that the whole W303 cells were fully converted to the spheroplast cells after about 15 minutes. The observations of the normal and the spheroplast W303 cells were then performed under an environmental scanning electron microscope (ESEM). The normal cells showed a smooth cell surface whereas the spheroplast cells had a bleb-like surface after the loss of its integrity when removing the cell wall.

1. Introduction

Over the years, traditional scanning electron microscope (SEM) made a lot of contributions in the imaging of materials with a detailed description of their structure and surfaces [1–4]. However, the need for high vacuum operating environment and complex sample preparation steps made the application on biological samples and specimen unfavorable [5–7]. Environmental Scanning Electron Microscope (ESEM) has overcome many of the drawbacks found in SEM and introduced a new advantage in biological research [8–11]. The ability of this tool to operate in wet and gaseous atmospheres made the nonconductive samples conductive, thus overcoming the need for coating samples prior to characterization and

preserving samples original features for further testing and manipulation [12–14]. In addition, the capability to control water vapor pressure inside the microscope while operating keeps the samples hydrated, which increases the chances of survival [15, 16].

One of the earliest experiments on biological specimens was done by Collins et al. [17]. They explained the application and advantages of using ESEM on microorganisms. ESEM has found its potentials in tissue engineering and biomaterials studies, because it supports the observation of cell and their topography in hydrated atmospheres [18]. Furthermore, the reduced sample preparation steps are useful for investigating mammalian cells and biomaterial interactions [5, 19–23]. Kirk et al. have imaged mammalian cells using ESEM showing very

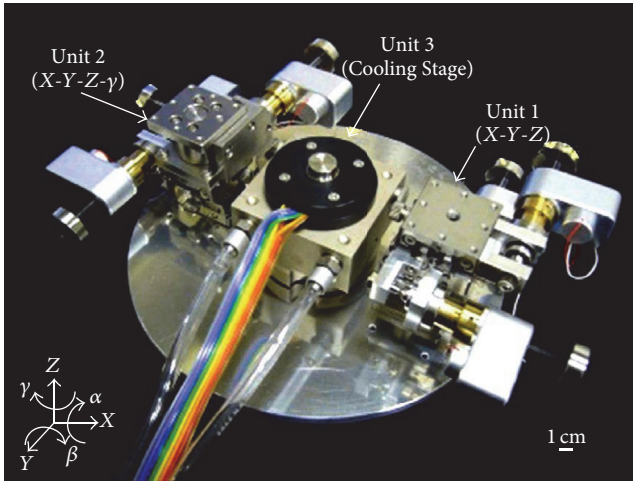


FIGURE 1: Nanorobotic manipulator of ESEM.

fine detail of delicate features such as filopodia and membrane ruffles [24]. They also showed that the cells survived the initial stages of sample preparation but experienced some damage during the dehydration stage. They have suggested cells with stronger cell wall could be imaged in their living states.

One of the main criteria of ESEM is the real life observation and monitoring of biological cells. This could be an advantage by integrating tools such as nanomanipulators or patch clamp to analyze cells and their characteristics while performing experiments. From our previous work, a nanomanipulator was successfully incorporated inside ESEM (Figure 1) for various single cell manipulation and characterization [25, 26].

One potential application of ESEM is to study the ion channel current measurement of cells by combining it with a patch-clamp system. The conventional planar patch-clamp system requires a bath solution to perform the measurement. However, this could result in having come errors in the measurement because of the differences between the bath solution chemical properties and the cytoplasm inside the cell [27]. To overcome that, instead of using the bath solution, the electrodes could be injected into the cell and the cytoplasm could be used as the medium for the current to flow during the current recording. Spheroplasting is one of the early steps required in the ion channel measurements experiments [28]. Thus, in order to perform the patch-clamp experiment inside ESEM, it is important to confirm the ability of ESEM to observe spheroplast cells successfully before further manipulation could be carried out.

Nanomanipulation is an effective strategy for the characterization of basic properties of individual nanoscale objects and to construct nanoscale devices quickly and effectively. We have constructed a hybrid nanorobotic manipulation system integrated with a transmission electron microscope- (TEM-) nanorobotic manipulator (TEM manipulator) and a scanning electron microscope- (SEM-) nanorobotic manipulator (SEM manipulator) [29]. This system allows effective sample preparation inside SEM with wide working area and many degrees of freedom (DOFs) of manipulation. It has high resolution

measurement and evaluation of samples inside a TEM capability. The sample chambers of these electron microscopes are set under the high vacuum (HV) condition to reduce the disturbance of electron beam for observation. To observe the water-containing samples, for example, biocells, drying treatment processes are additionally needed. Hence, direct observations of water-containing samples are normally quite difficult in these electron microscopes.

In the present study, we used the nanorobotic manipulators inside an ESEM [30]. It has been constructed with 3 units and 7 degrees of freedom (DOFs) in total (Figure 1). The ESEM enables direct observation of water-containing samples with nanometer high resolution by a specially built secondly electron detector. The evaporation of water is controlled by both the sample temperature (0–40°C) and sample chamber pressure (10–2600 Pa). The temperature of the sample is controlled by the cooling stage unit (Unit 3). The detailed specifications of the manipulator and the ESEM can be obtained from our previous paper [31]. The following experiments have been conducted through this system. The observation and comparison of W303 cells and spheroplast W303 were successfully performed using ESEM. Spheroplast W303 cells were obtained by enzymatic digestion which were confirmed qualitatively by the comparison of cell morphology between the cells and spheroplast cells, and quantitatively, by the OD_{800} absorbance data. The successful observation of spheroplast cells opens the possibility for a new way in the single ion channel current measurement.

2. Materials and Methods

2.1. Cell Cultures. Wild type yeast cells (W303 strains) were used for the observations and measurements under optical microscope and ESEM system. The W303 cells were cultured on a YPD plate (1% yeast extract, 2% peptone, 2% glucose, and 2% agar) in a 37°C incubator for 48 hours. A single colony was then picked from the cultured plate and then dipped into a tube containing 10 mL of YPD media. The tube was then incubated overnight in 30°C at 200 rpm. The OD_{600} values of the samples were measured by a spectrophotometer and samples that had OD_{600} values between 0.2 and 0.3 were used for spheroplasting.

2.2. Preparation of W303 Spheroplasts. Spheroplasts were prepared using Pichia spheroplast kit. In brief, logarithmic growing W303 wild type yeast cells (OD_{600} value between 0.2 and 0.3 in 1 mL of culture) were harvested by centrifugation at 6000 rpm for 5 minutes at 30°C and then washed with 1 mL of sterile water. Cells were pelleted by centrifugation at 6000 rpm for 5 minutes at 30°C.

The cell pellets were washed by resuspending in 1 mL of SED buffer containing 1 M sorbitol, 25 mM EDTA pH 8.0, and 1 M dithiothreitol and then centrifuged at 6000 rpm for 5 minutes at 30°C. The cells then were washed with 1 mL of 1 M sorbitol and centrifuged at 6000 rpm for 5 minutes at 30°C. Then, they were resuspended by swirling in 1 mL of SCE medium. A 3 μ L of cell wall hydrolyzing enzyme, Zymolyase, was added to the cells. The cells were then incubated at 30°C

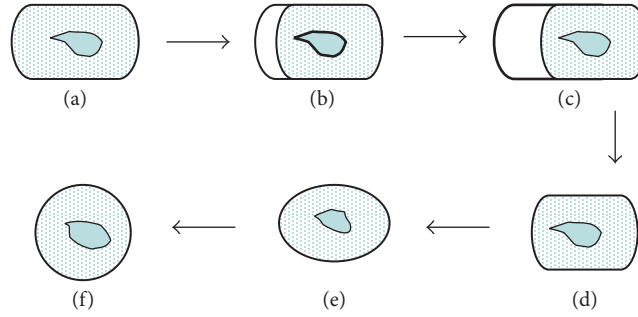


FIGURE 2: Schematic diagram illustration of the two phases in spheroplast formation. (a)–(d), Cell turns into prospheroplast. The appearance of spheroplast can be seen when the prospheroplast changes into a spherical shape ((e), (f)).

for about 1 hour. The spheroplasts were washed with 1 mL of 1 M sorbitol and collected by centrifugation at 6000 rpm for 5 minutes at 30°C. They were then resuspended in 1 mL of CaS.

A schematic diagram illustrating the spheroplast conversion is presented in Figure 2. In the first phase, the W303 cells were transformed into prospheroplasts. The prospheroplasts were extruded at one end where partial digestion of the cell wall occurred (Figures 2(a)–2(d)), retaining its shape despite the apparent loss of a supporting wall. In the second phase, the prospheroplasts rapidly transformed into spheroplasts where a spherical shape became dominant (Figures 2(e) and 2(f)).

2.3. W303 Spheroplast Observation by an Optical Microscope. The spheroplast cells were observed in four different mediums: YPD, sterile water, SCE, and CaS using Olympus IX-71 optical microscope at room temperature (20–25°C) in 100× oil immersion objective lens. The initial 1 mL spheroplast cells inside CaS medium were aliquoted into four microcentrifuge tubes. The first aliquot was the spheroplasts inside CaS medium. The other three aliquots were centrifuged at 6000 rpm for 5 minutes in 30°C and the CaS supernatant was discarded completely. The spheroplast pellets inside each of the three tubes were then resuspended with 250 μL of YPD medium, 250 μL of sterile water, and 250 μL of SCE medium, respectively.

2.4. W303 Spheroplasts Observations by ESEM. The ESEM system can perform direct observation of water-containing samples with nanometer high resolution by specially built secondary electron detector. The evaporation of water is controlled by adjusting the sample's temperature (~0–~40°C) and sample's chamber pressure (10–2600 Pa). The temperature of the sample is controlled by the cooling stage unit, that is, Unit3, as shown in Figure 1. ESEM system has a capability to control the chamber's pressure from high vacuum (~10⁻⁴ Pa) to high humidity (10–2600 Pa). The detailed specifications of the manipulator and the ESEM can be obtained from our previous paper [26]. The nanomanipulator has a tungsten probe, which has been used to transfer the single cell using the adhesion force. This force is produced between the micro probe and cell. In fact, the nanomanipulator system can control the position of a single cell.

3. Results and Discussion

3.1. Cells Morphology under Optical Microscope. Figures 3 and 4 show a comparison between the morphology of W303 cells before and after spheroplasting inside four different mediums: YPD, sterile water, SCE, and CaS. From the observations, the morphology of the W303 cells inside all four mediums had an oval shape.

YPD medium provided the best living medium for the cells, followed by sterile water, SCE, and CaS mediums (Figures 3(a)–3(d)). The reduction in number of the W303 cells in SCE and CaS media compared to the YPD (1% yeast extract, 2% peptone, 2% glucose, and 2% agar) is due to the absence of yeast extract. The yeast extract will typically contain all the amino acids necessary for growth. Figure 4 shows the morphology of spheroplast cells inside four the four mediums. It is clear that the spheroplast cells displayed a spherical shape inside all mediums. However, the condition and visibility of cells inside YPD and sterile water mediums were poor as compared to the SCE and CaS medium (Figures 4(a)–4(d)). The spherical shape for the spheroplast yeast cells was also reported by [32].

3.2. Spheroplast Conversion Percentage Based on the OD₈₀₀ Absorbance Data. The percentage of the spheroplast cells conversion can be determined from the following equation:

$$\% \text{ Spheroplast} = 100 - \left[\left(\frac{(\text{OD}_{800}|_{\text{time}=t})}{(\text{OD}_{800}|_{\text{time}=0})} \right) \times 100 \right]. \quad (1)$$

Figure 5 shows the values of OD₈₀₀ absorbance data for 50 minutes and its corresponding spheroplast conversion percentage. From the graph, it is shown that the cells rapidly changed into spheroplast cells; 85% of the cells converted into spheroplasts in 2 minutes after the addition of the digestion enzyme. The whole W303 cells completely adapted the spheroplast cells conditions in 15 minutes. From this data, it is concluded that the spheroplasting experiment was successfully achieved.

3.3. Surface Characteristic of W303 Cells and Spheroplast W303 Cells under ESEM. Figure 6 shows the surface topology of the cells under ESEM. The observations were performed at 30 kV and 100 μA. The environmental parameters

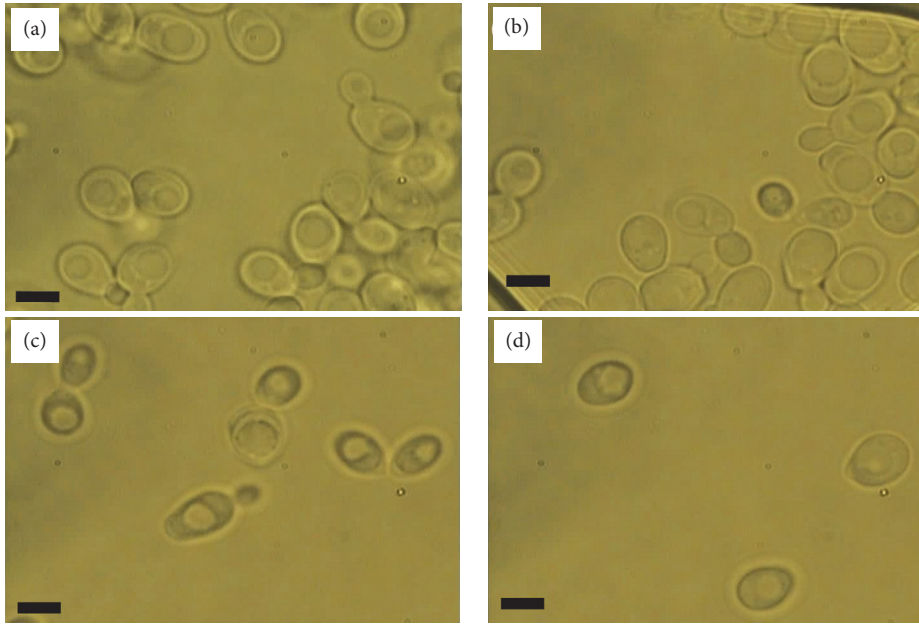


FIGURE 3: The morphology of the W303 cells inside four different mediums: (a) YPD, (b) sterile water, (c) SCE, and (d) CaS. Bar scale is $5\ \mu\text{m}$.

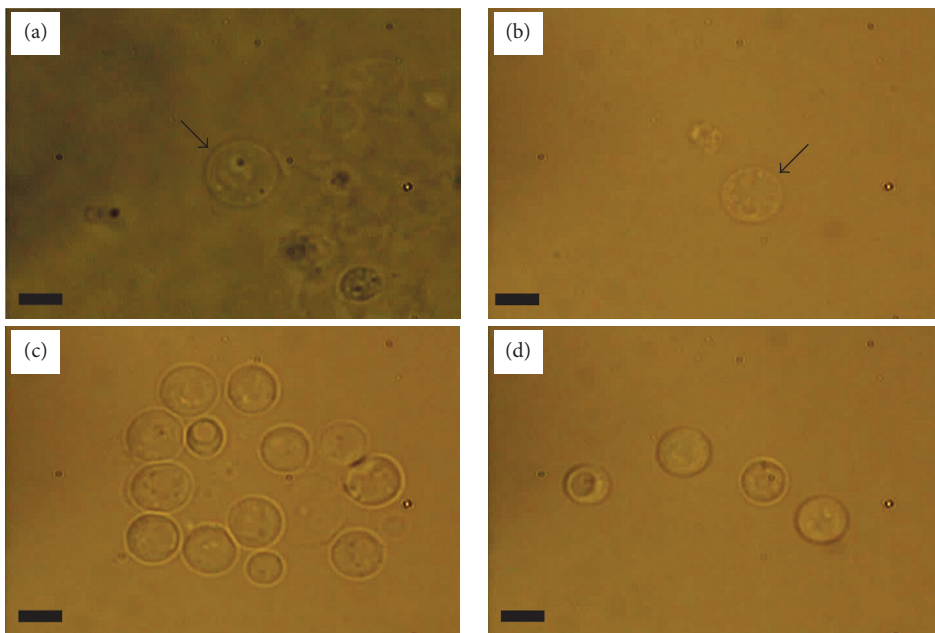


FIGURE 4: The morphology of the spheroplast W303 cells inside four different mediums: (a) YPD, (b) sterile water, (c) SCE, and (d) CaS. Arrow marks are added to indicate the position of the spheroplast cells inside the first two mediums, that is, YPD and sterile water. Bar scale is $5\ \mu\text{m}$.

settings were 600 Pa and 0°C . The whole cells were kept inside the YPD medium and diluted with distilled water. From the observation, the surfaces of the W303 cells were very smooth as can be seen (top view (Figure 6(a)), side view (Figure 6(b)), and closed-up side view (Figure 6(c))). This is also confirmed in previous literature [25, 26].

Figure 7 represents the surface topology of the spheroplast cells under an ESEM. For the first time, the observations

of spheroplast cells were performed without the need of complex sample preparation and sample coating. This will ensure the viability of the spheroplast cells that will enable further characterization and analysis to be carried out. As expected, the surface topology of the spheroplast cells was not smooth as cells having a cell wall. The significance of the cell wall as a cell shaper was highly acknowledged from these observations. In addition to the nonsmooth surface

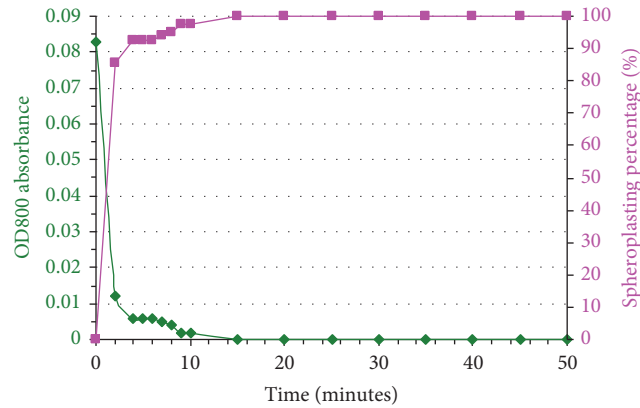


FIGURE 5: The OD₈₀₀ absorbance data and its corresponding spheroplast conversion percentage for 50 minutes of treatment using digestion enzyme; Zymolyase, on W303 cells.

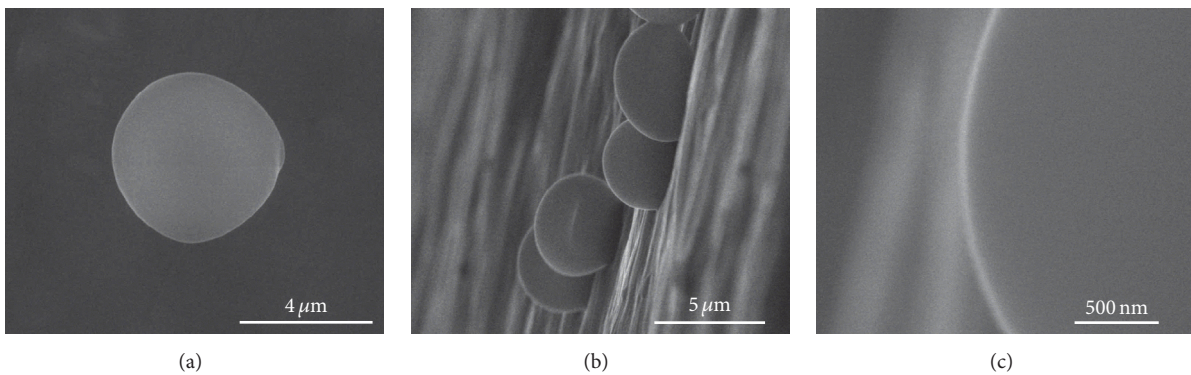


FIGURE 6: The surface topology of the W303 cells under an ESEM from different views: (a) top view, (b) side view, and (c) closed-up side view.

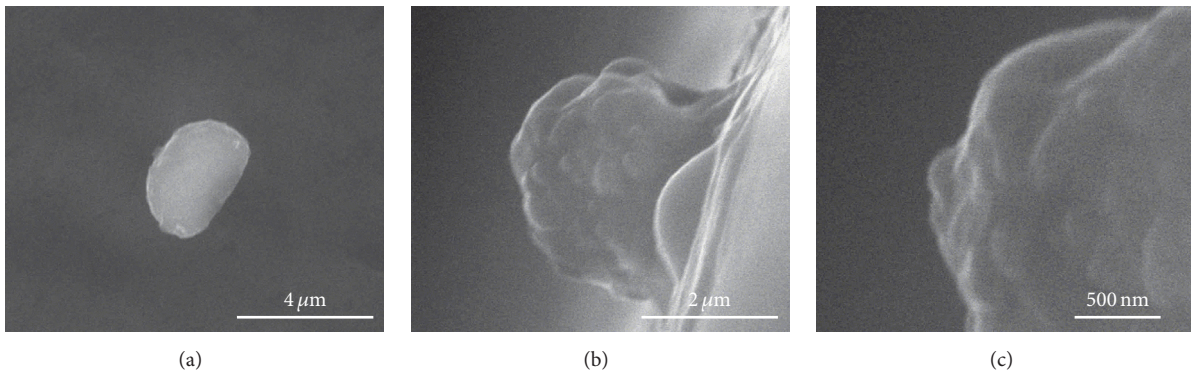


FIGURE 7: The surface topology of the spheroplast W303 cells under an ESEM from different views: (a) top view, (b) side view, and (c) closed-up side view.

topology, the spheroplast cells experienced some reduction in size as can be seen in top view image of spheroplast cell (Figure 7(a)). From the side view images (Figures 7(b) and 7(c)), it is noticed that the surface had several bleb structures.

4. Conclusion

The advantages of the integrated ESEM-nanomanipulation system rely on its capability to perform in situ local direct

observation and manipulation of biological sample and the ability to control the environmental conditions. The observations of the spheroplast without prior coating for an electron microscopy observation have been highlighted in this work. To the best of our knowledge, this work is the first to attempt to observe spheroplast cells under electron microscope without the need of sample coating. The spheroplasting was verified qualitatively and quantitatively by observing the cell's morphological change under optical

microscope observations and the spheroplast conversion percentage based on the OD₈₀₀ absorbance data. The spheroplast cells showed a spherical shape as compared to the oval shape for the normal cells. The electron microscope observation revealed the bleb-like surface of the spheroplasts as compared to the very smooth surface of the normal cells. This work could be extended to perform single ion channel current measurements on the spheroplast W303 cells inside the ESEM-nanomanipulation system.

Conflicts of Interest

The authors declare that they have no conflicts of interest.

Acknowledgments

The research was supported by the Ministry of Higher Education of Malaysia (Grant nos. 4L640 and 4F351) and Universiti Teknologi Malaysia (Grant nos. 03E11, 03G47, 02G46, 03H82, and 03H80); the authors thank them for funding this project and for their endless support. In addition, they would like to thank Professor Toshifumi Inada at Nagoya University for providing the W₃₀₃ yeast cell stains.

References

- [1] M. Yu, M. J. Dyer, G. D. Skidmore et al., "Three-dimensional manipulation of carbon nanotubes under a scanning electron microscope," *Nanotechnology*, vol. 10, no. 3, pp. 244–252, 1999.
- [2] M. A. Sutton, N. Li, D. C. Joy, A. P. Reynolds, and X. Li, "Scanning electron microscopy for quantitative small and large deformation measurements Part I: SEM imaging at magnifications from 200 to 10,000," *Experimental Mechanics*, vol. 47, no. 6, pp. 775–787, 2007.
- [3] J. I. Goldstein, D. E. Newbury, P. Echlin et al., *Scanning Electron Microscopy and X-Ray Microanalysis*, Springer US, Boston, Mass, USA, 1992.
- [4] K. C. A. Smith and C. W. Oatley, "The scanning electron microscope and its fields of application," *British Journal of Applied Physics*, vol. 6, no. 11, article 304, pp. 391–399, 1955.
- [5] L. Muscariello, F. Rosso, G. Marino et al., "A critical overview of ESEM applications in the biological field," *Journal of Cellular Physiology*, vol. 205, no. 3, pp. 328–334, 2005.
- [6] K. Hrubanova, O. Samek, A. Haronikova et al., "Morphological and production changes in stressed red yeasts monitored using sem and raman spectroscopy," *Microscopy and Microanalysis*, vol. 22, no. S3, pp. 1146–1147, 2016.
- [7] Y. Zhang, H. Wu, X. Yu, F. Chen, and J. Wu, "Microscopic observations of the lotus leaf for explaining the outstanding mechanical properties," *Journal of Bionic Engineering*, vol. 9, no. 1, pp. 84–90, 2012.
- [8] L. Bergmans, P. Moisiadis, B. Van Meerbeek, M. Quirynen, and P. Lambrechts, "Microscopic observation of bacteria: Review highlighting the use of environmental SEM," *International Endodontic Journal*, vol. 38, no. 11, pp. 775–788, 2005.
- [9] S. B. Surman, J. T. Walker, D. T. Goddard et al., "Comparison of microscope techniques for the examination of biofilms," *Journal of Microbiological Methods*, vol. 25, no. 1, pp. 57–70, 1996.
- [10] M. R. Ahmad, M. Nakajima, T. Fukuda, S. Kojima, and M. Homma, "Single cells electrical characterizations using nanoprobe via ESEM-nanomanipulator system," in *Proceedings of the 9th IEEE Conference on Nanotechnology (IEEE NANO '09)*, pp. 589–592, Genoa, Italy, July 2009.
- [11] Y. Shen, M. Nakajima, M. R. Ahmad, T. Fukuda, S. Kojima, and M. Homma, "Single cell injection using nano pipette via nanorobotic manipulation system inside E-SEM," in *Proceedings of the 9th IEEE Conference on Nanotechnology (IEEE NANO '09)*, pp. 518–521, Genoa, Italy, July 2009.
- [12] J. M. Manero, F. J. Gil, E. Padrós, and J. A. Planell, "Applications of environmental scanning electron microscopy (ESEM) in biomaterials field," *Microscopy Research and Technique*, vol. 61, no. 5, pp. 469–480, 2003.
- [13] A. M. Donald, "The use of environmental scanning electron microscopy for imaging wet and insulating materials," *Nature Materials*, vol. 2, no. 8, pp. 511–516, 2003.
- [14] G. D. Danilatos, "Introduction to the ESEM instrument," *Microscopy Research and Technique*, vol. 25, no. 5-6, pp. 354–361, 1993.
- [15] C. Gilpin and D. C. Sigeo, "X-ray microanalysis of wet biological specimens in the environmental scanning electron microscope. 1. Reduction of specimen distance under different atmospheric conditions," *Journal of Microscopy*, vol. 179, no. 1, pp. 22–28, 1995.
- [16] B. Little, P. Wagner, R. Ray, R. Pope, and R. Scheetz, "Biofilms: an ESEM evaluation of artifacts introduced during SEM preparation," *Journal of Industrial Microbiology*, vol. 8, no. 4, pp. 213–222, 1991.
- [17] S. P. Collins, R. K. Pope, R. W. Scheetz, R. I. Ray, P. A. Wagner, and B. J. Little, "Advantages of environmental scanning electron microscopy in studies of microorganisms," *Microscopy Research and Technique*, vol. 25, no. 5-6, pp. 398–405, 1993.
- [18] M. R. Ahmad, M. Nakajima, S. Kojima, M. Homma, and T. Fukuda, "A study of the spheroplast observations for W303 single cells under environmental-SEM," in *Proceedings of the International Symposium on Micro-NanoMechatronics and Human Science MHS 2008, with Symposium on "COE for Education and Research of Micro-Nano Mechatronics"*, Symposium on "System Cell Engineering by Multi-scale Manipulation", pp. 89–92, Nagoya, Japan, November 2008.
- [19] M. Baguneid, D. Murray, H. J. Salacinski et al., "Shear-stress preconditioning and tissue-engineering-based paradigms for generating arterial substitutes," *Biotechnology and Applied Biochemistry*, vol. 39, no. 2, pp. 151–157, 2004.
- [20] A. Motta, C. Migliaresi, F. Faccioni, P. Torricelli, M. Fini, and R. Giardino, "Fibroin hydrogels for biomedical applications: Preparation, characterization and in vitro cell culture studies," *Journal of Biomaterials Science, Polymer Edition*, vol. 15, no. 7, pp. 851–864, 2004.
- [21] Y. Shen, M. Nakajima, M. R. Ahmad, S. Kojima, M. Homma, and T. Fukuda, "Effect of ambient humidity on the strength of the adhesion force of single yeast cell inside environmental-SEM," *Ultramicroscopy*, vol. 111, no. 8, pp. 1176–1183, 2011.
- [22] M. R. Ahmad, M. Nakajima, S. Kojima, M. Homma, and T. Fukuda, "Buckling nanoneedle for characterizing single cells mechanics inside environmental SEM," *IEEE Transactions on Nanotechnology*, vol. 10, no. 2, pp. 226–236, 2011.
- [23] M. R. Ahmad, M. Nakajima, S. Kojima, M. Homma, and T. Fukuda, "Mechanical properties characterization of individual yeast cells using environment-SEM nanomanipulation system," in *Proceedings of the IEEE/RSJ International Conference on Intelligent Robots and Systems (IROS '07)*, pp. 596–601, Raleigh, NC, USA, November 2007.

- [24] S. E. Kirk, J. N. Skepper, and A. M. Donald, "Application of environmental scanning electron microscopy to determine biological surface structure," *Journal of Microscopy*, vol. 233, no. 2, pp. 205–224, 2009.
- [25] M. R. Ahmad, M. Nakajima, S. Kojima, M. Homma, and T. Fukuda, "The effects of cell sizes, environmental conditions, and growth phases on the strength of individual W303 yeast cells inside ESEM," *IEEE Transactions on Nanobioscience*, vol. 7, no. 3, pp. 185–193, 2008.
- [26] M. R. Ahmad, M. Nakajima, S. Kojima, M. Homma, and T. Fukuda, "In situ single cell mechanics characterization of yeast cells using nanoneedles inside environmental SEM," *IEEE Transactions on Nanotechnology*, vol. 7, no. 5, pp. 607–616, 2008.
- [27] D. Ogden, "Microelectrode techniques: the Plymouth Workshop handbook," *Company of Biologists Limited*, 1994.
- [28] M. Sokabe, F. Sachs, and Z. Jing, "Quantitative video microscopy of patch clamped membranes stress, strain, capacitance, and stretch channel activation," *Biophysical Journal*, vol. 59, no. 3, pp. 722–728, 1991.
- [29] M. Nakajima, F. Arai, and T. Fukuda, "In situ measurement of young's modulus of carbon nanotubes inside a TEM through a hybrid nanorobotic manipulation system," *IEEE Transactions on Nanotechnology*, vol. 5, no. 3, pp. 243–248, 2006.
- [30] M. Nakajima, F. Arai, and T. Fukuda, "Nanofixation with low melting metal based on nanorobotic manipulation," in *Proceedings of the 6th IEEE Conference on Nanotechnology (IEEE-NANO '06)*, pp. 925–928, Ohio, USA, June 2006.
- [31] M. R. Ahmad, M. Nakajima, S. Kojima, M. Homma, and T. Fukuda, "In-situ single cell mechanical characterization of W303 yeast cells inside environmental-SEM," in *Proceedings of the 7th IEEE International Conference on Nanotechnology—(IEEE-NANO '07)*, pp. 1022–1027, Hong Kong, China, August 2007.
- [32] S. Darling, J. Theilade, and A. Birch-Andersen, "Kinetic and morphological observations on *Saccharomyces cerevisiae* during spheroplast formation," *Journal of Bacteriology*, vol. 98, no. 2, pp. 797–810, 1969.

Research Article

Characterization of the Resistance and Force of a Carbon Nanotube/Metal Side Contact by Nanomanipulation

Ning Yu,¹ Masahiro Nakajima,² Qing Shi,¹ Zhan Yang,³ Huaping Wang,¹ Lining Sun,³ Qiang Huang,¹ and Toshio Fukuda¹

¹Intelligent Robotics Institute, Beijing Institute of Technology, Beijing 100081, China

²Department of Micro-Nano Systems Engineering, Nagoya University, Nagoya 464-0814, Japan

³Robotics and Microsystem Center, Soochow University, Suzhou 215006, China

Correspondence should be addressed to Qing Shi; shiqing@bit.edu.cn

Received 20 November 2016; Accepted 16 January 2017; Published 13 February 2017

Academic Editor: Xinyu Liu

Copyright © 2017 Ning Yu et al. This is an open access article distributed under the Creative Commons Attribution License, which permits unrestricted use, distribution, and reproduction in any medium, provided the original work is properly cited.

A high contact resistance restricts the application of carbon nanotubes (CNTs) in fabrication of field-effect transistors (FETs). Thus, it is important to decrease the contact resistance and investigate the critical influence factors such as the contact length and contact force. This study uses nanomanipulation to characterize both the resistance and the force at a CNT/Au side-contact interface inside a scanning electron microscopy (SEM). Two-terminal CNT manipulation methods, and models for calculating the resistance and force at contact area, are proposed to guide the measurement experiments of a total resistance and a cantilever's elastic deformation. The experimental results suggest that the contact resistance of CNT/Au interface is large (189.5 k Ω) when the van der Waals force (282.1 nN) dominates the contact force at the interface. Electron-beam-induced deposition (EBID) is then carried out to decrease the contact resistance. After depositing seven EBID points, the resistance is decreased to 7.5 k Ω , and the force increases to 1339.8 nN at least. The resistance and force at the contact area where CNT was fixed exhibit a negative exponential correlation before and after EBID. The good agreement of this correlation with previous reports validates the proposed robotic system and methods for characterizing the contact resistance and force.

1. Introduction

The era of scaling silicon field-effect transistors (FETs) to ever-smaller dimensions is coming to a close. As an alternative to silicon, carbon nanotubes (CNTs) have received much interest because of their excellent mechanical [1, 2], electrical [3, 4], and thermal properties [5]. Many kinds of CNT-FETs have been fabricated, such as back-gated [6], top-gated [7], and gate-all-around [8]. However, high contact resistance between CNTs and drain/source metal electrodes limits the performance of CNT-FETs due to different work function. It is a challenge to decrease the contact resistance and to clarify the influence factors such as contact length and contact force at the interface.

The contact resistance was usually extracted from a total resistance between the CNTs and electrodes, rather than being directly measured experimentally. A typical measurement of total resistance [9] initially involved dispersing CNT

solution on a Si wafer containing an electrode pair. Once CNTs bridged on the electrode pair, the total resistance across the two terminals was then measured. This method was easily carried out, but the likelihood of a CNT bridging the electrode pair was highly uncertain. Dielectrophoresis (DEP) technology improved the controllability of the CNT bridging process [10]. Bridging could be achieved using a tiny number of CNTs, and CNTs with specific properties could even be selected prior to assembly. However, the DEP process required many parameters to be regulated, such as the intensity, frequency, and duration of the applied electrostatic field [11, 12]. It was difficult to sufficiently control these parameters to achieve the specifically desired contact conditions, for example, a specific contact length. Micronanomanipulators have achieved a wide range of applications on electronic industry and biomedicine in recent decades, such as a unique microgripper with dual-axis force sensor [13] and nanomanipulators based on an Atomic Force Microscope (AFM) [14].

They are promising for good controllability of the targets. In our previous work, we successfully used nanorobotic manipulators inside a SEM to develop individual-CNT-based nanoposition sensors for the detection of approaching, touching, and sliding positions [15]. The controllability of nanorobotic manipulation provides an effective method to flexibly adjust the contact length of individual CNT.

For reducing the contact resistance, many techniques have been investigated. Joule heating was reported to be effective by Wang et al. [16]. They obtained a low ohmic contact resistance of $700\ \Omega$ between a multiwalled CNT (MWCNT) and tungsten (W) surface. Rapid thermal annealing at $600\text{--}800^\circ\text{C}$ for 30 s was used by Lee et al. [17]. They obtained the contact resistance of $0.5\text{--}50\ \text{k}\Omega$ between a CNT and Au. Such progress was significant, but these techniques were limited by intense heat release at the contact junction, which led to poor control of the contact area/geometry. Focused ion-beam-induced deposition (IBID) could provide good spatial and time-domain control of the chemical vapor deposition of various materials [18]. It was used to form in situ contacts in CNT devices [19], and IBID with tungsten yielded an ohmic contact with CNTs [20, 21]. However, the focused ion beam damaged CNTs during long observation durations. Electron-beam-induced deposition (EBID) was similarly applied, but with minimal damage to the CNT. For example, Kim et al. used EBID with carbon to decrease the contact resistance [22], and Brintlinger et al. used EBID with gold to achieve a contact resistance of $10\ \text{k}\Omega$ [23].

Much progress has been made on measuring and decreasing the contact resistance. However, it is important to also investigate critical influence factors such as the metal work function and wettability, the contact length, or contact area, as well as the contact force. The effect of work function and wettability was studied by using fourteen different metals for CNT interconnections [24]. The effect of contact length was investigated by laser ablation with fixed CNT diameters [25] and by silicon-compatible test structures with a small range of CNT diameters [26]. As for the contact force, Greenwood and Williamson investigated the contact between nominally flat metal/metal surfaces [27], and experimental results implied a simple law $R \propto F^{-0.9}$, where R was the contact resistance and F was the contact force. Based on our previous study, the connection force between CNT/CNT junctions was confirmed to be composed of van der Waals force, EBID fixing force, and chemical bonding force, respectively [28, 29]. Furthermore, we quantized the van der Waals force at a CNT/metal end-contact interface by measuring a probe deflection [30]. However, a clear understanding of contact force at the CNT/metal side-contact interface still remains elusive. Additionally, to the best of our knowledge, there is no study to find its relationship with contact resistance.

In this paper, we present two-terminal methods to characterize the contact resistance at a CNT/metal side-contact interface and to investigate the contact force by using a nanorobotic system inside a field emission scanning electron microscopy (FE-SEM). This method allows CNTs to be individually manipulated, and its superiority in varying the arbitrary contact length in situ compared to the typical four-probe measurement [17, 31] shows a controllable CNT

bridging process for the measurement of total resistance. EBID is carried out here to further control the contact area with tungsten deposits one by one and significantly decrease the contact resistance, which yields a strong CNT support with potential application on semiconductor nanodevices. Furthermore, the nanorobotic system is used to measure and analyze the force of a MWCNT/Au side-contact interface before and after EBID. It provides insight into the relationship between the contact force and the contact resistance.

2. System Configuration and Methods

A robotic system with two nanomanipulators was used here within a FE-SEM apparatus to measure a total resistance and characterize the force of a CNT/Au side-contact interface. Two-terminal CNT manipulation methods and calculation models were then developed to obtain the contact resistance and contact force.

2.1. System Configuration. A two-terminal method was used to obtain the contact resistance at the CNT/Au interface, so the robotic system was configured with two manipulators based on a FE-SEM apparatus (JSM-6500F, JEOL), as shown schematically in Figure 1. Both of the manipulators were driven by picomotors (830I-UHV, Newport) in x - y - z directions with a resolution of 30 nm. Two AFM cantilevers covered with layers of Au (OMCL-TR400PB-1, OLYMPUS) were mounted on the manipulators as the end effectors. A MWCNT forest prepared by Arc charge method was placed on top of the sample stage. Tungsten hexacarbonyl ($\text{W}(\text{CO})_6$, MKBR3026V, SIGMA-ALDRICH) was introduced into the specimen chamber as the precursor for EBID with tungsten. A visual-based force feedback system was developed with the robotic system for real-time manipulation (not shown in Figure 1).

The AFM cantilevers were able to be mounted in different orientations to achieve different tasks. Horizontally fixing the two AFM cantilevers allowed the total resistance to be measured, as shown in Figure 2. Changing the orientation of one cantilever to vertical orientation allowed the contact force to be characterized, as shown in Figure 3(a).

2.2. Calculation Model of Contact Resistance. Figure 2 shows that a single CNT bridging two AFM cantilevers is used to obtain the side-contact resistance between the MWCNT and Au electrodes. The total resistance is measured between the two cantilevers by connecting with a source measure unit (Model 6430, Keithley) outside the FE-SEM apparatus.

To form the bridge with a single CNT, a CNT is initially picked up by manipulator 1 (M1) assisted by EBID [32]. This CNT is carried towards cantilever 2 (C2) on manipulator 2 (M2) and overlapped with cantilever C2 by some arbitrary length as we wish. As M1 slowly moves downward, sufficiently small distance between the CNT and cantilever C2 results in the CNT being attracted to the Au surface of cantilever C2 by van der Waals forces. The total resistance between the two cantilevers is then measured by Model 6430, Keithley. EBID with tungsten (W) can then be deposited at the CNT/Au interface to reduce the contact resistance at contact area 2 (A2).

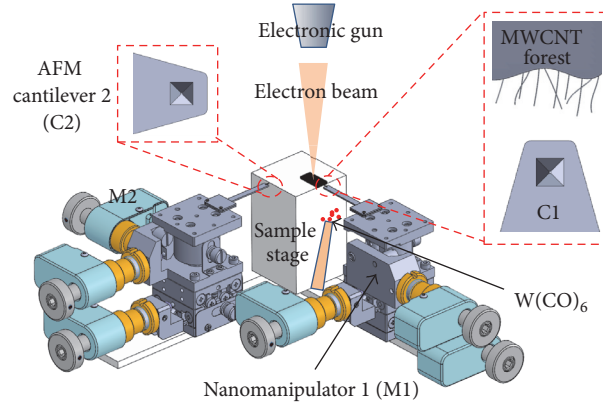


FIGURE 1: Schematic of the robotic system for characterizing the side contact between a CNT and metal electrodes inside a FE-SEM apparatus. M1 and M2 indicate manipulators 1 and 2, respectively. C1 and C2 indicate AFM cantilevers 1 and 2, respectively.

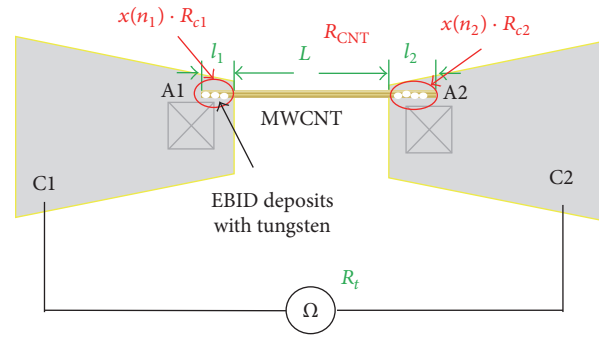


FIGURE 2: Schematic of the experimental setup used to measure the total resistance. R_t is the total resistance between cantilevers C1 and C2. R_{c1} and R_{c2} are the preliminary resistance of the CNT/Au side contact before EBID at contact areas 1 (A1) and 2 (A2), respectively. $x(n_1)$ and $x(n_2)$ are coefficients of the resistance variation before and after EBID; n_1 and n_2 are the numbers of EBID deposits at A1 and A2. R_{CNT} is the resistance of CNT. l_1 and l_2 are the contact lengths at A1 and A2. L is the gap length of the selected CNT.

As shown in Figure 2, the total resistance R_t between the two cantilevers is derived from the following equation:

$$R_t = x(n_1) \cdot R_{c1} + R_{CNT} + x(n_2) \cdot R_{c2}, \quad (1)$$

where R_{c1} and R_{c2} are the preliminary resistances of the CNT/Au side contact before EBID at contact areas A1 and A2, respectively, $x(n_1) \cdot R_{c1}$, and $x(n_2) \cdot R_{c2}$ are the resistances at A1 and A2 after EBID, $x(n_1)$, and $x(n_2)$ are the coefficients of the resistance variation after EBID, n_1 and n_2 are the numbers of EBID deposits at A1 and A2, and R_{CNT} is the CNT resistance.

R_t is able to be obtained directly from the source measure unit. $x(n_1) \cdot R_{c1}$ is a constant resistance, since the contact condition at A1 is constant as long as CNT is selected and picked up. In this case, we define $R_{nc1} = x(n_1) \cdot R_{c1}$. R_{CNT} is equal to a product of the resistivity r_{CNT} and length L . R_{c2} is derived from dividing the preliminary contact resistivity before EBID (ρ_{c2}) by the contact length between CNT and C2 (l_2) [25]. After EBID with tungsten deposition, the resistance at A2 can be expressed by $x(n_2) \cdot R_{c2}$. Specifically, $x(n_2) \cdot R_{c2}$ is composed of the contact resistances of CNT/Au, Au/W, and W/CNT interfaces and the resistances of W deposits [33]. Despite an increased resistance caused by newly added contact resistances of Au/W and W/CNT interfaces and the

resistances of W deposits, W deposition ensures electrical rigid contact benefitting for electron transport. As a result, the total resistance $x(n_2) \cdot R_{c2}$ at A2 is decreased. $x(n_2)$ and $x(n_2) \cdot R_{c2}$ can be changed by controlling l_2 and n_2 . Thus, in the current study, the contact resistance refers only to that at A2.

Assuming that the CNT sample is defect-free and that r_{CNT} and ρ_{c2} are uniform along the CNT axis, then the following can be derived from (1):

$$R_t = R_{nc1} + r_{CNT} \cdot L + x(n_2) \cdot \frac{\rho_{c2}}{l_2}. \quad (2)$$

When $n_2 = 0$, arbitrarily changing l_2 by controlling M1 or M2 will lead to different values of R_t . Analyzing R_t under different situations yields ρ_{c2} and R_{c2} before EBID. Furthermore, $x(n_2)$ and $x(n_2) \cdot R_{c2}$ after EBID can be calculated by analyzing different values of R_t measured with increasing n_2 when l_2 is fixed.

2.3. Calculation Model of Contact Force. The mechanical and electrical contact condition is affected by the applied contact force. Therefore, monitoring the force of the CNT/Au contact is necessary. Based on the method of measuring the total resistance in Section 2.2, the force of the CNT/Au side contact includes contributions from two kinds of force. One is the

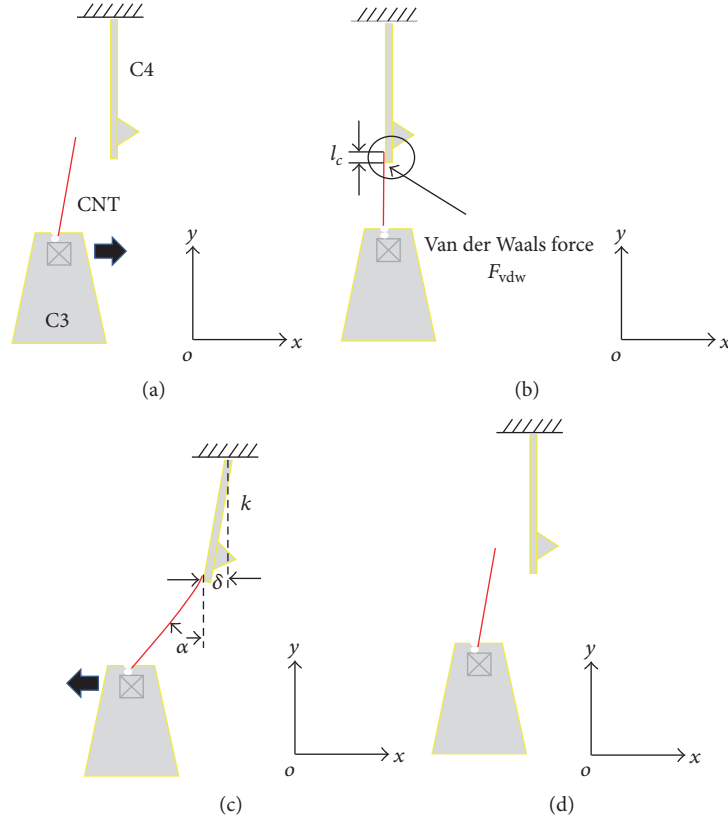


FIGURE 3: Schematic of the experimental setup used to measure the contact force. (a) CNT on cantilever 3 (C3) approaching cantilever 4 (C4). (b) The CNT attracted to the side of C4 with contact length l_c . (c) Elastic deformation of C4. (d) CNT release and recovery of C4.

attractive van der Waals force at the CNT/Au interface before EBID. The other force is the fixing force of EBID deposits. Electrostatic forces are omitted since the CNT and AFM cantilevers are well grounded.

To quantify the contact force, elastic deformation of cantilever 4 (C4) is intended to measure, which is derived from the two kinds of force at the CNT/Au interface. The principle and manipulation strategy are shown schematically in Figure 3. The robotic system still contains two cantilevers C3 and C4. C3 is horizontally bounded on M1, while C4 is vertically orientated on M2, shown in Figure 3(a). C3 is used to pick up a single MWCNT from the CNT forest. The picked CNT is then allowed to contact with the side of C4 by van der Waals forces (F_{vdw}), as shown in Figure 3(b). After good contact, C3 is moved in the x -axis, and C4 thereby experiences an elastic deformation δ , as shown in Figure 3(c). With increasing of δ , the elastic restoring force on C4 becomes larger than F_{vdw} , and it leads to the CNT release and C4 in situ recovery, as shown in Figure 3(d).

Obviously, cantilever C4 is acted by two forces: one is the van der Waals force at the CNT/Au contact interface, and the other is the elastic resilience force resulting from elastic deformation. According to the law of force balance, the van der Waals force per unit contact length (f_{vdw}) is obtained as follows:

$$f_{vdw} = \frac{F_{vdw}}{l_c} = \frac{k\delta_{max}}{l_c}, \quad (3)$$

where F_{vdw} is the van der Waals force, l_c is the CNT/Au contact length on C4, k is the spring constant of C4, and δ_{max} is the maximum deformation at the moment of CNT release.

Similarly, when EBID deposits are formed at the CNT/Au interface on C4, the total force (F_t) including contributions from F_{vdw} and a fixing force of EBID (F_{EBID}) is expressed as

$$F_t = F_{vdw} + F_{EBID} = k\delta_{max}. \quad (4)$$

The fixing force per EBID deposit (f_{EBID}) is

$$f_{EBID} = \frac{k\delta_{max} - F_{vdw}}{n}, \quad (5)$$

where n is the number of EBID deposits.

3. Experimental Results and Discussion

In this section, the total resistance was measured with varying the contact length (l_2) and increasing the number of EBID deposits (n_2). The contact resistance at A2 was calculated by analyzing these measured total resistances using the above proposed calculation model. The van der Waals force and the EBID fixing force at the CNT/Au interface were also investigated by measuring the deformation of C4.

3.1. Experimental Materials. The MWCNT forest used in these experiments was synthesized by Arc charge method. Their length was $\sim 20 \mu\text{m}$, and the diameter was 20–50 nm.

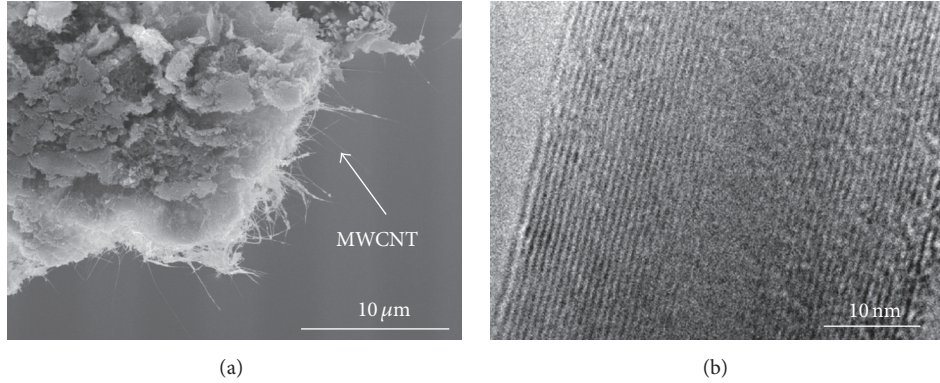


FIGURE 4: The MWCNT samples. (a) SEM image. (b) TEM image.

Figure 4 shows the SEM and TEM images of these MWCNT samples.

Each cantilever chip (OMCL-TR400PB-1) consisted of two different length levels. The 100 and 200 μm -long level had spring constant of 0.09 and 0.02 N/m, respectively. The Au coating thickness was 40–50 nm.

3.2. Experimental Conditions

- (1) The SEM chamber pressure was approximately 10^{-4} Pa.
- (2) The beam current was 0.01 nA.
- (3) The acceleration voltage was 10 kV.
- (4) The mean deposited length per minute of a EBID point was 37 nm/min when using $\text{W}(\text{CO})_6$, and its maximum diameter was about 100 nm.

3.3. Results of Contact Resistance. A longer, straight CNT was targeted from the CNT forest. Cantilever C1 was controlled to contact the CNT fixed by EBID and then to pick the CNT up. This process was shown in Figures 5(a) and 5(b). The diameter of the picked CNT was 28 nm, and the contact length l_1 was 940 nm. Five EBID points were deposited, each with deposition time of 3 min. Then, we bridged the selected CNT to C2 with a contact length l_2 of 0.43 μm , as shown in Figure 5(c). The contact length was a visually determined length after we confirmed the CNT was firmly contacted with the Au surface at A2. After bridging the CNT, electron beam was turned off to avoid the irradiation on the electrical contact of CNT/Au interface [33], and three minutes later, we measured the total resistance of the two cantilevers by using the source measure unit. The unit generated a sweep voltage, and a PC recorded the current passing through the CNT. To avoid unwanted heating effects, the voltage was constrained to 0–0.2 V, and its step size was 0.002 V. Figure 5(d) showed the measured I - V curve, from which an average total resistance of 1010 ± 104 k Ω was obtained. After this test, electron beam was turned on, and C1 was moved such that the CNT was released from C2 and then allowed to form a new contact with a contact length l_2 . The total resistance was then measured once more. This

procedure was carried out four times. In the four tests, each value of contact length l_2 yielded a different total resistance, respectively, whereas the CNT resistivity r_{CNT} and the contact resistivity ρ_{c2} were constants. Based on (2), we could obtain these parameters as listed in Table 1. Table 1 showed that a larger contact length resulted in a lower contact resistance. The contact length of 1.34 μm resulted in a contact resistance of 189.5 k Ω . However, this result was still much higher than ideal value. Theoretically, the contact resistance is governed by the quantum limit, and in the case of ideal contacts, it is 6.45 k Ω accounting for two conduction channels per CNT shell [9]. EBID technique was then applied to decrease the resistance.

Fixing the contact length l_2 at 1.34 μm , EBID points (each with a 3 min deposition time) were deposited on the CNT/Au interface at A2. The number of deposited points ranged from one to seven, and the corresponding total resistance was measured with electron beam being off after each EBID deposit. The experimental results were shown in Figure 6. Since images with increasing the number of EBID points were very similar, images from 2–6 EBID points were not shown in Figure 6. The I - V curves in Figures 6(b), 6(d), and 6(f) were linear, indicating an ohmic contact in each test. Total resistances were obtained from these I - V curves and were listed in Table 2. Resistances after EBID at A2 were then calculated using (2), and a contact resistance of 7.5 k Ω was obtained finally after seven EBID deposits, which was in good agreement with the theoretical value and previously reported experimental values demonstrated in [17, 23]. Compared with the preliminary contact resistance of 189.5 k Ω ($n = 0$), the resistance at A2 was decreased by 96.0% ($x_{(n2)} = 4.0$).

3.4. Results of Contact Force. We first tested the van der Waals force F_{vdw} of a CNT and Au side contact before EBID in this section. After a single MWCNT (outer diameter of 25 nm) pick-up by C3, it was moved to gradually approach C4 in a vertical orientation, as shown in Figure 7(a). The CNT then attractively contacts the side of the Au surface by F_{vdw} with contact length l_c shown in Figure 7(b), and M1 began to move to the left. C4 also moved following C3 and generated an elastic deformation δ shown in Figure 7(c). Finally, the CNT was released when the van der Waals force became less than

TABLE I: The total resistance and contact resistance before EBID.

Tests	Contact length l_2 (μm)	Total resistance R_t ($\text{k}\Omega$)	Contact resistivity ρ_{c2} ($\text{k}\Omega \cdot \mu\text{m}$)	Contact resistance R_{c2} ($\text{k}\Omega$)
1	0.43	1010 ± 104	254.0	590.7
2	0.70	755 ± 35.4	254.0	362.9
3	1.12	598 ± 26.7	254.0	226.8
4	1.34	387 ± 26.1	254.0	189.5

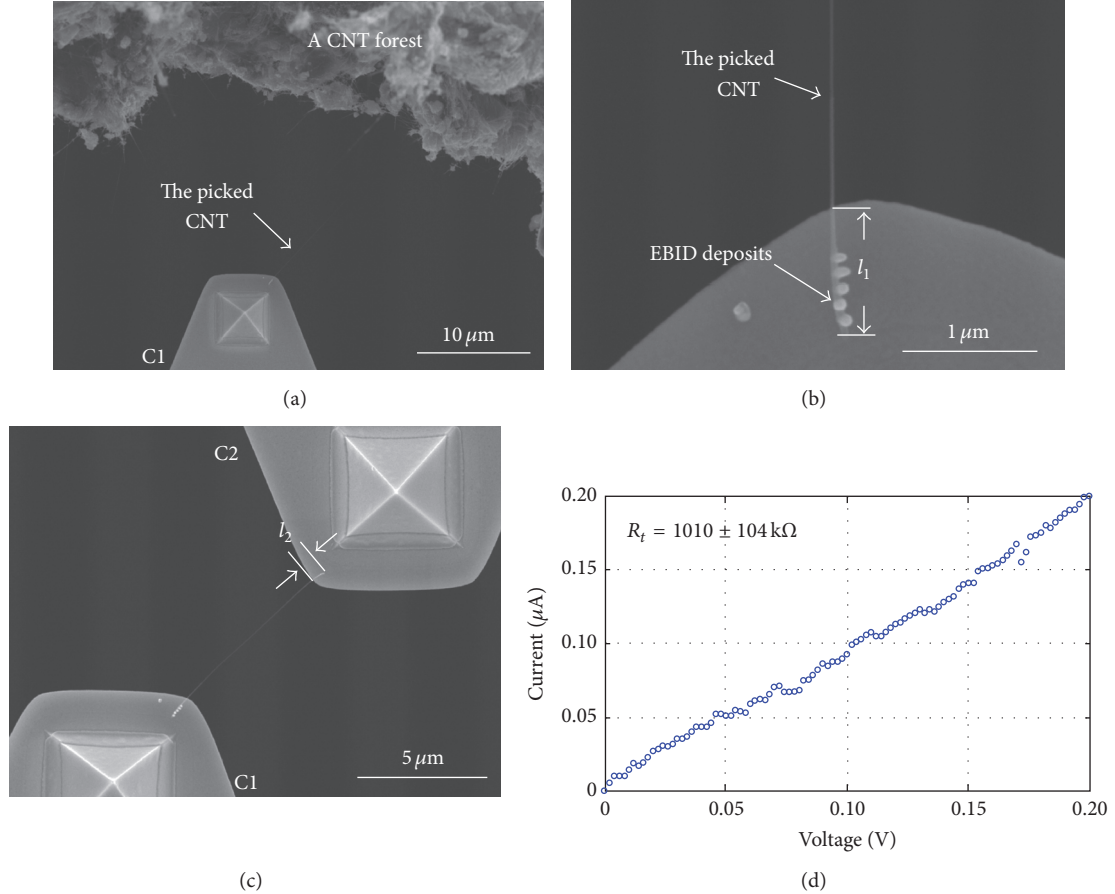


FIGURE 5: Measurement of total resistance of the CNT/Au side contact before EBID. (a) CNT selection and pick-up. (b) Magnification of the picked CNT and EBID deposits on C1. (c) Bridging of the CNT to C2. (d) Measured I - V curve from which total resistance was obtained.

the recovery force of C4, as shown in Figure 7(d). A video recording of this process was used to measure δ_{\max} . Four measurements of δ_{\max} were carried out and the resulting data were summarized in Table 3. Using (3), the van der Waals force per unit contact length (f_{vdw}) was then calculated. The f_{vdw} values for the four δ_{\max} measurements were 208.9, 209.7, 222.4, and 200.8 $\text{nN}/\mu\text{m}$, and the average was $210.5 \text{ nN}/\mu\text{m}$. To verify this result, a theoretical value was calculated from $f_{\text{vdw}} = H\sqrt{D}/16d^{5/2}$, where Hamaker constant H was $12.46 \times 10^{-20} \text{ J}$ [34], outer diameter of the CNT D was 25 nm, and the distance between the CNT and Au surface was assumed to be 0.5 nm. The calculated result f_{vdw} was $220.1 \text{ nN}/\mu\text{m}$, which was comparable to the above experimental result. This validates the proposed method for measuring the force of the CNT/Au contact.

The total force with one EBID deposit was measured similarly. A picked CNT from cantilever C3 was bridged to the pyramidal tip of cantilever C4, as shown in Figure 8(a). One EBID point was then deposited on the interface to fix the CNT. The original state of the two cantilevers after CNT bridging was shown in Figure 8(b). Cantilever C3 was moved and formed a resulting deformation at C4 in Figure 8(c). The CNT was under tension in this process and finally broke in the middle in Figure 8(d) when its stress limit was surpassed. Four tests were carried out with recording of the experimental data and the measured δ_{\max} in Table 4, in which test 1 and test 2 used the same CNT sample, and tests 3 and 4 used two further samples. Additionally, contact length in test 2 was approximated to be zero in Table 4 because only the CNT end-point touched the Au surface of the cantilever.

TABLE 2: The total resistance and the resistance at A2 after EBID.

Number of EBID points n_2	The total resistance R_t (k Ω)	The resistance at A2 $x(n_2) \cdot R_{c2}$ (k Ω)	$x(n_2)$ (%)
0	387 ± 26.1	189.5	100
1	219 ± 10.1	21.5	11.3
2	215 ± 6.6	17.5	9.2
3	209 ± 2.5	11.5	6.1
4	216 ± 9.0	18.5	9.8
5	209 ± 8.5	11.5	6.1
6	208 ± 17.0	10.5	5.5
7	205 ± 10.5	7.5	4.0

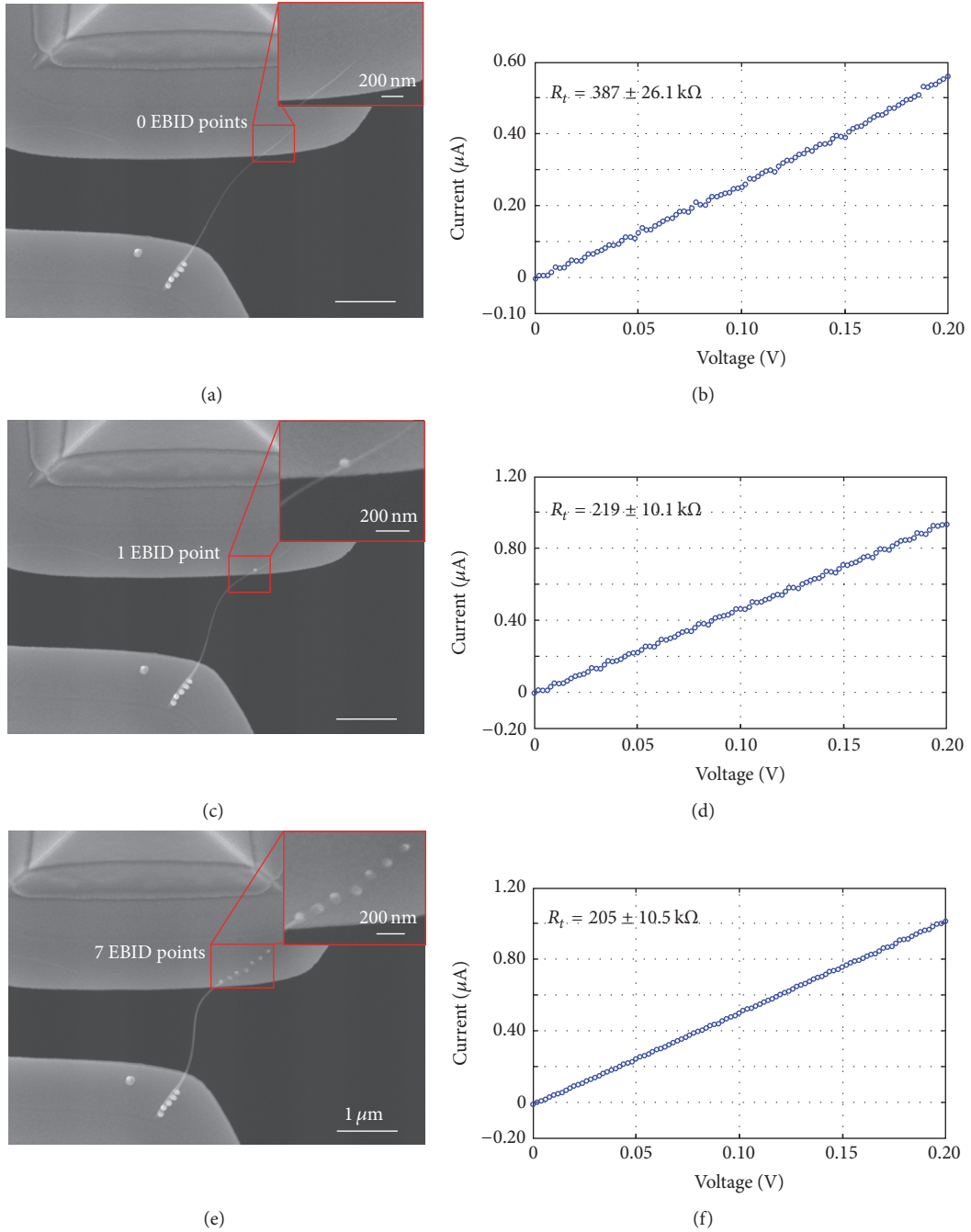


FIGURE 6: Measurement of total resistances with increasing number of EBID deposits. (a), (c), and (e) show SEM images of the bridged CNT with 0, 1, and 7 EBID deposits at A2, respectively. (b), (d), and (f) show the corresponding I - V curves recorded by a Keithley 6430 source measure unit. Scale bar indicates $1 \mu\text{m}$.

TABLE 3: Measurement of the van der Waals force at the CNT/Au interface before EBID.

Tests	Contact length l_c (μm)	Spring constant k (N/m)	Deformation δ_{max} (μm)	Van der Waals force per unit contact length f_{vdw} (nN/ μm)
1	0.18	0.02	1.88	208.9
2	0.29	0.02	3.04	209.7
3	0.49	0.02	5.45	222.4
4	1.08	0.09	2.41	200.8

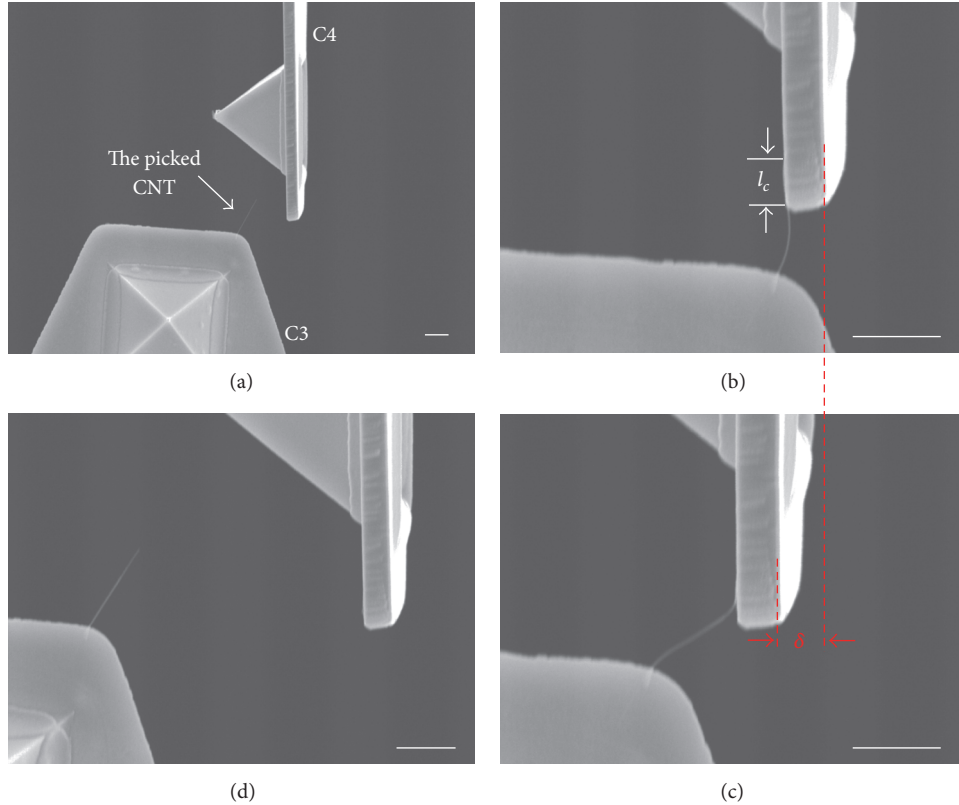


FIGURE 7: Measurement of van der Waals force at the CNT/Au interface. (a) A picked CNT approaching cantilever C4. (b) Attracted contact of CNT/Au side surface with C4. (c) Coordinated motion of C4 following C3. (d) CNT release from C4. Scale bar indicates $1 \mu\text{m}$.

All of the CNT samples were broken in the experiment, so we could only estimate the value of the total contact force within a range instead of obtaining an exact value. Actually, the contact force after EBID was strong enough to enhance the electrical rigid contact at CNT/Au interface and to decrease the resistance by improving the electron transport. Considering the cantilever tip angle of 70° , the total force in these four tests was more than 96.2, 151.1, 183.1, and 179.4 nN, respectively. The resulting f_{EBID} values were calculated using (5) and were more than 66.7, 151.1, 130.5, and 80.5 nN, respectively.

The EBID that used to decrease contact resistance in this study not merely well controlled the size of the contact area but also increased the contact force. The contact area and contact force were closely related to the size and shape of EBID deposits, which were in turn influenced by many factors such as the electron beam energy and the location of incidence. This study focused on investigating a valid

method for measuring the contact resistance and contact force and the relationship between them. Thus, all of the factors affecting the size and shape of EBID deposits were kept constant in these experiments. In terms of this point, the f_{EBID} values for the four tests should in theory have been comparable. The larger deviation in these values was caused by the different break positions and varying tensile stresses of the CNT samples. We concluded that f_{EBID} was >151.1 nN.

Additionally, based on our previous work, the fixing force at the CNT/Au contact area was increased with more than 30 s electron irradiation when the contact area was magnified to be 30,000 times [30]. Therefore, all of the tests on the force measurement in this study were carried out with a smaller magnification (less than 10,000 times). In case of larger magnification for confirming the contact condition between CNT and Au surface, the observation usually took less than 30 s to reduce the electron irradiation as much as possible.

TABLE 4: Measurement of EBID fixing force at the CNT/Au interface.

Tests	1	2	3	4
Number of EBID points	1	1	1	1
Contact length l_c (μm)	0.14	≈ 0	0.25	0.47
Spring constant k (N/m)	0.02	0.09	0.09	0.09
Deformation δ_{max} (μm)	14.06	4.91	5.95	5.83
$k\delta_{\text{max}}$ (nN)	281.2	441.9	535.5	524.7
Total contact force (nN)	>96.2	>151.1	>183.1	>179.4
Calculated F_{vdw} (nN)	29.5	≈ 0	52.6	98.9
The fixing force of EBID f_{EBID} (nN)	>66.7	>151.1	>130.5	>80.5

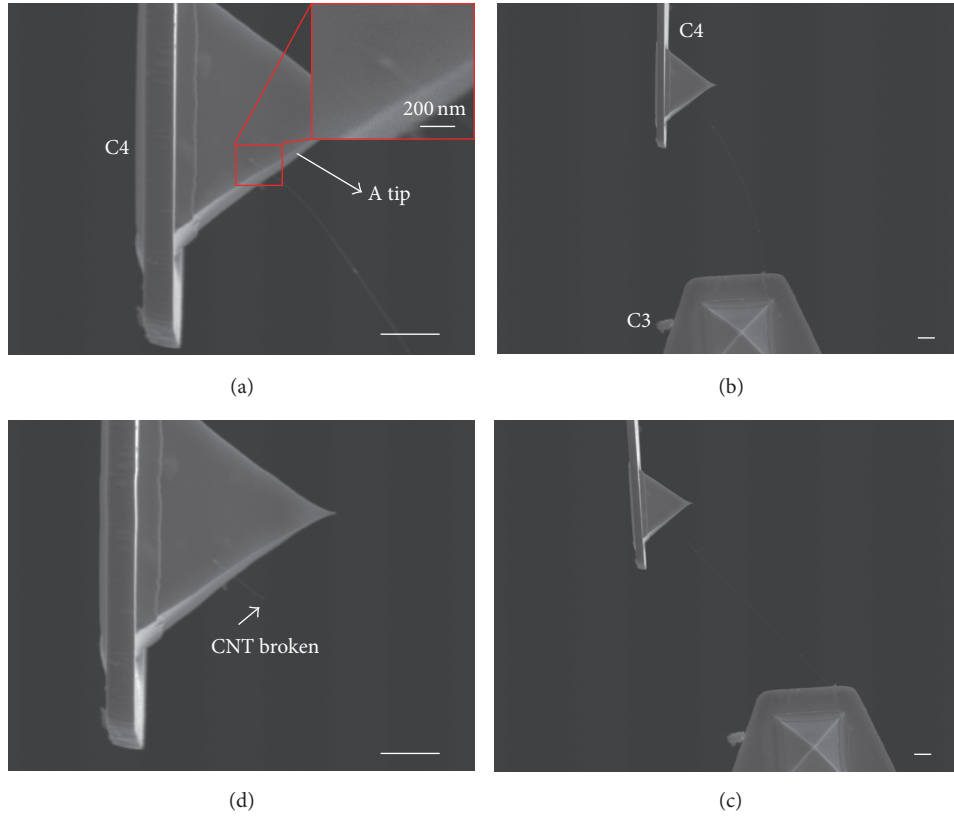


FIGURE 8: Measurement of EBID fixing force. (a) A picked CNT bridging to the tip of cantilever C4 with one EBID point from cantilever C3. (b) The original state of the two cantilevers after CNT bridging. (c) Coordinated motion of C4 following C3. (d) Stretched CNT broken in the middle and C4 recovered. Scale bar indicates $1 \mu\text{m}$.

3.5. Relationship between the Resistance and the Force of the CNT/Au Side Contact. Table 1 showed the contact resistance for different contact lengths before EBID, in which the van der Waals force per unit contact length (f_{vdw}) was $210.5 \text{ nN}/\mu\text{m}$. Thus, the contact force before EBID (i.e., the van der Waals force) in the four tests was calculated to be 90.5, 147.4, 235.8, and 282.1 nN. Furthermore, since f_{EBID} was $>151.1 \text{ nN}$, the total force at the CNT/Au contact area after seven EBID deposits was $>1339.8 \text{ nN}$. Other cases are summarized in Table 5. The contact resistance $x(n_2) \cdot R_{c2}$ and the force F_t before/after EBID in Table 5 were fitted to a very simple

proportion $x(n_2) \cdot R_{c2} \propto F_t^{-1.26}$, as shown in Figure 9. From Figure 9, the contact resistance became smaller with an increased contact force. This was explained by the fact that the contact resistance is inversely proportional to the contact area, while the contact area becomes larger with the increased contact force. Additionally, Figure 9 was obtained by setting $f_{\text{EBID}} = 151.1 \text{ nN}$ for the convenience of fitting. This setting affected the fitting index of F_t , and $x(n_2) \cdot R_{c2} \propto F_t^{-1.15}$ would be obtained if f_{EBID} was set to 300 nN . Increasing f_{EBID} to 1500 nN yielded $x(n_2) \cdot R_{c2} \propto F_t^{-1.00}$. Thus, the contact resistance was negative-exponentially related to the contact

TABLE 5: Resistance and force of the CNT/Au contact before and after EBID.

Tests	Contact length l_2 (μm)	Number of EBID deposits	Resistance at A2 (k Ω)	The force F_t before EBID (nN)	Total force F_t after EBID (nN)
1	0.43	0	590.7	90.5	
2	0.70	0	362.9	147.4	
3	1.12	0	226.8	235.8	
4	1.34	0	189.5	282.1	
5	1.34	1	21.5		>433.2
6	1.34	2	17.5		>584.3
7	1.34	3	11.5		>735.4
8	1.34	4	18.5		>886.5
9	1.34	5	11.5		>1037.6
10	1.34	6	10.5		>1188.7
11	1.34	7	7.5		>1339.8

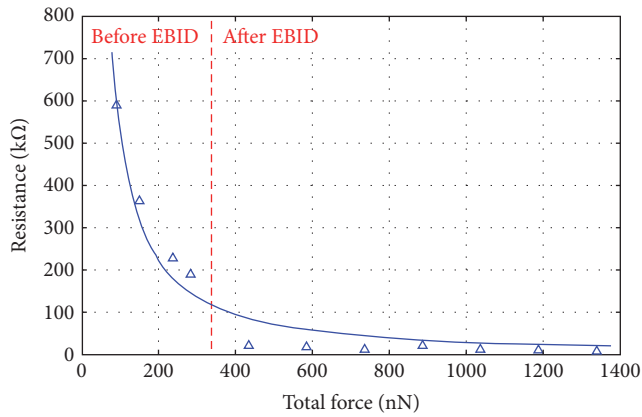


FIGURE 9: Relationship between the force and the resistance of the CNT/Au contact before and after EBID. Hollow triangles represent the contact resistance under the different contact force, whereas the solid line represents a fitting of these experimental data.

force. This negative-exponentially relationship was similar to the reported $R \propto F^{-0.90}$ [27] and $R \propto F^{-0.94}$ [35], which proved the validity of our method.

4. Conclusions

This paper reported a nanorobotic system containing two manipulators within a SEM apparatus. This system allowed both the contact resistance and the force between a MWCNT and Au-coated cantilevers to be measured before and after EBID. Experimental results showed a contact resistance of 189.5 k Ω before EBID and a decreased resistance of 7.5 k Ω after 7 EBID deposits. Contact force at the CNT/Au interface before EBID was measured to be 210.5 nN/ μm and increased by >151.1 nN per EBID point. Fitting the experimental data yielded a negative exponential relationship between the resistance and force of the contact area, and good agreement of the relationship with previous reports validated the proposed method. In future, our robotic system will be expanded to investigate the contact between CNTs and other metals and

to fabricate nanodevices such as CNT-FETs in combination with EBID.

Competing Interests

The authors declare that there is no conflict of interests regarding the publication of this paper.

Acknowledgments

This work was supported in part by the National Natural Science Foundation of China (NSFC) under Grant nos. 61433010, 61375108, and 61603044 and the Beijing Natural Science Foundation under Grant 4164099.

References

- [1] A. Subramanian, L. X. Dong, and B. J. Nelson, "Stability and analysis of configuration-tunable bi-directional MWNT bearings," *Nanotechnology*, vol. 20, no. 49, Article ID 495704, 2009.
- [2] Y. Song, X. Cheng, H. Chen et al., "Highly compression-tolerant folded carbon nanotube/paper as solid-state supercapacitor electrode," *Micro & Nano Letters*, vol. 11, no. 10, pp. 586–590, 2016.
- [3] B. Q. Wei, R. Vajtai, and P. M. Ajayan, "Reliability and current carrying capacity of carbon nanotubes," *Applied Physics Letters*, vol. 79, no. 8, pp. 1172–1174, 2001.
- [4] M. F. L. De Volder, S. H. Tawfik, R. H. Baughman, and A. J. Hart, "Carbon nanotubes: present and future commercial applications," *Science*, vol. 339, no. 6119, pp. 535–539, 2013.
- [5] M. A. Kuroda, A. Cangelaris, and J.-P. Leburton, "Nonlinear transport and heat dissipation in metallic carbon nanotubes," *Physical Review Letters*, vol. 95, no. 26, Article ID 266803, 2005.
- [6] S. Xie, N. Jiao, S. Tung, and L. Liu, "Fabrication of SWCNT-graphene field-effect transistors," *Micromachines*, vol. 6, no. 9, pp. 1317–1330, 2015.
- [7] S. J. Wind, J. Appenzeller, R. Martel, V. Derycke, and P. Avouris, "Vertical scaling of carbon nanotube field-effect transistors using top gate electrodes," *Applied Physics Letters*, vol. 80, no. 20, pp. 3817–3819, 2002.

- [8] A. D. Franklin, S. O. Koswatta, D. Farmer et al., "Scalable and fully self-aligned n-type carbon nanotube transistors with gate-all-around," in *Proceedings of the IEEE International Electron Devices Meeting (IEDM '12)*, San Francisco, Calif, USA, December 2012.
- [9] P. Wilhite, A. A. Vyas, J. Tan et al., "Metal-nanocarbon contacts," *Semiconductor Science and Technology*, vol. 29, no. 5, Article ID 054006, 2014.
- [10] D. Xu, A. Subramanian, L. Dong, and B. J. Nelson, "Shaping nanoelectrodes for high-precision dielectrophoretic assembly of carbon nanotubes," *IEEE Transactions on Nanotechnology*, vol. 8, no. 4, pp. 449–456, 2009.
- [11] M. Dimaki and P. Bøggild, "Dielectrophoresis of carbon nanotubes using microelectrodes: A Numerical Study," *Nanotechnology*, vol. 15, no. 8, pp. 1095–1102, 2004.
- [12] C. S. Han, H. W. Seo, H. W. Lee, S. H. Kim, and Y. K. Kwak, "Electrokinetic deposition of individual carbon nanotube onto an electrode gap," *International Journal of Precision Engineering and Manufacturing*, vol. 7, no. 1, pp. 42–46, 2006.
- [13] Q. Xu, "Design, Fabrication, and testing of an MEMS micro-gripper with dual-axis force sensor," *IEEE Sensors Journal*, vol. 15, no. 10, pp. 6017–6026, 2015.
- [14] H. Xie and S. Régnier, "High-efficiency automated nanomanipulation with parallel imaging/manipulation force microscopy," *IEEE Transactions on Nanotechnology*, vol. 11, no. 1, pp. 21–33, 2012.
- [15] P. Liu, L. Dong, F. Arai, and T. Fukuda, "Nanotube multi-functional nanoposition sensors," *Journal of Nanoengineering and Nanosystems*, vol. 219, no. 1, pp. 23–27, 2005.
- [16] M.-S. Wang, D. Golberg, and Y. Bando, "Superstrong low-resistant carbon nanotube-carbide-metal nanocontacts," *Advanced Materials*, vol. 22, no. 47, pp. 5350–5355, 2010.
- [17] J.-O. Lee, C. Park, J.-J. Kim, J. Kim, J. W. Park, and K.-H. Yoo, "Formation of low-resistance ohmic contacts between carbon nanotube and metal electrodes by a rapid thermal annealing method," *Journal of Physics D: Applied Physics*, vol. 33, no. 16, pp. 1953–1956, 2000.
- [18] I. Utke, P. Hoffmann, and J. Melngailis, "Gas-assisted focused electron beam and ion beam processing and fabrication," *Journal of Vacuum Science and Technology B: Microelectronics and Nanometer Structures*, vol. 26, no. 4, pp. 1197–1276, 2008.
- [19] R. Vajtai, B. Q. Wei, Z. J. Zhang, Y. Jung, G. Ramanath, and P. M. Ajayan, "Building carbon nanotubes and their smart architectures," *Smart Materials and Structures*, vol. 11, no. 5, pp. 691–698, 2002.
- [20] T. Saito, T. Yamada, D. Fabris et al., "Improved contact for thermal and electrical transport in carbon nanofiber interconnects," *Applied Physics Letters*, vol. 93, no. 10, 2008.
- [21] L. An and C. R. Friedrich, "Measurement of contact resistance of multiwall carbon nanotubes by electrical contact using a focused ion beam," *Nuclear Instruments and Methods in Physics Research B*, vol. 272, pp. 169–172, 2012.
- [22] S. Kim, D. D. Kulkarni, K. Rykaczewski, M. Henry, V. V. Tsukruk, and A. G. Fedorov, "Fabrication of an ultralow-resistance ohmic contact to MWCNT-metal interconnect using graphitic carbon by electron beam-induced deposition (EBID)," *IEEE Transactions on Nanotechnology*, vol. 11, no. 6, pp. 1223–1230, 2012.
- [23] T. Brintlinger, M. S. Fuhrer, J. Melngailis et al., "Electrodes for carbon nanotube devices by focused electron beam induced deposition of gold," *Journal of Vacuum Science and Technology B*, vol. 23, no. 6, pp. 3174–3177, 2005.
- [24] S. C. Lim, J. H. Jang, D. J. Bae et al., "Contact resistance between metal and carbon nanotube interconnects: effect of work function and wettability," *Applied Physics Letters*, vol. 95, no. 26, Article ID 264103, 2009.
- [25] C. Lan, P. Srisungsitthisunti, P. B. Amama, T. S. Fisher, X. Xu, and R. G. Reifenberger, "Measurement of metal/carbon nanotube contact resistance by adjusting contact length using laser ablation," *Nanotechnology*, vol. 19, no. 12, 2008.
- [26] K. Li, R. Wu, P. Wilhite et al., "Extraction of contact resistance in carbon nanofiber via interconnects with varying lengths," *Applied Physics Letters*, vol. 97, no. 25, Article ID 253109, 2010.
- [27] J. A. Greenwood and J. B. Williamson, "Contact of nominally flat surfaces," *Proceedings of the Royal Society A*, vol. 295, no. 1442, pp. 300–319, 1966.
- [28] T. Fukuda, F. Arai, and L. Dong, "Fabrication and property analysis of MWNT junctions through nanorobotic manipulations," *International Journal of Nonlinear Sciences and Numerical Simulation*, vol. 3, no. 3-4, pp. 753–758, 2002.
- [29] L. Dong, F. Arai, and T. Fukuda, "Nanoassembly of carbon nanotubes through mechanochemical nanorobotic manipulations," *Japanese Journal of Applied Physics, Part 1: Regular Papers and Short Notes and Review Papers*, vol. 42, no. 1, pp. 295–298, 2003.
- [30] P. Liu, M. Nakajima, Z. Yang, T. Fukuda, and F. Arai, "Evaluation of van der Waals forces between the carbon nanotube tip and gold surface under an electron microscope," *Proceedings of the Institution of Mechanical Engineers, Part N: Journal of Nanoengineering and Nanosystems*, vol. 222, no. 2, pp. 33–38, 2008.
- [31] T. Kanbara, T. Takenobu, T. Takahashi et al., "Contact resistance modulation in carbon nanotube devices investigated by four-probe experiments," *Applied Physics Letters*, vol. 88, no. 5, Article ID 053118, pp. 1–3, 2006.
- [32] Q. Shi, N. Yu, Q. Huang, T. Fukuda, M. Nakajima, and Z. Yang, "Contact characterization between multi-walled carbon nanotubes and metal electrodes," in *Proceedings of the 15th IEEE International Conference on Nanotechnology (IEEE-NANO '15)*, pp. 1386–1389, Rome, Italy, July 2015.
- [33] K. Rykaczewski, M. R. Henry, S.-K. Kim et al., "The effect of the geometry and material properties of a carbon joint produced by electron beam induced deposition on the electrical resistance of a multiwalled carbon nanotube-to-metal contact interface," *Nanotechnology*, vol. 21, no. 3, Article ID 035202, 2010.
- [34] J. Visser, "Van der Waals and other cohesive forces affecting powder fluidization," *Powder Technology*, vol. 58, no. 1, pp. 1–10, 1989.
- [35] R. A. Onions and J. F. Archard, "The contact of surfaces having a random structure," *Journal of Physics D: Applied Physics*, vol. 6, no. 3, pp. 289–304, 1973.